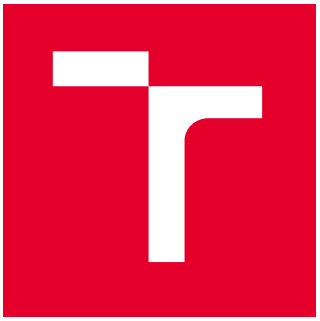

BRNO UNIVERSITY OF TECHNOLOGY

VYSOKÉ UČENÍ TECHNICKÉ V BRNĚ

FACULTY OF MECHANICAL ENGINEERING

FAKULTA STROJNÍHO INŽENÝRSTVÍ

INSTITUTE OF SOLID MECHANICS, MECHATRONICS AND BIOMECHANICS

ÚSTAV MECHANIKY TĚLES, MECHATRONIKY A BIOMECHANIKY

ANALYSIS OF THE EFFECT OF SIZE, TEMPERATURE AND STRAIN RATE ON THE HARDENING OF METALLIC MATERIALS

ANALÝZA VLIVU VELIKOSTI, TEPLOTY A RYCHLOSTI DEFORMACE NA ZPEVNĚNÍ KOVOVÝCH MATERIÁLŮ

MASTER'S THESIS

DIPLOMOVÁ PRÁCE

AUTHOR — Bc. Radek Novotný

AUTOR PRÁCE

SUPERVISOR — doc. Ing. František Šebek, Ph.D.

VEDOUCÍ PRÁCE

BRNO 2025

BRNO UNIVERSITY OF TECHNOLOGY
FACULTY OF MECHANICAL ENGINEERING

Assignment Master's Thesis

Institut:	Institute of Solid Mechanics, Mechatronics and Biomechanics
Student:	**Bc. Radek Novotný**
Degree programm:	Engineering Mechanics and Biomechanics
Branch:	Engineering Mechanics
Supervisor:	**doc. Ing. František Šebek, Ph.D.**
Academic year:	2024/25

As provided for by the Act No. 111/98 Coll. on higher education institutions and the BUT Study and Examination Regulations, the director of the Institute hereby assigns the following topic of Master's Thesis:

Analysis of the effect of size, temperature and strain rate on the hardening of metallic materials

Brief Description:

Knowledge of behaviour of metallic materials beyond the yield point is important for numerical simulations of various operating conditions as well as manufacturing processes. The application of the finite element method in the design process can be successful only in the case of good knowledge of the material behaviour under the given circumstances, which may be influenced by various factors, such as the size, elevated temperature or high strain rate. However, these must be studied experimentally.

Master's Thesis goals:

1. Design of the experimental program for the investigation of the effect of size, temperature and strain rate.
2. Development of a miniature testing device for the investigation of the size effect with respect to the camera positioning and specimen gripping.
3. Processing and assessment of measured data on standard and miniaturized specimens.
4. Calibration of the material model taking into account various effects on hardening.

Recommended bibliography:

ASTM INTERNATIONAL. Standard Test Method for Tension Testing of Metallic Materials. 24. West Conshohocken, 2024.

BEERLI, T.; ROTH, Ch. C. and MOHR, D. Semi-automatic miniature specimen testing method to characterize the plasticity and fracture properties of metals. Acta Materialia. 2024, Vol. 263, pp. 119539.

JENÍK, I.; KUBÍK, P.; ŠEBEK, F.; HŮLKA, J. and PETRUŠKA, J. Sequential simulation and neural network in the stress-strain curve identification over the large strains using tensile test. Archive of Applied Mechanics. 2017, Vol. 87, pp. 1077-1093.

KAMAYA, M. and KAWAKUBO. A procedure for determining the true stress-strain curve over a large range of strains using digital image correlation and finite element analysis. Mechanics of Materials. 2011, Vol. 43, Issue 5, pp. 243-253.

MIRONE, G. A new model for the elastoplastic characterization and the stress-strain determination on the necking section of a tensile specimen. International Journal of Solids and Structures. 2004, Vol. 41, Issue 13, pp. 3545-3564.

PEIRS, J.; VERLEYSEN, P.; VAN PAEPEGEM, W. and DEGRIECK, J. Determining the stress-strain behaviour at large strains from high strain rate tensile and shear experiments. International Journal of Impact Engineering. 2011, Vol. 38, Issue 5, pp. 406-415.

SAKARIDIS, E.; MEYER, P. P.; ROTH, Ch. C. and MOHR, D. Whip-Bezier: A C1-continuous hardening law for efficient direct and inverse identification. International Journal of Solids and Structures. 2024, Vol. 288, pp. 112616.

Deadline for submission Master's Thesis is given by the Schedule of the Academic year 2024/25

In Brno,

L. S.

prof. Ing. Jindřich Petruška, CSc. Director of the Institute	doc. Ing. Jiří Hlinka, Ph.D. FME dean

Abstrakt

Diplomová práce se zabývá analýzou vlivu velikosti vzorku, teploty a rychlosti deformace na deformační zpevnění vybraných kovových materiálů – hliníkové slitiny AW 2024–T351, niklové slitiny Inconel 718 a nerezové oceli 316L. Pro experimentální ověření byly navrženy a realizovány tahové zkoušky včetně miniaturizovaných variant, jejichž cílem bylo postihnout komplexní materiálové chování v různých podmínkách zatěžování. Naměřená data byla využita ke kalibraci Johnson–Cookova konstitutivního modelu, přičemž optimalizace parametrů byla provedena pomocí optimalizace hejnem částic. Správnost kalibrace byla ověřena pomocí numerických simulací v prostředí metody konečných prvků. Výsledky ukazují význam vlivu velikosti, rychlosti deformace a teploty na zpevnění a potvrzují vhodnost použití kalibrovaného modelu pro popis materiálového chování ve výpočetních simulacích.

Klíčová slova

materiálové modely, Johnson–Cook, miniaturní zkoušky, jednoosá zkouška tahem, aproximace křivky, optimalizace hejnem částic

Abstract

This thesis focuses on the analysis of the influence of specimen size, temperature, and strain rate on the strain hardening of selected metallic materials – aluminium alloy AW 2024–T351, nickel alloy Inconel 718, and stainless steel 316L. A comprehensive experimental program was designed, including miniature tensile testing, to investigate the complex behavior of materials under varying loading conditions. The acquired data were used for the calibration of the Johnson–Cook constitutive model, with parameter optimization performed using the Particle swarm optimization. The accuracy of the calibrated model was validated by finite element method. The results demonstrate the significant effects of strain rate, temperature, and specimen size on material hardening and confirm the applicability of the calibrated model in computational simulations of structural components.

Keywords

material models, Johnson–Cook, miniature testing, uniaxial tensile test, curve fitting, particke swarm optimization

Rozšířený abstrakt

Úspora materiálu, efektivita, nízké výrobní náklady, snížení množství odpadu, energetická náročnost výroby, náklady na dopravu. Tyto všechny faktory a mnohé další mají u nových konstrukcí, strojů a systémů v dnešní době velký význam. Řadu z nich je možné ovlivnit díky správnému návrhu konstrukce, efektivnímu využití materiálu vzhledem k zatížení součástí nebo například snížením vlivů okolního prostředí. Hlavně v odvětvích, jako je kosmický průmysl, letectví, ale také v automobilním a dopravním inženýrství se rapidním způsobem rozšiřují aditivně vyráběné materiály, superslitiny nebo vysoce pevné a lehké hliníkové slitiny. V rámci vývoje je výroba prototypů a jejich testování, které je jak časově, tak finančně náročné, nahrazována v co největší míře tvorbou virtuálních modelů a numerických simulací, které umožňují velkou variabilitu, časovou i finanční úsporu, ale hlavně nižší riziko selhání a možnost větší optimalizace a široké škály testů. Díky tomu dochází k výraznému snižování hmotnosti konstrukcí při zachování jejich pevnosti, nebo výraznému zlepšení například aerodynamických vlastností nebo vyšší účinnosti. Tyto simulace se však neobejdou bez možnosti správného simulování materiálových vlastností.

Vysoké rychlosti zatěžování dynamických systémů, pohonných jednotek, proudových motorů nebo výztuží křídel či podvozků letadel a automobilů mohou výrazným způsobem ovlivnit jejich chování a tím i životnost a hlavně bezpečnost celé konstrukce. Stejně tak mohou být materiály náchylné na změny teploty. Komponenty, které tak pracují za zvýšené teploty, musí být vyrobeny z materiálů, které zachovávají své vlastnosti i při vyšších teplotách a s jejich možnou změnou vlastností se musí počítat při návrhu. Hlavně při výrobě tenkých a velmi malých struktur, které mohou být díky novým materiálům a superslitinám vysoce pevné a zároveň lehké, je jednou z nejméně prozkoumaných vlastností právě vliv velikosti. Ukazuje se, že přílišné zmenšení základních rozměrů součástek může vést ke změně materiálového chování. Při vývoji nových materiálů a určení jejich možného využití je tak nutné tyto materiály důkladně testovat s přihlédnutím na celou škálu možných vlivů a na základě výsledků přenést tyto poznatky do virtuálního prostředí v podobě materiálových modelů, které co nejpřesněji reprezentují jejich chování.

Protože jsou možnosti výzkumu vlivu velikosti dnes bohužel značně omezené a miniaturní testování ještě není zcela rozšířenou metodou, jsou výzkumná pracoviště odkázaná na vývoj vlastních zkušebních zařízení. V rámci této práce proběhl vývoj testovací aparatury pro miniaturní tahové zkoušky, včetně držáku kamery pro metodu digitální korelace obrazu a přesného systému upínání vzorků. Při vývoji musela být dodržena základní pravidla testování materiálů, stejně jako možnost porovnání výsledků mezi jednotlivými pracovišti a současně s běžným typem testů. Miniaturní testování zároveň přináší mnohé výzvy, jako je správné určení deformace vzorku optickými metodami, nebo vhodný tvar vzorků k určení všech důležitých vlastností materiálu.

Materiálové modely musí být kalibrovány s ohledem právě na variabilitu okolních vlivů a změny vlastností materiálu napříč různými okrajovými podmínkami. Pro jejich kalibraci a určení materiálových parametrů je možné využít celou řadu možných přístupů. V této práci byl zvolen široce používaný Johnson–Cookův model, jehož parametry byly určeny na základě dat z tahových zkoušek provedených při různých rychlostech deformace a teplotách, a to pro tři typy materiálů – hliníkovou slitinu AW 2024–T351, nerezovou ocel 316L a superslitinu Inconel 718. Jako nejefektivnější a nejpřesnější se ukazují dnes již velmi pokročilé metody umělé inteligence. Optimalizace hejnem částic, která se zakládá na popisu chování hejna ryb nebo ptáků, byla v této práci implementována v prostředí

MATLAB a úspěšně využita pro automatizovanou identifikaci parametrů materiálového modelu.

Pouze určení parametrů materiálového modelu není dostačující. Materiálové modely je nutné před jejich využitím validovat ve výpočetním prostředí, ve kterém budou využívány. Z toho důvodu je nedílnou součástí kalibrace materiálových modelů i numerická simulace experimentů, na jejichž datech byl materiálový model určen. V této práci byla validace provedena pomocí numerických simulací v prostředí LS-DYNA, kde byly výsledky simulací porovnány s experimentálními tahovými křivkami. To se zpravidla děje v numerických simulacích pomocí metody konečných prvků v softwarech jako je Ansys, ABAQUS nebo LS-DYNA.

Na základě správně nastaveného materiálového modelu v metodě konečných prvků je následně možné provádět numerické simulace součástí nebo celých strojů, k určení hodnot napětí, deformace, jejich životnosti a bezpečnosti. Kalibrace materiálových modelů je tak velmi důležitou a nedílnou součástí výroby všech strojů a zařízení, při jejichž vývoji jsou využívány numerické simulace a pevnostní výpočty.

Bibliographic citation

NOVOTNÝ, Radek. Analysis of the effect of size, temperature and strain rate on the hardening of metallic materials. Online, Master's Thesis. František ŠEBEK (supervisor). Brno: Brno University of Technology, Faculty of Mechanical Engineering, 2025. Available at: https://www.vut.cz/en/students/final-thesis/detail/165101.

Declaration

I hereby declare that I have written this master's thesis on my own, under the supervision of doc. Ing. František Šebek, Ph.D., using the literature included in the list of references. During the writing process, I also used artificial intelligence tools (e.g. language models or translators) to improve the linguistic and stylistic quality of the text, while ensuring that the content and interpretation of the work remained my own.

Acknowledgement

I would like to thank my thesis supervisor doc. Ing. František Šebek, Ph.D., for his professional guidance, valuable advice, helpful approach and patience, which he gave me during the whole time of solving this thesis. His experience and willingness to consult complex problems contributed significantly to the realization of this thesis.

Poděkování

Z celého srdce děkuji své rodině za nekonečnou podporu, trpělivost, pochopení a lásku během celé mé studijní cesty. Děkuji, že jste stáli při mně i ve chvílích, kdy jsem o sobě pochyboval, a že jste mi vždy věřili, i když jsem si sám nevěřil. Vaše tiché oběti, povzbudivá slova a klidná přítomnost mi dávaly sílu pokračovat dál.

Contents

1 Introduction **12**
1.1 Motivation . . . 12
1.2 Formulating of the problem situation . . . 13
1.3 Problem formulation and solution . . . 14

2 State of the art **16**
2.1 Strain rate and effect of temperature . . . 16
2.1.1 Stainless steel 316L . . . 16
2.1.2 Inconel 718 . . . 17
2.2 Overview of miniature testing . . . 19
2.2.1 Size effect on ductile fracture . . . 20
2.2.2 Miniature testing for prediction of properties of a common size specimen . . . 21
2.2.3 Semi-automatic testing of miniature specimen . . . 22

3 Hardening of the metals **24**
3.1 Description of hardening . . . 24
3.1.1 Metallic Materials Hardening Mechanisms . . . 24
3.2 Influence of external parameters and its material models . . . 26
3.2.1 Strain rate . . . 26
3.2.2 Temperature . . . 26
3.2.3 Size . . . 27
3.3 Common experimental procedures . . . 29
3.4 Digital image correlation . . . 29
3.5 Particle swarm optimization . . . 30
3.5.1 The principle of the algorithm . . . 31
3.5.2 PSO in MATLAB . . . 32

4 Modifications of a testing device **34**
4.1 DIC camera holder . . . 34
4.1.1 DIC camera lens attachment . . . 35
4.1.2 Movement in the x and y axes . . . 36
4.1.3 Movement in z axis . . . 36
4.1.4 Production and comparison . . . 38
4.2 Clamping of the specimen . . . 39
4.3 Joint and centering fixture . . . 41
4.3.1 Normalized and designed parts of joint . . . 41

4.3.2 Assembly of the joint and its function . . . 44
4.4 Fixtures for clamping and other parts . . . 45
4.4.1 3D printed fixtures . . . 45
4.4.2 Clamps housing . . . 46
4.4.3 Motor movement screw head . . . 47
4.5 Final assembly . . . 48

5 Plan of experiments 50
5.1 Tensile test . . . 50
5.2 Static testing . . . 52
5.3 Miniature testing . . . 55

6 Experimental procedures 57
6.1 Miniature testing procedure . . . 57
6.1.1 Preparation of mini specimens . . . 57
6.1.2 Experiment preparation and specimen clamping . . . 58
6.1.3 The progress of the experiment . . . 60
6.2 Mini testing in COMTES FHT . . . 60
6.3 Summary of measurements made . . . 61

7 Data processing 62
7.1 Computational relations . . . 62
7.2 Material model . . . 64
7.2.1 Model of elasticity . . . 64
7.2.2 Model of plasticity . . . 64
7.3 Preparation of experimental data for curve fitting . . . 65
7.3.1 Engineering stress–strain diagram . . . 65
7.3.2 True stress–strain diagram . . . 67
7.3.3 Evaluation of static curve . . . 67
7.4 Curve fitting in MATLAB . . . 68

8 Material model calibration 71
8.1 Analysis settings . . . 71
8.1.1 Geometry and boundary conditions . . . 71
8.1.2 Finite element mesh . . . 73
8.1.3 Material model . . . 73
8.1.4 Modifying settings . . . 74
8.2 Processing of results and comparison of simulation and experiment . . . 75

9 Results and discussion 77
9.1 Results for stainless steel 316L . . . 77
9.2 Results for Inconel 718 . . . 78
9.3 Results for AW 2024–T351 . . . 80
9.3.1 Size effect for AW 2024–T351 . . . 81

10 Conclusion 84

List of References **86**

List of Figures **94**

List of Tables **96**

Appendices **96**

A Tensile diagrams **97**

B *.k files **102**

1 Introduction

1.1 Motivation

Knowledge of the behaviour of structural materials allows engineers and scientists to predict how materials and components made from them will behave under different types of loading, in different environments, and at different temperatures. The behavior of materials is influenced by a number of factors that have a major impact on mechanical properties such as strength, hardness, toughness, or fatigue. An important parameter for describing a material and its behavior is the hardening caused by the external load or the deformation that the external load induces. A very simple and most common type of loading for testing purposes is uniaxial tension – such type of loading is used in uniaxial tensile testing, which can take many forms and provides a large amount of information about the behavior of the material, including the effect of strain rate, temperature and size of the test specimen [1].

The loading of the specimen during tensile testing induces deformation in the material or specimen, which may be elastic, plastic, or, in some cases, rheological. Plastic deformation has a significant effect on the behavior of the material, and therefore, it is important to continue research and increase knowledge of the properties of new alloys or materials with different manufacturing methods. Currently, the production of alloys from metallic materials using additive manufacturing is becoming more and more widespread, which requires a detailed determination of the properties of these materials for further use.

Material hardening is the process by which a material gains increased strength, hardness, and resistance to deformation. This phenomenon is most commonly associated with metallic materials and arises as a result of changes at the microscopic level during mechanical loading or technological processing. There are several hardening mechanisms that differ in the way of achieving increase in strength, with strain hardening being the most important mechanism in engineering practice [2].

Deformation hardening is a process by which the strength and hardness of a material increase as a result of plastic deformation, a phenomenon that is particularly typical of metals and their alloys. This process is caused by changes in the crystal structure of the material at the microscopic level. When a material is loaded beyond its elastic limit, inelastic deformation occurs, in which the atoms in the crystal lattice are irreversibly displaced. This movement is accompanied by the formation and movement of dislocations, which are disturbances in the crystal lattice. Plastic deformation significantly increases the density of these dislocations, which interact and block each other, preventing their further movement. This phenomenon requires increasingly greater force to continue deformation, increasing the strength and hardness of the material. However, at the same time, the ductility is reduced, making the material less capable of further deformation. The mechanism of strain hardening is based on the formation of a dense network of dislocations and an increase in internal stress in the material. The interactions of the dislocations create local stresses that further increase the resistance to movement of the

dislocations [1, 2]. This process is crucial for many industrial applications where it is necessary to increase the strength of materials, but it can also lead to loss of ductility, which is sometimes undesirable.

Tensile test responses, which contain the response of the material to external loads and show the hardening process of the specimen under test as strain increases until failure, need to be implemented in computational software using material models for structural design purposes. These models allow simulation of the actual behavior of materials under different types of loading and include everything from linear elastic behavior, which describes the relationship between stress and strain in the elastic regime, to advanced elastoplastic models capturing the transition to the plastic region and subsequent hardening isotropic and kinematic hardening, for instance, describe different mechanisms of hardening increase during plastic deformation. For soft materials, such as rubbers or biological tissues, hyper-elastic models are used to describe their non-linear elastic behavior during large deformations. Viscoplastic models reflect the dependence of plastic deformation on time and loading rate, which is crucial when modelling dynamic, creep, or long-term loading. Brittle and damage models allow the simulation of crack initiation and propagation in materials such as concrete, ceramics, or composites. These models, together with the corresponding material parameters, transfer the physical and mechanical properties of real materials into the environment of the Finite Element Method (FEM), where they serve as a basis for accurate analysis and optimization of structures [2].

1.2 Formulating of the problem situation

Calibration of material parameters for advanced material models such as the Johnson–Cook model, Cowper–Symonds model, Gurson–Tvergaard–Needleman (GTN) model, viscoplastic models or hyperelastic models are essential for accurate simulation of material behavior in engineering applications. These models allow the simulation of a wide range of mechanical properties, from elastic and plastic behavior to viscoplastic, creep and damage phenomena. However, calibrating material parameters for advanced material models is a challenging process that requires experimental data reflecting the influence of various factors such as:

- **Size** – It has significant influence on mechanical properties such as strength and plasticity. Small specimens reveal microstructural effects, but are affected by size effects which can distort the results.
- **Rate of deformation** – High rates of deformation usually cause an increase in strength and a decrease in ductility. It is necessary to include rate dependencies in material models, for example, in viscoplastic or creep models.
- **Temperature** – It affects strength, plasticity, and other properties of the material; higher temperatures lead to lower yield strength and greater susceptibility to creep behavior.

The calibration of the material model is complicated by various problems resulting from several factors:

- **Multiple factor consideration** – The combination of size effects, strain rate, and temperature requires a complex approach as these factors often interact.

- **Complexity of models** – The Johnson–Cook model, viscoplastic models, or hyperelastic models have specific data requirements and need to capture different aspects of material behavior.
- **Numerical prediction** – Incorrectly calibrated material parameters can lead to erroneous simulations and unexpected structural failures.

The importance of experimental data for accurate calibration of material models. It is essential to:

- **Analyse the effect of size** on the experimental data and correct the results.
- **Conduct experiments at different velocities and temperatures** to obtain reliable model parameters.
- **Integrate data from different types of measurements** into one consistent material model.

1.3 Problem formulation and solution

The determination of the Johnson–Cook material model parameters is based on measured experimental data for AW 2024–T351, Inconel 718 and 316L stainless steel, taking into account the strain rate and temperature and showing the effect of the specimen size for these materials.

The solution will be the realisation of the proposed experiments focused on the calibration of material parameters. The experiments will be designed to capture all of the aforementioned effects on the hardening of metallic materials while respecting the technical capabilities of the available equipment, as well as time and financial constraints. The data obtained from the experiments will be processed using MATLAB, which allows analyses, curve fitting, and determination of material parameters using optimisation methods. Other software can also be used for data processing, for example Python. Numerical simulations in FEM software such as Ansys, Abaqus or LS-DYNA will be used to verify the accuracy of these models, where the simulation results will be compared with the experimental data. In this way, a calibrated material model that describes the behaviour of the material well and is suitable for use in engineering practice will be developed.

Goals of the thesis

1. **Design of the experimental program for the investigation of the effect of size, temperature, and strain rate**

   Development of an experimental plan that includes different types of tests to investigate in detail the influence of these factors on the hardening of metallic materials.

2. **Development of a miniature testing device to investigate the effect of size with respect to the camera positioning and specimen gripping**

   A very important step to be able to measure the experimental data for miniature specimens. In this step, the design and subsequent implementation of a camera mount for Digital Image Correlation (DIC) is required. Development of new clamping for mounting miniature specimens and further design modifications to test equipment.

3. **Processing and assessment of measured data on standard and miniaturized specimens**

   Analysis and interpretation of data obtained from experiments with different types of specimens. This includes processing data sets, applying appropriate statistical methods to reduce outliers, and using software such as MATLAB or Python to display and model the results.

4. **Calibration of the material model taking into account various effects on hardening**

   Determination of material parameters for models such as Johnson–Cook or other suitable models based on experimental data. The calibrated models will be validated by comparison with experimental results to describe the material behavior under different conditions such as temperature, strain rate, and the effect of specimen size.

2 State of the art

In order to gain a deeper understanding of the mechanical behaviour of metallic materials under various loading conditions, it is essential to first review the current state of knowledge in the field. This chapter aims to identify and summarise key scientific studies focused on the effects of strain rate, temperature, and specimen size on material response. This overview not only highlights what research has already been conducted, but also helps to uncover existing knowledge gaps that the present thesis seeks to address.

2.1 Strain rate and effect of temperature

Understanding how materials respond to different strain rates and temperatures is crucial to predicting their behaviour under various dynamic, impact loading conditions, or high temperature conditions. The effect of additive manufacturing on the mechanical properties of materials has recently been the subject of extensive investigation. Then these are typically compared to conventional manufactured materials.

2.1.1 Stainless steel 316L

Güden M. et al. [3] focused on comparing the mechanical behaviour of two variants of 316L stainless steel – one produced by selective laser melting SLM–316L and the other a conventionally processed annealed and rolled alloy C–316L. The work investigates the effect of the strain rate in a wide range from 10^{-4} to approximately $2800\,\mathrm{s}^{-1}$, utilising both quasi-static compression tests and dynamic tests using a split Hopkinson pressure bar [3].

The authors find that SLM–316L exhibits a higher yield strength (R_e = 510 MPa) compared to C–316L (R_e = 360 MPa), attributed to the higher dislocation density in the additively manufactured material. Both alloys demonstrate strain rate sensitivity, with SLM–316L showing a higher sensitivity in the quasi-static regime. At higher strain rates, the sensitivities of both materials become comparable. However, C–316L shows a more rapid decline in sensitivity with increasing strain [3].

The study also determines the Johnson–Cook material model parameters (this model is explained in 7.2.2). The strain rate sensitivity parameter C in the Johnson–Cook model was determined for both alloys. For SLM–316L, C decreases from 0.18 at a true strain of 0.11 to 0.011 at 0.56. For C–316L, C values range from 0.0185 to 0.009 over the same strain interval. Additionally, when fitted within the lower strain rate range (10^{-4} to $10^{-2}\,\mathrm{s}^{-1}$), C decreases from 0.0185 to 0.0155 at strains of 0.11 and 0.22, and further to 0.013 at higher strains [3].

Li et al. [4] investigated the mechanical behaviour of 316L stainless steel produced by laser powder bed fusion, with a particular focus on the influence of specimen type and microstructural features on tensile performance, strain rate sensitivity, and activation volume. Two types of specimens were tested: directly-printed tensile specimens built with support structures, and flat tensile specimens extracted from printed plates. All specimens had a relative density of at least 98.8 % [4].

The study revealed a clear difference in mechanical properties between the two types of specimens. The plate-extracted samples exhibited both higher strength and greater percent elongation compared to the directly-printed ones. Additionally, the measured strain rate sensitivity for both specimen types was approximately 0.02–0.03, which is notably higher than for conventionally processed 316L stainless steel. The calculated activation volume was very low ($\sim$ 20–30 b^3, where b is the Burgers vector of 316L), implying that the dominant mechanisms of plasticity operate at a microstructural scale much finer than the measured grain structure. In general, the study highlights that the geometry of the specimen and the structure of the internal defects can strongly influence the tensile response of additively manufactured materials, even when their bulk density is high [4].

2.1.2 Inconel 718

Additively manufactured Inconel 718 appears to be one of the highly researched materials of late. The mechanical response of Inconel 718 shows the influence of the strain rate on its material properties. At low to moderate strain rates, Inconel 718 exhibits strain rate sensitivity typically associated with strain rate hardening, resulting in increased yield strength and flow stress. This effect becomes more pronounced in additively manufactured materials with low porosity, where ductility can even increase due to a more effective distribution of plastic deformation [5, 6, 7, 8].

The effect of strain rate on additively manufactured Inconel 718 is influenced by the microstructural anisotropy resulting from the layer-by-layer build process. In the as-built condition, the mechanical response can be relatively homogeneous across directions, but post-processing (e.g., aging heat treatments) often enhances directional differences, with the build direction typically showing reduced ductility but increasing strength mainly in pressure [5, 8, 6, 7].

When strain rate effects are combined with elevated temperatures, the material generally exhibits a decrease in strength but a concurrent increase in ductility. Constitutive models such as the Johnson–Cook model require careful calibration to account for these coupled effects, particularly the thermal softening terms that vary with strain rate and temperature [8, 7].

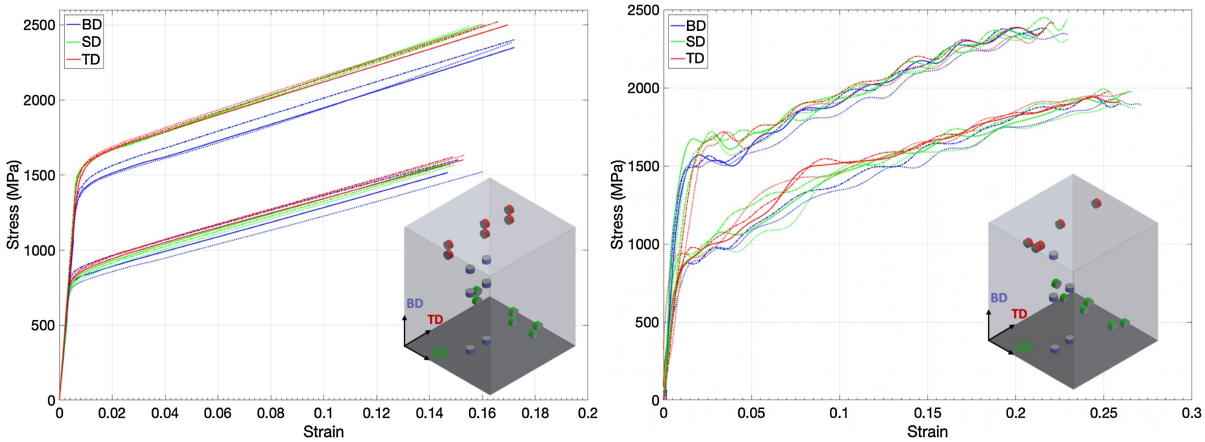

Figure 2.1: Comparison of quasi-static and dynamic stress–strain responses of Inconel 718 [7]

Kouraytem et al. [7] focused their study on investigating the mechanical response of

additively manufactured Inconel 718 produced via Laser powder bed fusion under different strain rates. Specimens were tested in two conditions, as-built and direct-age hardened. The experiments included both quasi-static and dynamic compression tests, with samples extracted in three principal directions corresponding to the build orientation. The results can be seen in Fig. 2.1, with the quasi-static test results shown on the left and the dynamic compression test results on the right. The lower set corresponds to the as-built condition, and the upper set to the heat-treated condition. It is clearly visible that heat treatment significantly increases the yield strength and overall strength, with stress values in the heat-treated specimens reaching nearly twice those of the as-built ones [7].

When comparing quasi-static and dynamic responses, it was observed that dynamic loading results in higher stress levels in both the elastic and plastic regions, as well as a steeper curve progression. This reflects a positive strain rate sensitivity, indicating improved resistance of the material under impact or high-rate loading. The results confirm that additively manufactured Inconel 718, when properly heat-treated, can achieve excellent mechanical properties even under high strain rates, making it a promising material for applications in aerospace, automotive, and defense industries where dynamic loading is critical [7].

Forni et al. [8] also investigated the mechanical behaviour of Inconel 718 under high strain rates. For the experimental measurements, they employed a high strain rate tensile testing setup using a split Hopkinson tensile bar to simulate extreme service conditions. Based on the collected data, they calibrated the material parameters of the Johnson–Cook constitutive model, with particular emphasis on capturing the influence of strain rate on the stress–strain response. At room temperature (20 °C), the strain rate sensitivity parameter C was determined to be 0.01535 for the as-cast material, 0.01218 for the as-built condition manufactured with 300 W laser power, and 0.02006 for the as-built condition at 400 W. These differences reflect the varying sensitivity to the strain rate depending on the manufacturing process and microstructural characteristics [8].

In addition, Forni et al.[8] also examined the effect of elevated temperatures on the tensile behaviour of Inconel 718. Tests were conducted at 20 °C, 350 °C, and 550 °C under both quasi-static and high strain rate loading. The results showed that increasing temperature led to a clear reduction in yield strength and ultimate tensile strength, while ductility tended to increase. This thermal softening effect was observed consistently across both as-cast and as-built material conditions. The authors also noted that the influence of the manufacturing process (cast agains additively manufactured) diminished at higher temperatures, with mechanical responses becoming more comparable. These observations were incorporated into the Johnson–Cook model through a calibrated thermal softening exponent, enabling more accurate simulation of Inconel 718 under combined thermal and dynamic loading conditions [8].

In some materials, the influence of strain rate and temperature on plastic deformation is too complex to be accurately captured by classical constitutive models. As a result, new models are developed or existing ones are modified to better reflect the coupled effects of these parameters on the material response.

Wang et al. [9] proposed a modified Johnson–Cook model to better describe the complex flow behaviour of the 2A12 aluminium alloy under coupled strain rate and temperature conditions. Their motivation stemmed from the observation that the classical Johnson–Cook model failed to accurately capture the material's non-monotonic strain rate sensitivity at elevated temperatures. In particular, they reported a so-called V-shaped

response, where flow stress initially decreases and then increases again with increasing strain rate, especially at temperatures between 350 K and 450 K. Such behaviour could not be adequately reproduced using the original model formulation [9].

To address these limitations, the authors introduced a strain-dependent nonlinear strain rate sensitivity term and a temperature-softening function that includes coupling with strain. The resulting model is formulated as follows [9]:

$$\sigma = \left(A + B\varepsilon_p + C\varepsilon_p^2 + \frac{D}{\varepsilon_p} \right) (1 + E \ln \dot{\varepsilon}^*) \, f(\varepsilon_p, T^*), \tag{2.1}$$

where ε_p is the plastic strain, $\dot{\varepsilon}^* = \dot{\varepsilon}/\dot{\varepsilon}_0$ is the normalized strain rate, and $f(\varepsilon_p, T^*)$ is a thermal softening function accounting for the interaction between strain and temperature. The term $\left(A + B\varepsilon_p + C\varepsilon_p^2 + \frac{D}{\varepsilon_p} \right)$ represents the strain hardening behaviour of the material [9].

The improved model was shown to provide significantly better agreement with experimental data across a range of strain rates and temperatures, and was successfully validated using FEM in Abaqus [9].

2.2 Overview of miniature testing

Miniature testing of metals is based on the need to obtain local plastic or fracture properties of materials in situations where it is not possible to produce standard test bodies with conventional dimensions of tens of millimeters, for example in thin material layers, electronic components or in areas with steep gradients in mechanical properties. Research dates back to the 1970s. In those days, the early so-called micro-dogbone contact specimens were investigated. However, it was not until systematic reviews from the early 2000s onward that optimal length/thickness ratios and minimum grain numbers for representative behaviours began to become definitively clear [10, 11].

Normally, the geometry of miniature specimens follows the shapes of conventional test bodies, and their width does not usually exceed 2 mm. Due to affine scaling, specimens can be sized with factors between $\lambda = 5$ and $\lambda = 20$ relative to full-size standards, where λ is the ratio between the original and mini size. Due to the similarity of the shapes, a direct comparison of the results and transfer of knowledge between large and miniature specimens is possible [1, 12].

Miniature specimens are most often produced by µ-milling or µ-wire-EDM (µ-WEDM) or other advanced machining methods such as laser cutting or electronic machining. Advantages of µ-WEDM include high precision of around ±0.2 µm and roughness below 0.1 µm. However, there is a so-called recast layer and a thermally influenced zone up to 4 µm thickness. For materials thinner than 0.15 mm, this layer thus represents a significant percentage of the cross section, which can misrepresent the resulting material characteristics [10, 13].

It is possible to come across some standardization and validation works nowadays that summarize recommendations for miniature tensile testing. Key criteria include a minimum width to thickness ratio of 5–10 and a minimum of 6–10 grains in thickness to maintain homogeneity. The DIC-based deformation measurement approach involves performing at least three repetitions in order to assess the statistical deviation of the obtained results.

All these requirements are summarized in detailed review and design guidelines [11].

With the advance of high throughput and automated systems, testing has reached the level of sophisticated frames with interchangeable specimen cartridges. Advanced workstations also use robotic manipulators with prepared approaches that use cassettes with tens of specimens that are sequentially clamped and tested in a single run. This makes these tests highly productive and eliminates operator error during specimen manipulation [14, 15].

In the future, further integration with advanced DIC of internal structures or the implementation of machine learning is expected for automated strain field analysis and failure prediction at the individual grain level. This paves the way for detailed mapping of material micromechanics and the design of new bio-inspired composites with a controlled hierarchy of structures [1].

2.2.1 Size effect on ductile fracture

The size effect is also seen in certain manufacturing methods that have been used for a long time for various engineering applications. One of them, for example, is micro-flanged upsetting. Micro-flanged upsetting is a special microforming technique in which a small cylindrical blank (billet) is inserted into an axisymmetric tool consisting of a hollow sleeve (die) and a piston (punch). The plunger gradually hits the top of the cylinder and pushes it down axially. However, due to the shape of the cavity in the tool, the material cannot flow either downwards or upwards, instead it "blows" out into the circular gap between the punch and the sleeve in the middle of the cylinder, forming a thin reinforcement flange wall around the center of the specimen. This method was discussed by Ran J. Q. et al. [16].

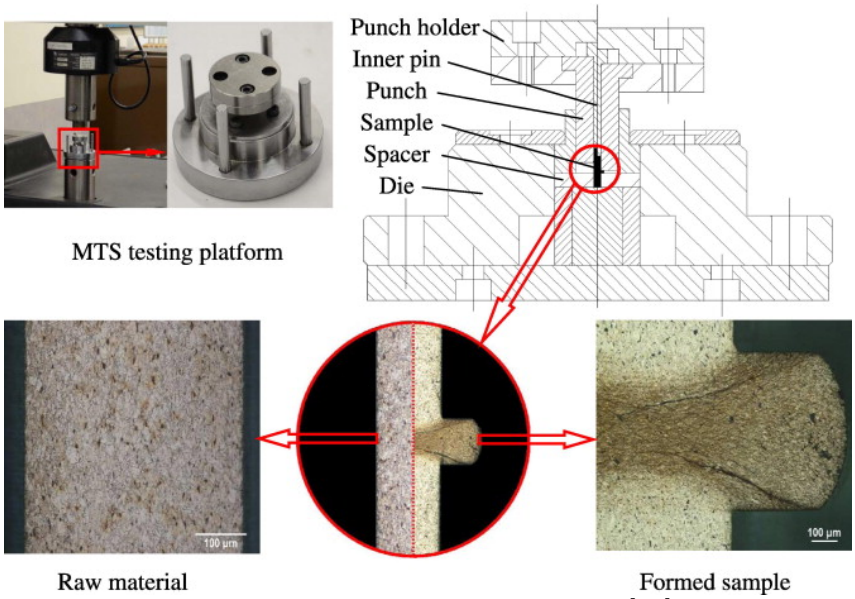

Figure 2.2: Micro-flange upsetting [16]

Therefore, the authors investigated the microflanged upsetting process, in which the compressed bar is radially expanded to form a flange in the middle. They proposed a hybrid "surface layer model" that divides the material into two groups of grains which can be seen in Fig. 2.3. The inner ones, which deform according to classical polycrystalline

theory (Hall–Petch effect and Armstrong crystalloplastic approach) and the surface ones, which deform more easily due to the free surfaces. The ratio of these components is expressed by the size factor η, which depends on the grain size d and the geometry of the specimen (diameter D, height h), and the resulting flow pattern is then the sum of the "bulk" component and an addition proportional to η [16].

The experimental part included heat treatment of C3602 brass in a vacuum furnace, which varied the grain size between 18 and 88 µm, and a series of upsetting tests on specimens of 2 mm and 0.5 mm diameter. The deformation was carried out on an MTS press at 0.01 mm/s and lubricated with oil to minimize the effect of friction and velocity dependence. Forces, paths, fracture surfaces, and scanning electron microscopy fractography were recorded [16].

Numerical modelling was performed in Abaqus with CAX4R elements for large deformations. The flow curve from the surface model was inserted into the plastic constitutive law and an extended Cockcroft–Latham criterion was chosen for the damage, in which the size factor η appears instead of the pure stress-strain integral. The evolution of damage is controlled by the energy required to open a unit crack area, eliminating the sensitivity to the size of the element [16].

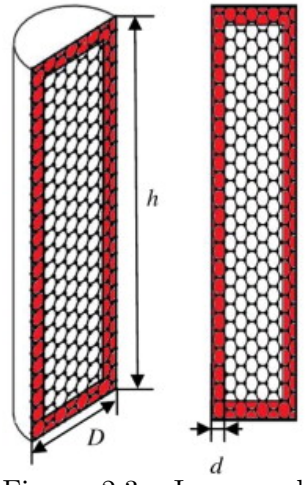

Figure 2.3: Inner and outer grains [16]

Comparison of the experimental and simulated flow curves for both macro and micro specimens showed that the model without size effect significantly overestimates the yield stress, while the surface model accurately reproduces the flow. The prediction of the fracture further indicated that the microspecimens did not reach the required "fracture energy" at the same height reduction (75 %) and therefore did not develop a continuous ductile crack as easily as the macrospecimens. Scanning electron microscopy confirmed that the macrospecimens ruptured at 45° and secondarily perpendicularly, while only small microcracks appeared in the microspecimens. The fractured surfaces were dominated by transgranular "dimples" whose size correlated with grain size [16].

The authors concluded that accounting for the high proportion of surface grains, i.e., the size effect, was crucial for accurate predictions of both flow and fracture in microforming. The surface layer model and the extended fracture criterion provided a reliable tool for the design of microforming processes in which grain size, geometric ratios, and process parameters had to be carefully chosen to avoid unexpected part failures [16].

2.2.2 Miniature testing for prediction of properties of a common size specimen

Testing of miniature solids does not always have to be performed just to determine the effect of size. Some studies have reported that miniature specimens can be used to predict material properties of normal-sized specimens in order to speed up the development of new material alloys, to reduce the volume of material needed for the production of test specimens, or to avoid the problems of producing specimens from, for example, strips or sheets from which commonly used standardized blanks cannot be produced. One such study is the study by Zhang L. et al. [17].

This study works with dual-phase steels, which combine soft ferrite with hard martensite and are at the core of modern automotive design due to their high strength in thin

sheets. The development of new steel alloys typically requires melting in batches of tens of kilograms, which is time and material consuming. Rapid Alloy Prototyping (RAP) speeds up this process by producing laboratory specimens weighing 20–140 grams, allowing up to a hundred compositions to be tested per week. However, to evaluate the mechanical properties of RAP specimens, the traditional ISO/EN A80 tensile body (80 mm gauge length) cannot be produced from thin sheet metal and therefore a miniaturized body suitable for 1–2 mm thick strip blanks must be designed [17].

In that work, tensile tests were performed on test bodies of different geometries (ISO/EN A80, A50, ASTM25, Mini1 and Mini2) on a Tinius–Olsen H25KS machine with strain sensing by an XSight 9 Mpx video extensometer. From the force–elongation curves, the authors evaluated the overall percentage elongation e_f, which they correlated with the so-called slenderness of the specimen $K = L_0/\sqrt{A}$ using the Bertelle–Oliver equation [17]

$$e_f = e_0 K^{-\alpha}, \tag{2.2}$$

where e_f, e_0, K and α represent the total elongation, the specific elongation (i.e., the percentage elongation normalized by the gauge length and the cross-sectional area), the slenderness ratio, and a material constant, respectively. High coefficients of determination ($R^2 > 0{,}97$) were obtained on log-log plots for both materials (DP600 and DP800), and therefore the validity of this correction was verified for miniaturized specimens with a specific length of 5–80 mm and a sheet thickness below 2 mm [17].

The limit curve for formation was derived from the tensile test data using the Keeler–Brazier formulation, where the key role is played by the work exponent n, determined from the Hollomon relation $\sigma = k\,\varepsilon^n$, and the sheet thickness. The anisotropy of the material was quantified by the plastic strain ratio r, calculated from the relation [17]

$$r = -\frac{\varepsilon_w}{\varepsilon_w + \varepsilon_\ell}, \tag{2.3}$$

where ε_w and ε_ℓ represent the width and length plastic strains, respectively, measured on specimens oriented 0°, 45° and 90° to the rolling direction [17].

The concept of miniature specimens in this thesis is not entirely identical to the concept of mini-testing explored, and particularly with reference to the dimensions of the miniature specimens used in this thesis and in the work of Zhang L. et al. [17]. This is a good example of how mini-testing can be used and in what direction it can be developed further.

2.2.3 Semi-automatic testing of miniature specimen

Beerli et al. [1] looks at miniature testing in terms of possible partial automation during testing, to ensure better results that will not be affected by influences that can arise from improper handling and at the same time, make testing more efficient [1].

In an effort to obtain plastic and fracture material parameters in locations where standard tensile specimens cannot be cut (e.g., in electronic components or thin films), the authors present a fully semi-automated system for mechanical testing of miniature specimens. The main concept involves the affine scaling of proven geometries of classical test bodies with factors of $\lambda = 5$, 10 and 20, and minimizing manual manipulation that could cause damage to very sensitive parts [1].

The actual test process can be divided into three automated phases:

1. **Insertion and form-fit clamping** – The specimen is inserted into the replaceable gussets in the frame, where it is preloaded to a fixed force (4 N, 2 N or 1 N depending on the dimension) to ensure seating without excessive preload. This prevents damage to the sensitive specimen arms during manual handling [1].
2. **Confocal thickness scan** – The entire frame is moved to a confocal measuring head made up of two high precision sensors which, after calibration, scan the specimen profile in increments of ±1 µm in the transverse direction and 5–20 µm in the longitudinal direction. This contact–safe measurement reveals the true thickness and its local variations, including roughness and wire EDM cutting effects [1].
3. **DIC in tensile test** – After moving under the optical assembly, a quasi-static tensile test is performed (speed 0.02 to 2.4 mm/min depending on the size of the specimen). Filming with a monochrome 5 Mpx camera with up to 6.5× zoom allows DIC analysis of surface deformation fields with a resolution of 0.77–5 µm/pixel [1].

A key benefit is the correction of the measured thickness for effects caused by the wire EDM. After applying a treatment that removes the effect of the thermally influenced layer, the engineering stress–strain curves of specimens of all three scales (large, medium, small) and of full 10mm specimens agree to within less than 1 % deviation in both strength and yield [1].

The validation performed in the study shows that the differences between the specimen types changed by less than 10 %. Therefore, it can be assumed that partial or total automation of miniature testing is possible in the near future and mini-testing could become a widespread and integral part of the determination of material parameters in the near future [1].

3 Hardening of the metals

To correctly interpret experimental results and subsequently calibrate material models, it is essential to understand the basic hardening mechanisms of metallic materials. This chapter summarises the theoretical knowledge of how size, temperature and strain rate influence material behaviour, and presents selected constitutive models that describe these phenomena. Since accurate calibration also depends on the quality of experimental data, an overview of commonly used testing procedures is included to clarify how such material characteristics are typically obtained. The review also covers the tools used in this study: the DIC method for strain measurements and the particle swarm optimisation (PSO) algorithm for determining material model parameters.

3.1 Description of hardening

The main cause of hardening of metallic materials is plastic deformation which occurs when the yield strength of the material is exceeded. Plastic deformation is considered to be a permanent, i.e. irreversible, change in the shape or dimensions of the observed component. The plastic deformation is always associated with an elastic part of the deformation, which returns to zero after the load is relieved, according to Hooke's law. In metallic materials, plastic deformation is caused by dislocation motion, where layers of atoms are displaced by one lattice vector after sliding over each other. Another mechanism may be the so-called twinning, which is less common and occurs when long-fibre flipping occurs. This mode of propagation of plastic deformation is important, for example, for ceramic materials [18, 19].

Plastic deformation also depends on the temperature and strain rate, with higher temperature or lower strain rate usually reducing the resistance of the material to plastic deformation. This causes the material to have a lower yield strength while lower temperatures and high strain rates make the material harder [18, 19].

3.1.1 Metallic Materials Hardening Mechanisms

Hardening means increasing the strength of a material, i.e. its ability to resist plastic deformation. From a microscopic point of view, strength is closely related to the resistance to movement of dislocations, i.e. the more obstacles that prevent dislocations from moving, the higher the stress (and therefore the higher the strength or hardness) is required to induce further plastic deformation. Thus, anything that acts as an obstacle to the sliding of dislocations can be considered as a stiffening mechanism. Mechanisms are usually divided into several subgroups according to the nature of obstacles, such as grain boundary obstacles, solid solution, precipitated particles, and other phases, such as increased density of dislocations. In practice, it is a general rule that the material solidifies due to several mechanisms simultaneously [18, 19].

- **Grain boundary hardening** – Grain boundaries play an important role in hardening of polycrystalline metals. The grain boundary itself is a barrier to the movement of dislocations, if the dislocation reaches the grain boundary, its further propagation

into the neighbouring grain is made more difficult. This causes polycrystals to be typically stronger and harder than single crystals as they contain a larger total grain boundary area which effectively hinders the movement of dislocations. This relationship is expressed quantitatively by the empirical Hall–Petch equation formulated by N. J. Petch and E. O. Hall in the 1950s [20, 21]. According to the Hall–Petch relationship, the yield strength R_e of a material increases inversely proportional to the square root of the average grain size d

$$R_e = \sigma_0 + kd^{-\frac{1}{2}} \tag{3.1}$$

where σ_0 and k are material parameters dependent on the purity and structure of the material. This relationship holds for a wide range of materials and grain sizes from common polycrystals to ultrafine grained materials [18, 19].

- **Solid solution hardening** – Another important mechanism is solid solution hardening, sometimes called as substitution/interstitial hardening. When admixture atoms of another element (metal alloying), which have a different size or modulus of elasticity than the base metal, are dissolved in the crystal lattice of a metal, a stress field is created around these foreign atoms to prevent dislocation motion during deformation. The dislocations are more difficult to move when passing through such a deformed lattice, accumulating around the impurity atoms and resulting in an increase in the strength of the material. This effect can occur in two ways: substitutional hardening, where the base metal atoms are replaced in the lattice by admixture atoms of a different size, or interstitial hardening, where smaller admixture atoms are mixed into the gaps of the crystal lattice [18, 19].

- **Precipitation hardening** – Many alloys, especially aluminum and nickel alloys or hardenable steels, use precipitation hardening. The principle is to exclude small second phase particles (called precipitates) from the supersaturated solid solution during appropriate heat treatment. These fine precipitates, dispersed within the crystalline grains of the matrix, then act as effective barriers to the movement of dislocations that get caught on them or have to flow around them, leading to an increase in the strength and hardness of the material. Typical examples are age-hardened aluminium alloys (e.g. duralumin containing $CuAl_2$ precipitates) or hardened tool steels with carbide precipitates [18, 19].

- **Deformation hardening** – The last key mechanism, that operates especially in cold forming of metals, is deformation hardening. This hardening is caused by the increase in dislocation density during plastic deformation and the interaction of newly formed dislocations. As mentioned above, plastic deformation increases the number of dislocations in the material and decreases their average spacing. The dislocations become entangled with each other and form a complex network within the crystals, thus becoming obstacles to themselves. Each new dislocation encounters other, no longer moving dislocations and must overcome the resistance of their stress fields. In practice, this means that after some previous plastic deformation, the metal has a higher yield strength and hardness than before the deformation. This phenomenon is also called work hardening or strain hardening [18, 19].

In addition to the main mechanisms mentioned above, there are other ways of increasing the strength of metallic materials. These include, for example, transformation hardening using martensitic transformation. When steel is hardened by heating to austenitizing temperature and then rapidly cooled, most of the austenite is converted to martensite, which forms a hard and brittle phase with supersaturated carbon and high dislocation density [18, 19].

3.2 Influence of external parameters and its material models

3.2.1 Strain rate

The rate of deformation has a major influence on the plastic behavior of metals. As the rate of deformation increases, the stresses required to propagate dislocations generally increase. Dislocations that cause plastic deformation have a limited rate of motion. In the case of slow loading, the dislocations can move relatively easily to overcome obstacles. However, if the rate of deformation increases, they do not have sufficient time to overcome obstacles, which may lead to their accumulation or stoppage, and thus the material generally exhibits a higher strength than in cases of low loading rates. It appears that at high velocities the so-called phonon drag starts to dominate. Thus, higher stresses are required to maintain the same rate of deformation. The material behaviour thus transitions into velocity–dependent hardening. At extremely high strain rates, it has been observed that the metal heats up locally and can harden unexpectedly, and the dislocations then move ballistically with significant drag [22, 23]. Example of models for the dependence of strength on strain rate:

- **Cowper–Symonds model** –The dynamic yield stress σ_d is derived from the static one σ_s according to the empirical relation [24, 25],

$$\sigma_d \;=\; \sigma_s \left[1 + \left(\frac{\dot{\varepsilon}}{C}\right)\right]^{\frac{1}{p}} \tag{3.2}$$

  where $\dot{\varepsilon}$ is the strain rate, C and p are the material constants. This model is often used in impact load simulations due to its simplicity and ease of calibration.

- **Johnson–Cook model** – The Johnson–Cook model is a phenomenological description involving three main effects – plastic hardening, velocity hardening and thermal softening. This model will be discussed in more detail in the next section of the thesis [26].

3.2.2 Temperature

Plastic deformation in metals usually becomes easier as the temperature increases. Dislocations are able to overcome obstacles more easily, reducing the yield strength and the original change in strength. Due to the higher temperature, diffusion is increased, resulting in a decrease in dislocation density and thus less hardening. The progression of deformation can be divided into several stages: First, hardening work dominates (stage I), then (stages II–III), gradual dynamic recovery, and eventually recrystallization lead

to softening of the material, until in the final state (stage IV) a balance between hardening and softening occurs [27]. Here are several examples of models of the dependence of strength on temperature change:

- **Johnson–Cook model** – Again, the Johnson–Cook model could be used, combining not only the effect of strain rate but also the effect of temperature change [26].
- **Zerilli–Armstrong model** – The Zerilli–Armstrong model is an alternative to the Johnson–Cook model. For material modelling, the modified variants of the Zerilli–Armstrong model are used. For example:

$$\bar{\sigma} = \sigma_{0G\varepsilon} + B\exp(-\beta T) + B_0\left[\varepsilon_r\left(1-\exp\left(-\frac{\varepsilon}{\varepsilon_r}\right)\right)\right]\exp(-\alpha T) + k_\varepsilon \ell^{-\frac{1}{2}} \quad (3.3)$$

  where $\sigma_{0G\varepsilon}$ is athermal stress, which depends on the dislocation density, subgrain structure and impurity content, B, β, B_0, ε_r and α are constants determined experimentally, ε is the plastic transformation and T is the temperature, ℓ is grain size and k_ε is the Hall–Petch coefficient, which expresses the hardening of the material due to decreasing grain size [28].

  The Zerilli–Armstrong model is used primarily for predicting the flow stress of metallic materials at high strain rates and over a wide temperature range, especially where temperature and rate sensitivity of plastic deformation are important. Due to its construction based on the theory of thermally activated dislocation, the model allows to quantify and distinguish the contributing mechanisms (strain hardening, strain rate hardening, thermal softening) for different crystal structures (body–centered cubic vs. face–centered cubic) [29, 30, 28].

3.2.3 Size

When the size of the material is reduced to the microscopic level, its mechanical behaviour changes significantly compared to the macroscopic scale. This phenomenon, referred to as the size effect, is significantly manifested in micro-forming processes and affects material properties, deformation, fracture behaviour and damage accumulation mechanism. Due to this effect, conventional material models and analytical methods for macroscale specimens are no longer applicable at the microscale.

The cause of the size effect is a reduction in the number of grains in the deformation zone, which means that individual grains have a more pronounced effect on the overall deformation behaviour. The behaviour of the material is influenced not only by the grain size itself, but also by the orientation, position, properties, and dimensions of the specimen [31, 16, 32, 33, 34, 35].

There are two main types of size effect:

- **Grain size effect** – occurs when the grain size changes at constant specimen dimensions.
- **Geometry size effect** – occurs when the specimen size changes at constant grain size.

Tensile tests on copper sheets showed that a decrease in the thickness to grain size ratio leads to a decrease in fracture stress, fracture strain, and the number of micro–cavities on the fracture surface. For thin metal sheets, it was also found that the yield strength and the maximum strength decrease with decreasing grain number over thickness. However, if the grain size exceeds the thickness of the specimen, the yield strength value may again increase slightly.

In standard macro-forming processes, the proportion of surface grains is negligible. However, it increases significantly at the micro-scale. Surface grains are less mechanically constrained, leading to lower hardening and lower resistance to deformation and rotation. This causes a reduction in flow stress, promoting micro-cavity coalescence and crack growth through the thickness of the material [31, 16, 32, 33, 34, 35]. Size–dependent strength models are:

- **Surface layer model** – The surface layer model describes the flow stress of the material by the relation [31]:

$$\bar{\sigma} = \eta_s \sigma_s + (1 - \eta_s)\sigma_i \tag{3.4}$$

  where $\bar{\sigma}$ is the resulting flow stress, σ_s is the flow stress of surface grains, σ_i is the flow stress of internal grains, $\eta_s = N_s/N_w$ is the ratio of the number of surface grains N_s to the total number of grains N_w.

  This model explains why the flow stress decreases with miniaturization due to the surface grains being less resistant to deformation and dominating the overall behaviour of the material [31].

- **Strain gradient plasticity model (SGP)** – SPG is an extension of classical plasticity that takes into account the effect of spatial changes in plastic strain on the mechanical behaviour of the material. Although conventional theories work only with the magnitude of the plastic strain, the SGP model adds a dependence on its gradient, specifically the effective gradient η_p. This approach allows modelling size effects observed on the micrometer scale, such as the higher strength of thin specimens, which conventional plasticity cannot explain [36, 37, 38].

  The flow stress within the SGP model is described by the relation [36]:

$$\bar{\sigma} = \sigma_{\text{ref}} \sqrt{f^2(\varepsilon_p) + l\eta_p} \tag{3.5}$$

  where σ_{ref} is the reference stress, $f(\varepsilon_p)$ is the nonlinear plastic strain function, l is the internal material length, and η_p is the effective plastic reshaping gradient.

  In the FEM, the SGP model is implemented in such a way that the spatial derivatives of the plastic deformation are numerically evaluated at the integration points. The model is mainly used to simulate the behaviour of micro-structures such as thin films, micro-columns or regions around crack tips where strain gradients are significant and size effects play a major role. This allows SGP to better predict increased strength, stiffening, and altered stress distributions in microstructured materials [36, 37, 38].

3.3 Common experimental procedures

In general, material properties are divided into four basic areas (elasticity, plasticity, strength and toughness). However, the mechanical properties are many and need to be addressed. The different areas usually contain several different mechanical characteristics that are described - for example, elasticity contains Young's modulus or Poisson's ratio. The uses of mechanical testing are numerous. They are widely used for the design and calculation of structures, in the manufacture of materials to verify their quality, or for the design of technological processes in the further processing of materials [39].

For better clarity and usability, the tests are defined by standards. Mechanical testing standards establish rules and procedures for the testing of materials to ensure accuracy, repeatability and comparability of results. These standards define the conditions, methodologies and requirements to be followed when testing the mechanical properties of materials [39]. The standards define a range of tests for the mechanical properties of the material. The most commonly used are the following.

- **Tensile test** – is used to determine tensile strength, yield strength, ductility and modulus of elasticity [40, 41, 42].
- **Compression test** – tests the resistance of a material to compression, often used for brittle materials [43].
- **Bending Test** – tests the strength and flexibility of a material in bending, used for metals, plastics and composites [44].
- **Hardness Testing** – measures the hardness of a material by various methods such as Brinell, Vickers or Rockwell [45, 46, 47].
- **Impact Test** – evaluates the toughness of a material under sudden loading, e.g. using a Charpy hammer [48].
- **Fatigue Test** – tests the resistance of a material to cyclic loading, important for long-term durability [49].
- **Creep Test** – monitors the behaviour of the material under long-term loading at elevated temperatures [50].

Individual tests can take a number of forms in which different initial conditions or environmental influences and test parameters will affect the resulting mechanical properties. This is particularly important in cases where it is necessary to describe the material under several different loading conditions. All experimental data used in this work were determined by the **tensile test**.

3.4 Digital image correlation

Determining the effect of size on the hardening of metallic materials presents certain pitfalls. One of these is how to accurately determine the deformation of the specimen during testing. For this thesis, it is important to know mainly the value of the reaction force and elongation of the specimen. However, miniature testing is a very costly and time consuming activity, so it is advisable to capture as much data as possible about the material behavior during testing. Since the nature of the specimen does not allow the use of conventional extensometers or strain gauges, DIC method is used.

DIC is non-contact optical method which is widely used in experimental mechanics and materials science, and it is able to measure surface deformation and displacement [51, 52]. DIC operates by tracking changes between the unique patterns monitored in the area of interest under load. The unique pattern, either the natural texture of the specimen or the applied stochastic speckle pattern, is captured in the digital images. The pattern should be high-contrast with at least 50 % filling. The specimen of the pattern used on miniature specimens is in Fig. 3.1 compared to the specimen with the surface of production. By comparing images, DIC software is able to calculate the full-field or uniaxial displacement and strain across the surface of the object. The ability to generate detailed deformation maps sets DIC apart from traditional point-based measurement methods, such as strain gauges and extensometers [51, 53].

Figure 3.1: Unique pattern used on miniature specimen compared to the original surface [54]

This makes DIC one of the most widely used engineering applications of materials testing. The fact that this method is non-contact makes it very convenient when working with small specimens or wherever physical contact between the specimen and the measuring equipment could affect the test results. For small specimen tensile tests, which are necessary to determine the effect of size on the strength of metallic materials, DIC can provide complete information on the mechanical properties of the material, including Young's modulus, Poisson's ratio and strain distribution. By scanning the entire surface area, DIC can reveal material mechanic responses that are difficult to determine using conventional testing methods [51, 52].

3.5 Particle swarm optimization

In order to accurately calibrate the parameters of advanced material models based on experimental data, it is essential to employ reliable and efficient optimization techniques. Traditional methods may struggle with the complexity and nonlinearity of material behavior, especially when multiple influencing factors such as strain rate, temperature, and specimen size are present simultaneously. PSO a population-based metaheuristic algorithm inspired by natural behavior, has proven to be a powerful tool for solving such inverse problems in engineering applications. This chapter presents the fundamental prin-

ciples of the PSO algorithm and its implementation in MATLAB, which was used in this thesis to identify the optimal parameters of the Johnson–Cook material model from true stress–strain data.

PSO is an evolutionary optimization algorithm inspired by the behavior of swarms of birds or fish that move collectively in search of food. Each individual point in the swarm, called a particle, represents a potential solution to the optimization problem. PSO thus solves the problem by iteratively improving the population of the candidate solution of the chosen quality measure. The particles move in the defined search space based on their own experience (best solution found) and the experience of the entire swarm (global best solution). The algorithm iteratively updates the position and velocity of the particles using simple equations, allowing the search for the global optimum function. The particle swarm is known for its simplicity, flexibility, and ability to efficiently search for optimal solutions in multidimensional spaces [55]. This method was first described by Kennedy and Eberhart in 1995 [56], when it was originally intended to model the social behavior of a swarm of birds or fish, but proved to serve very well for optimization problems once simplified [56].

3.5.1 The principle of the algorithm

The basic PSO algorithm works by having a certain population or a swarm of candidate particles to solve. Then, the particles move and search the defined space according to a few simple patterns. The movement of the particles themselves is governed by their own position in the searched space and also by the known position of the entire swarm. This process is then repeated until an exact solution is obtained. However, obtaining an exact solution is not always guaranteed [55, 57].

Formally, let $f : \mathbb{R}^n \to \mathbb{R}$ be the objective function we want to minimize. The function f takes as input a candidate solution in the form of a vector of real numbers and returns a real value that indicates the quality of this solution. The gradient of the function f is unknown. The task is to find a solution a such that $f(a) \leq f(b) \quad$ for all b in the search space, which guarantees that a is a global minimum [55, 57, 58].

Let S denote the number of particles in the swarm. Each particle i has a solution in the solution space $x_i \in \mathbb{R}^n$ and velocity $v_i \in \mathbb{R}^n$. It is important to remember that: [55, 58]

- p_i: is the best position of the particle i found so far,
- g: is the best positon of the whole swarm so far.

The basic PSO algorithm for minimizing the function f is shown in Fig. 3.2 and can be systematically described as follows: [55, 56, 58]

1. Initialization of positions x_i and speed v_i randomly.
2. Repeat until the termination condition is met:
   (a) Speed update
   $$v_{i,d} \leftarrow w\, v_{i,d} + \phi_p\, r_p\, (p_{i,d} - x_{i,d}) + \phi_g\, r_g\, (g_d - x_{i,d}), \tag{3.6}$$
   where w is inertia, ϕ_p, ϕ_g are cognitive and social coefficients, $r_p, r_g \sim U(0, 1)$.
   (b) Position update
   $$x_i \leftarrow x_i + v_i. \tag{3.7}$$

(c) Update p_i and possibly g if the new position has produced a better value f.

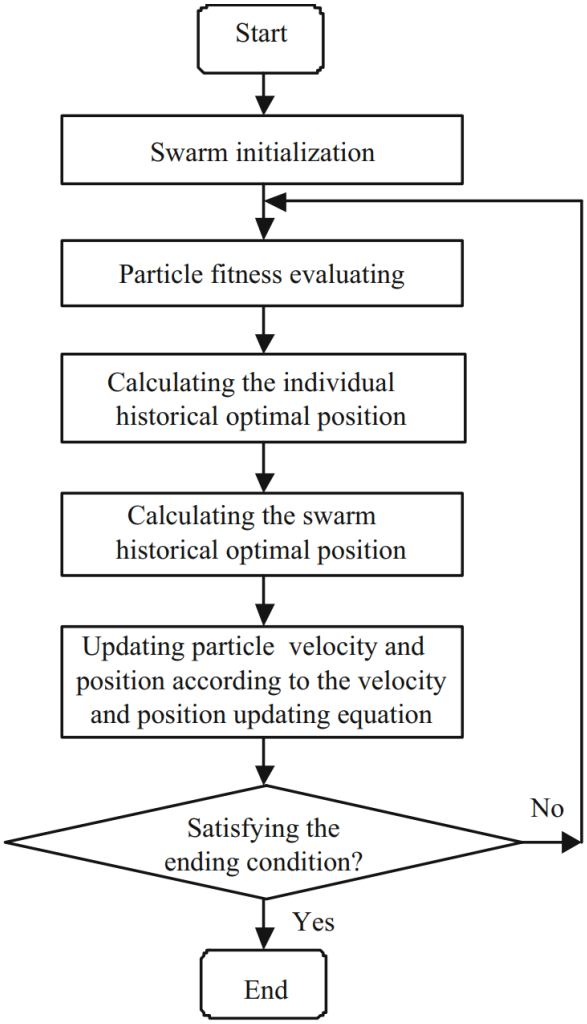

Figure 3.2: Graphical representation of PSO algorithm [55]

3.5.2 PSO in MATLAB

In MATLAB, PSO is implemented within the `Global Optimization Toolbox` package using the `particleswarm` function, which accepts a handle to the objective function, a number of variables, and (optionally) lower and upper bound vectors as input. The initial particle swarm is randomly initialized with positions x_i and velocities v_i. In each iteration, MATLAB updates the velocity according to the constriction approach [59, 60]:

$$v \;=\; W\,v \;+\; y_1\,u_1\,(p-x) \;+\; y_2\,u_2\,(g-x), \tag{3.8}$$

where W is the constriction coefficient, y_1 and y_2 are the cognitive and social weights, respectively $u_1, u_2 \sim U(0,1)$. The position is then adjusted as

$$x = x + v. \tag{3.9}$$

Parameters such as the swarm size, maximum number of iterations, inertia range or weights y_1 and y_2 are set by the options object [61]

`options = options('particleswarm',...)`.

There are also advanced options such as parallel evaluation (`UseParallel`), hybrid result tuning (`HybridFcn`) or custom functions for initializing and updating the swarm, allowing PSO to be adapted to a wide range of optimization tasks [59, 60].

4 Modifications of a testing device

In order to determine the effect of size on hardening, it is necessary to carry out the experiments with small or miniature specimens.. The geometry of small specimens has already been proposed by Patrik Salvet [31]. In the same thesis, the miniature specimen device and the whole apparatus were used [62, 63].

During the testing and calibration at that work, it was found that certain parts needed improvement – for example the camera holder, the clamping and some other parts, and at the same time remove some measurement errors. For this reason, it was necessary to modify the selected parts of the test apparatus prior to performing the experiments.

4.1 DIC camera holder

The first part which needed to be improved was a camera holder. The camera was used to read the elongation of the specimen accurately. This is because for such small specimens, it is not possible to use a commonly used extensometer or other equipment that is directly attached to the specimen, and so image-based methods are used to measure the deformation.

In previous works [31, 64] the AZURE – 6505THM lens was used [65]. Therefore, the camera holder was originally designed with this lens and its dimensions in mind. In the course of modifications and testing of the test apparatus, another lens was chosen, which has better recognition capabilities, and thus the results obtained will be more accurate. Therefore, the camera holder was modified in the process, specifically the DIC camera lens attachment part 4.1.1. Thus, in the following description, only the final design of this holder is mentioned and described, which is based on the newly used lens.

Figure 4.1: DIC camera lens TC3MHR016–C [66]

The new lens type is OPTO Engineering TC3MHR016–C shown in Fig. 4.1 was used with the FLIR Blackfly S BFS–U3–88S6M–C DIC camera. All specifications of the camera lens as focal length dimensions and other information are available on the manufacturer's

website [66]. The data sheet with information needed to design the mount, including 3D data in STEP format and others that were used for visualization and functionality checks during the design of the mount in Autodesk Inventor 2023 is also available on the website. Since this camera lens (also the previous one) has a fixed focal length and different specimen types have different dimensions or will have a slight shift in the planes or space when clamping them, it is necessary to precisely locate the camera position to focus the specimen area for each specimen separately.

The main goal in designing the new mount was to ensure camera movement in all three axes with the highest possible accuracy and rigidity of the holder. For the holder production and due to previous experience, a 3D printing machine was chosen for the production, which enables fast production and possible modification of individual parts within a few hours or days. This was very helpful in the development and prototyping of the holder. In addition, today's modern 3D printers achieve sufficient manufacturing accuracy for the production of the holder. In addition, steel components have been added to its design to enable movement while maintaining sufficient precision.

4.1.1 DIC camera lens attachment

Since the camera itself is light in relation to the lens and the center of gravity of the entire assembly is in the lens section, the clamping behind the lens was chosen. When designing the clamping part, the most important parameters are the lens diameter $D_{lens} = 37.7$ mm and the fixed focal length, respectively, fixed working distance $w_{dist} = 43.1 \pm 3$ % mm. The fixed focal length is the main reason for the creation of the whole holder.

A two–piece clamp is designed to hold the camera lens firmly in place. This clamp is supplemented with a pressure part that allows to create more pressure on the lens, which is then firmly held in place. The two parts of the sleeve are connected by a series of four bolts and nuts that ensure firm contact between the two parts, supplemented by one bolt and nut which serve to create pressure on the lens through the pressure part. The whole lens clamp assembly is shown in Fig. 4.2.

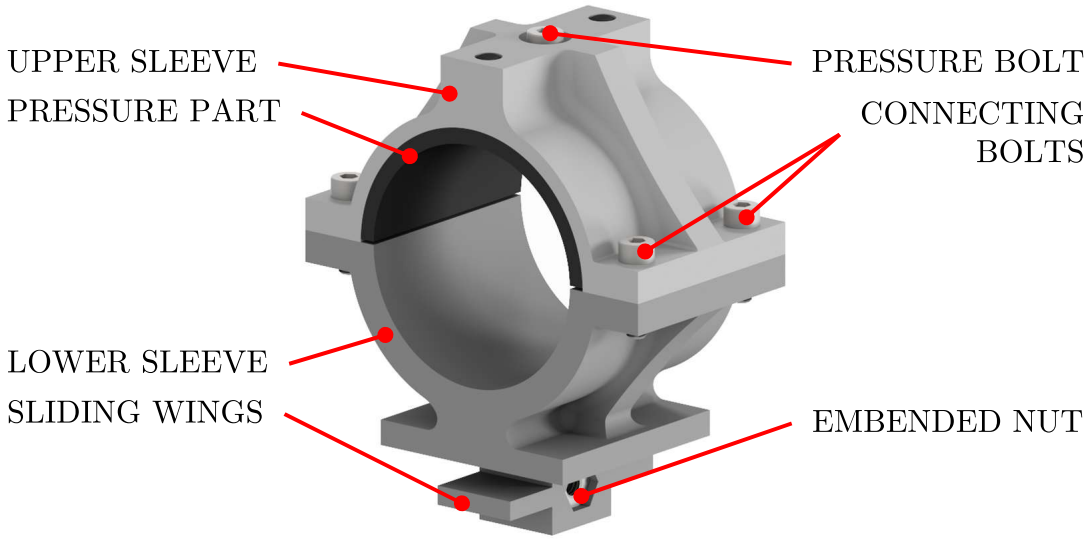

Figure 4.2: Clamp of the camera lens

4.1.2 Movement in the x and y axes

For movement in the x and y axes (the xy-plane passes normal to the loading direction of the specimen, the loading axis is marked as the z-axis), friction surfaces in the form of "wings" fitting into a slot in the counterpart were used. These wings ensure that the part cannot rotate around the axis of the motion screw. Their perpendicular surfaces then ensure fixation with respect to the z-axis and the component can only move in a translational motion.

A precision threaded rod with a low pitch thread was used to ensure precise movement. To convert the rotary motion into translational one, nuts are used through which the threaded rod passes. The nuts are inserted into hexagonal holes in the 3D printed part, preventing the nuts from rotating. A handle was attached to the end of the threaded rod to allow rotation. To move the camera in the desired direction, it is sufficient to turn the screw handle. The whole mechanism can be seen in Fig. 4.3.

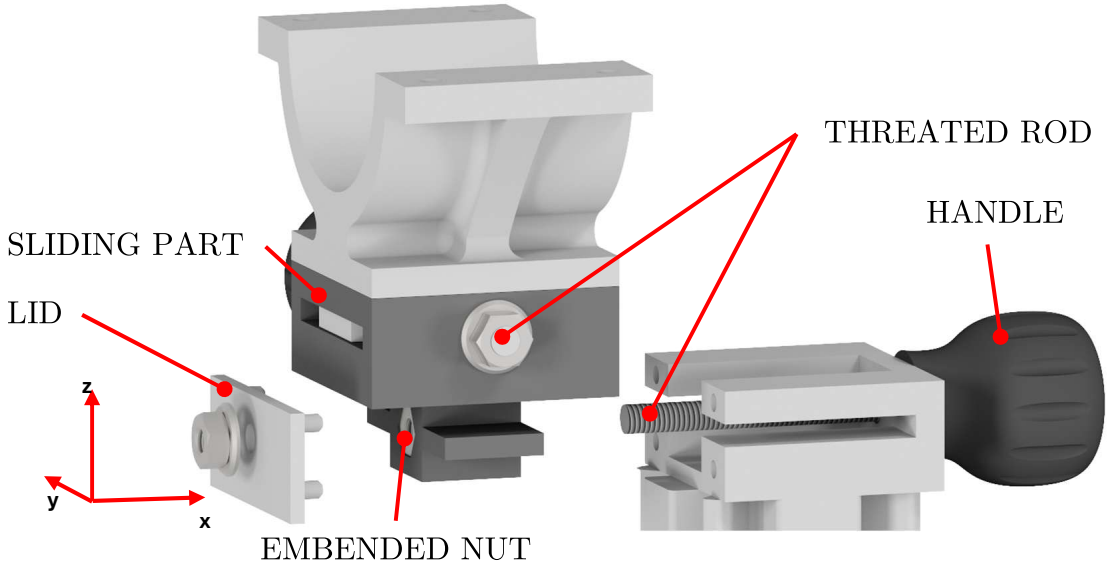

Figure 4.3: Translational mechanism in x and y axes

4.1.3 Movement in z axis

Similarly to the x and y axis displacements, the z axis displacement is designed in a similar way. The only difference is that the wings are placed in the shape of the letter x and are supplemented with additional friction surfaces between the standing part and the sliding part.

To ensure a more precise and smooth movement when extending the holder in the z-axis and to increase the rigidity of the entire structure, a linear guide was used. The linear guide consists of a smooth rod and a linear bearing. The rod is firmly pressed into the stand of the holder and the bearing is inserted into the lifting part, and two threaded rods with a knob are placed in the mount to move the camera in the z-axis. This part of the holder is in Fig. 4.4.

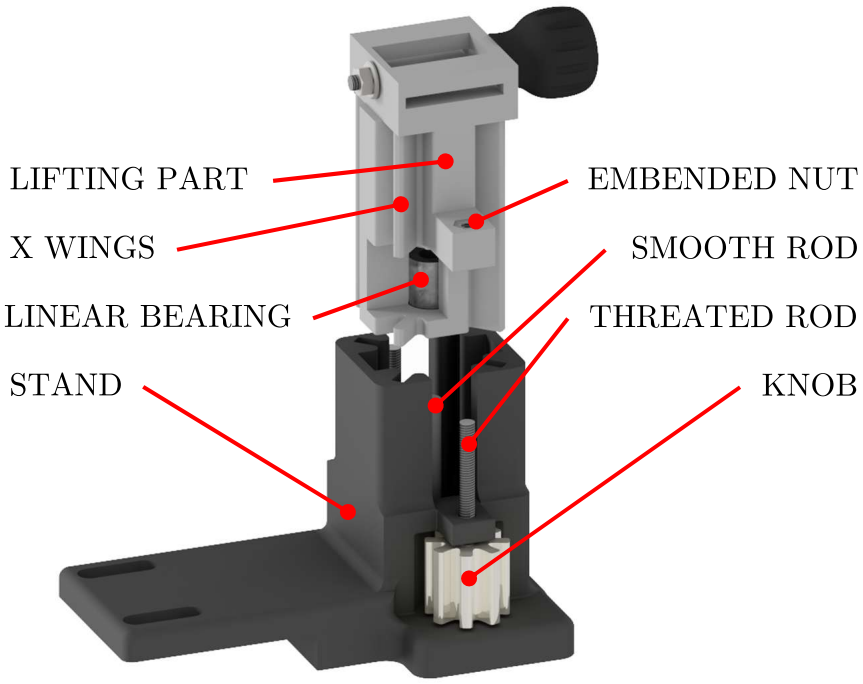

Figure 4.4: Translational mechanism in z axis

As can be seen, two screws are used for a firm connection of the holder and the rest of the apparatus. The holes for these screws can be seen in Fig. 4.4 and the complete design of the mount, including the DCI camera lens, is shown in Fig. 4.5.

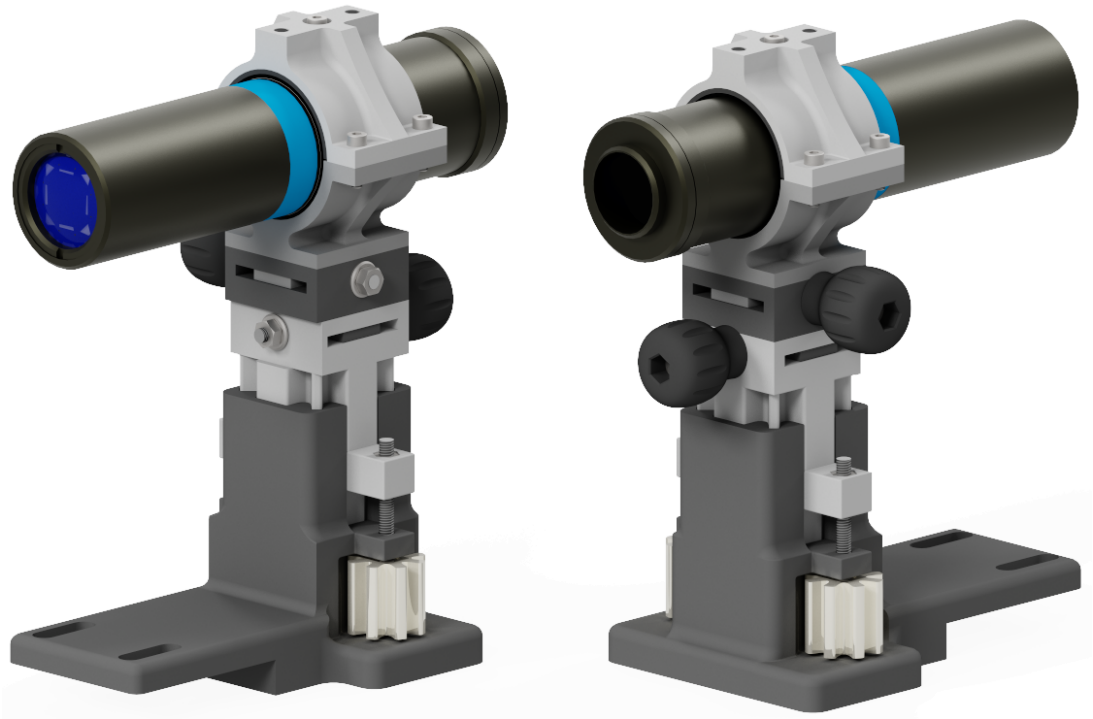

Figure 4.5: Model of camera holder

4.1.4 Production and comparison

As already mentioned, 3D printing was used to produce the camera holder. Specifically, the Prusa MK4 printer was used. The Prusa MK4 is a desktop FDM 3D printer that uses Fused Deposition Modelling (FDM), in which plastic filament is melted in an extruder and applied layer by layer according to the model. Offering a print volume of 250 × 210 × 220 mm, it features a 32-bit xBuddy baseplate and a new Nextruder extruder with precise material feed control. The 0.4 mm nozzle reaches temperatures of up to 300 °C, while the heated pad with flexible PEI sheet can be heated to 120 °C. Automatic calibration and an Input Shaper system minimize vibration, allowing accurate printing at speeds of up to 200 mm/s. The printer supports layer height adjustment from 0.05 mm to 0.30 mm, with positioning accuracies quoted as 0.01 mm on the X/Y axis and 0.002 mm on the Z axis, but these accuracies are dependent on the specific setup, alignment, and technical condition of the printer [67].

The material used for the printing was Prusament PLA Gravity Grey - that is a high–quality material developed specifically for Prusa printers and in combination with Prusa MK4 ensures high precision and print quality [67]. PLA (polylactide) is a biodegradable thermoplastic material made from renewable resources, such as corn starch or sugar cane. Its low melting temperature (approximately 180–200 °C), minimal shrinkage, and ease of printing make it one of the most widely used filaments for FDM 3D printing. Its technical characteristics are quite sufficient for the prototyping and production of similar products such as this holder. The complete manufactured holder and its comparison with the previous type used is shown in Fig. 4.6.

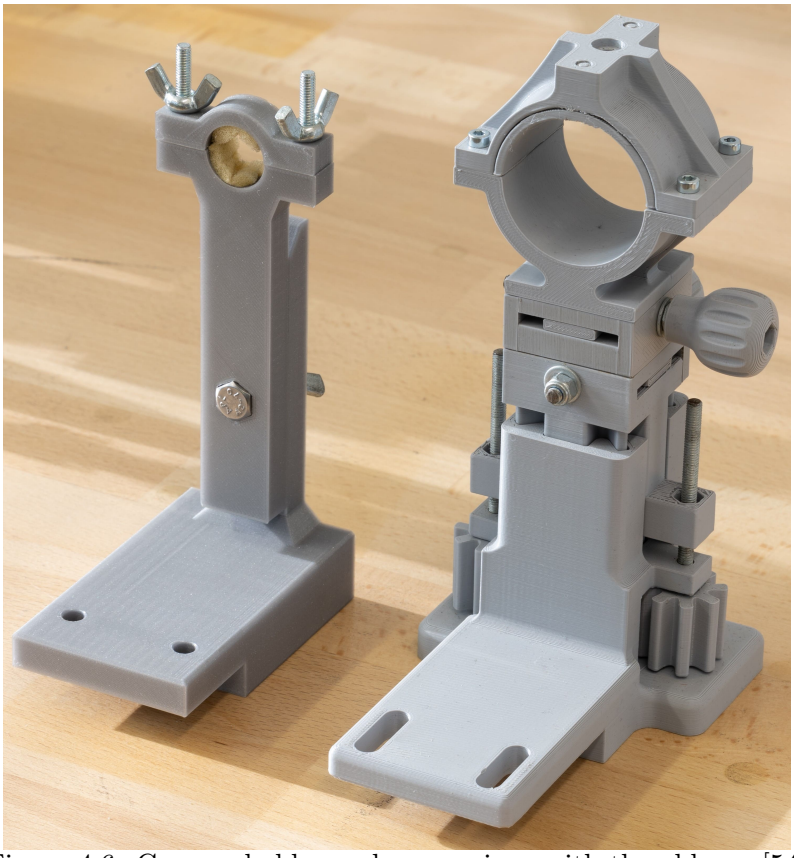

Figure 4.6: Camera holder and comparison with the old one [54]

4.2 Clamping of the specimen

Another part that needed to be improved was the specimen clamps. The problem with the old clamps was the clamping force when the old clamps had only one screw that put pressure on the clamped part of the specimen, and somehow the specimen could slip out of the clamps during testing. Moreover, testing of high–strength materials is planned.

For this reason, a search was carried out to find the best clamping option. There is the option of wedge attachment which is used for conventional flat specimens or composites. The advantage of this solution is that the compressive force on the specimen increases as the tensile force increases, thus holding the specimen firmly in the clamp. A frequently used solution for miniature specimens is the firm contact between the clamp and the clamping part of the specimen by means of a pin or edge of the specimen. This offers a solution similar to, for example, those used in [68, 69].

Unfortunately, these solutions are not suitable for use in this device. One of the problems would be the cost of manufacturing. However, the main problem remains one of space since there is not enough space on the current instrument to allow such a large change of clamping parts, which would be significantly more space consuming. This type of clamping and the search for possible better solutions may be useful when developing a new test machine, not when modifying the existing one.

That is why the clamps were designed based on the shape of the type already used with the difference that two bolts with nuts were used. An important dimension was the spacing of the screws, which had to ensure that the clamping part of the specimen could be inserted between the screws. At the same time, the dimensions of the new clamps had to fit the connection parts of the test equipment. The shape of the designed clamps is shown in Fig. 4.7.

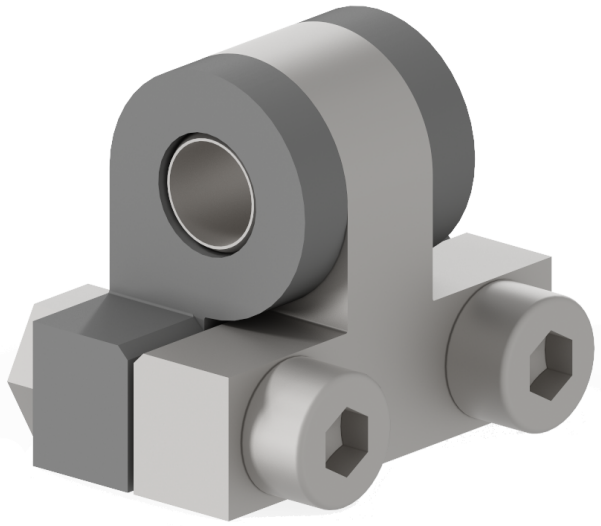

Figure 4.7: New specimens clamps

As the clamps will be under considerable stress by pressure and to avoid damage to the clamps, it is necessary that the material of these is stronger than the material of the specimens, tool steel 1.2312 according to DIN EN ISO 4957 was chosen for the production of these clamps and the entire surface of the clamps was nitrided to a depth of 0.25 mm, achieving a surface hardness of 60 ± 5 HRC to improve its properties. It is

also crucial to maintain a high level of precision in their manufacture so that their contact surfaces fit together as accurately as possible and so that measurement errors caused by large clearances in the system do not arise. All prescribed dimensions and tolerances are entered into the drawings in Figs. 4.8 and 4.9.

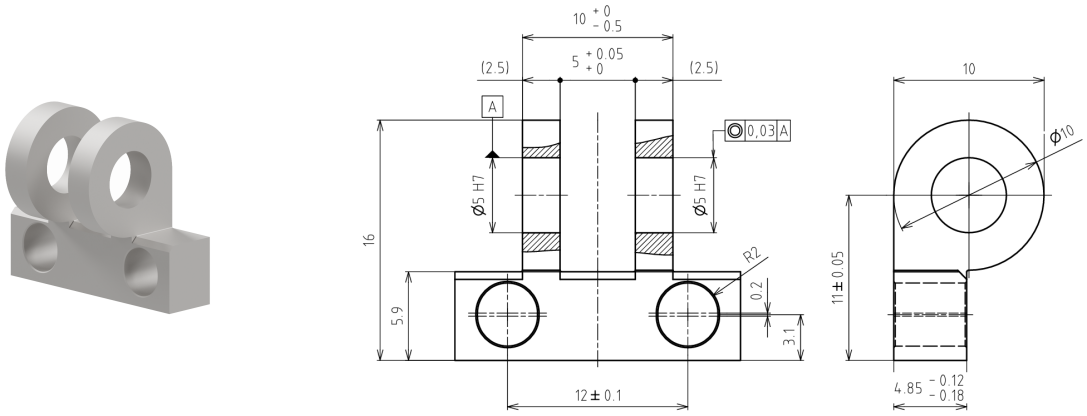

Figure 4.8: Drawing of clamp 1 (dimensions in mm)

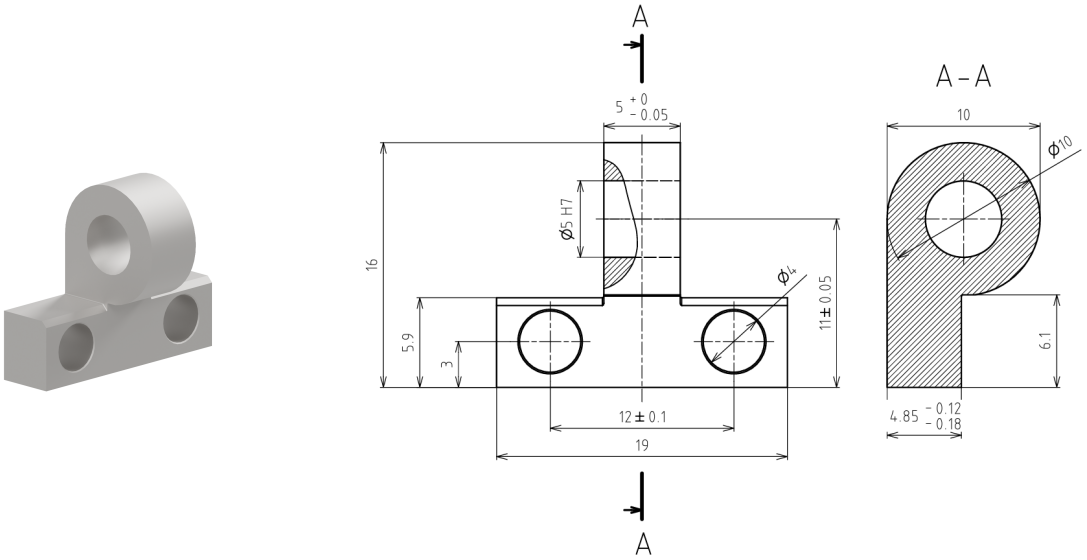

Figure 4.9: Drawing of clamp 2 (dimensions in mm)

As can be seen from the drawings in Figs. 4.8 and 4.9, the surfaces that are in contact with the clamping part of the specimen have a clearance of about 0.3 mm between each other. The gap between clampers can also be seen in Fig. 4.7. This is in order to make the clamp and specimen surfaces as close as possible when inserting the test body. If the clamp faces were made without clearance, the squeeze can be loose when the specimen is inserted, and the specimen could slip during measurement. If the clearance were too great – in extreme cases or when testing very soft materials – the clamps could dig into the specimen, deforming the specimen and creating an indentation in which the stresses would concentrate, and the specimen would break and deflect in that indentation. Since most of the specimens that will be tested will be 0.3 mm thick, a clearance of only 0.3 mm was created in the clamps. The three described cases are shown in Fig. 4.10.

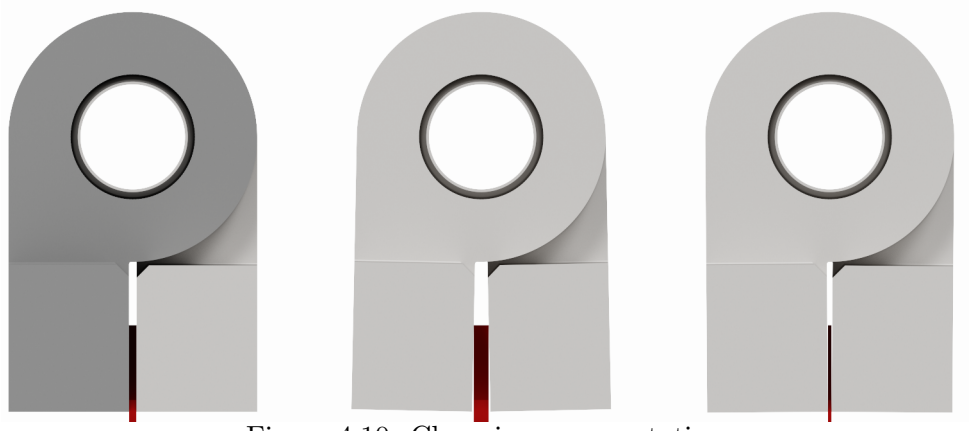

Figure 4.10: Clamping representation

As a result, the designed clamps meet the required properties to enable the experiment to be carried out.

4.3 Joint and centering fixture

One of the main changes made to the test device is the replacement of the lower crossbar which, like the upper one, served to attach the clamp and was guided against possible rotation on two vertical guide rods.

Placing the crossbar on two guide rods was technically advantageous in preventing the clamps from being offset and rotated relative to each other. However, currently, it presents a problem in clamping the specimen and tying it properly in the clamps due to lack of space. Therefore, a new clamping method has been devised, but it will require a change in the clamp mounting and the removal of the bottom crossbar. In addition, it is not advisable to have any other element between the specimen and the load cell that could even marginally affect the reaction force measured in the load cell, for example, by frictional force on the guide rods, even if the surface of the guide rods was ground and lapped during manufacture and had very little surface roughness.

Based on this information, this entire piece of testing equipment needs to be replaced. One of the main problems was ensuring uniaxial tension in the specimen.

4.3.1 Normalized and designed parts of joint

To maintain uniaxial load, it is best to use a joint that ensures that the specimen does not bend or rotate in any way due to error during clamping.

The most suitable type of joint would be a spherical joint which would allow rotation in all directions, and thus ensure that only the tensile force is transmitted. However, as this joint would be difficult to manufacture and could be disconnected under tensile loads, a two–axle joint, generally known as a **gimbal**, was chosen.

This type of joint is very common and is used in a wide range of engineering applications making it possible to buy it as a normalized part. As it is necessary to ensure that the entire joint is not too large and long due to the limited space of the mini-tester, a joint with the marking GU 01 E was chosen. The exact specifications, dimensions, and further details can be found in the manufacturer's catalog [70]. The joint is shown in Fig. 4.11.

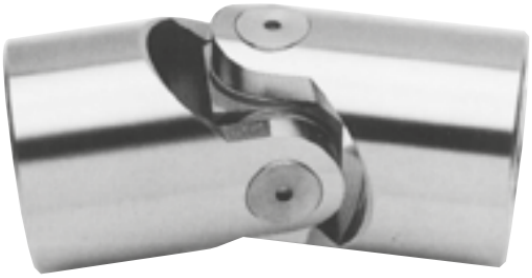

Figure 4.11: Universal joint GU 01 E [70]

As mentioned above, joint length could be problematic. Therefore, the joint was disassembled into parts and only some of them were used with combination of the manufactured parts.

A bolt was designed to connect the joint to the load cell and an H coupler was designed to connect the joint and clamps. The standardized joint GU 01 E is designed so that other parts are connected to it by pressing into the face holes. For this reason, it is necessary to design the bolt correctly to hold it firmly in connection with the joint. Therefore, a fit with an overlap was chosen. All the dimensions of the bolt are shown in Fig. 4.12.

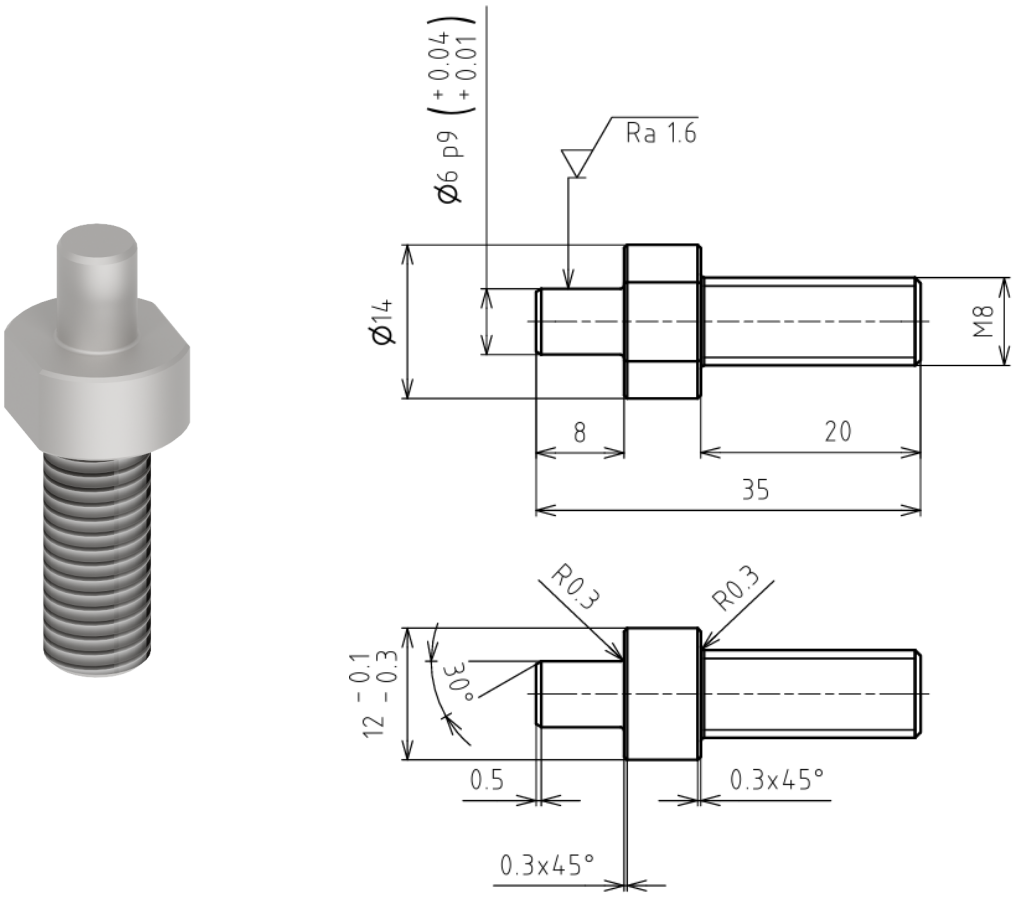

Figure 4.12: Bolt to connect the joint and load cell (dimensions in mm)

On the head of the bolt in Fig. 4.12, two flat surfaces are visible. These surfaces can be used when the entire joint is assemble into the testing device. The bolt can be

attached to these surfaces with a wrench or pliers, and the joint can be mounted in the test device.

Another part is the H coupler which has been designed so that one of the joint parts can be replaced by this coupler. The parts that connected the original part of the joint were used for the connection. Thus, only the H coupler was made and then assembled with the rest of the part of normalized joint. The shape and dimensions are shown in Fig. 4.13. The H coupler was made of tool steel of ČSN 19 573. This is a high-alloy, heat-resistant and corrosion-resistant steel containing chromium, nickel, and other alloying elements that provide excellent resistance to corrosion and high temperatures. Due to its chemical stability and mechanical strength, it is used not only for components operating in extreme conditions but also in laboratory instruments and precision measuring equipment where dimensional stability, strength, and accuracy are key.

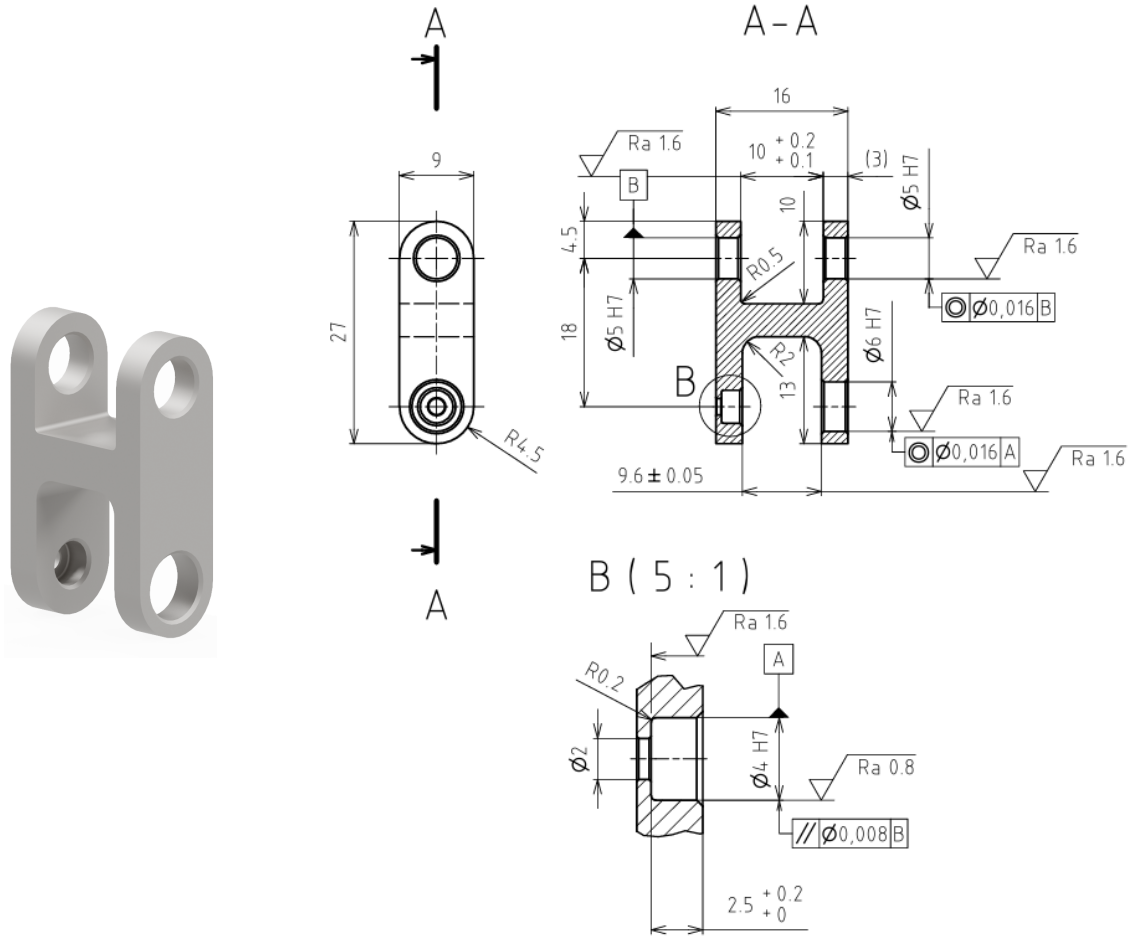

Figure 4.13: H coupler (dimensions in mm)

However, removing the crossbar from the mechanism could lead to the problem outlined in the introduction to this subsection. That is, the torsion stress on the specimen if the clamps were slightly rotated relative to each other during the assembly of the test device. For this reason, a very precise centering part has been designed and manufactured that replaces the clamps during the assembly of the equipment and ensures that the clamps are always precisely positioned relative to each other.

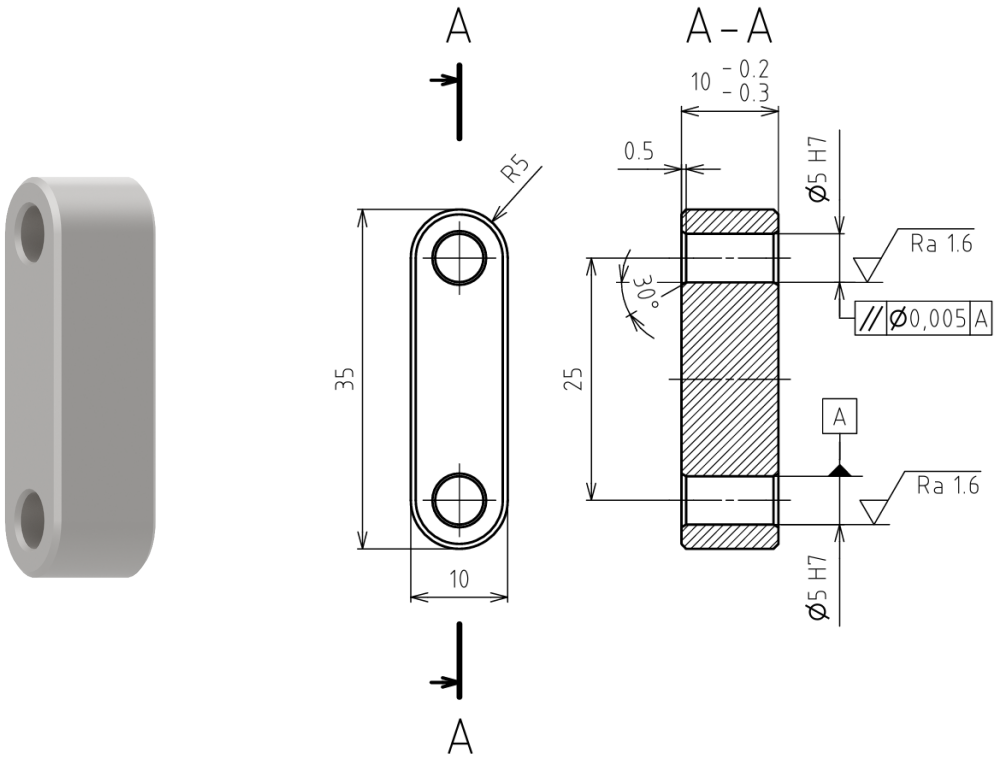

Figure 4.14: Centering fixture

In Fig. 4.14, the centering fixture can be seen which was made the same as the H coupler of steel ČSN 19 573. During assembly, this part is placed using the same pins that are used to secure the clamps. This results in a very precise positioning of the joint at the bottom of the testing device in relation to the upper cross bar, which in turn ensures that the clamps are also precisely positioned in relation to each other. The joint is fixed firmly in the load cell by means of a nut and cannot be rotated during clamping and measurement.

This change has ensured that the reaction force is minimally affected by frictional or other reaction forces and the entire magnitude is transmitted directly to the load cell. Moreover, clamping of the specimen can be much easier and new fixtures can be designed for clamping.

4.3.2 Assembly of the joint and its function

The above mentioned and designed parts were then used to assemble the whole joint, which will replace the lower cross bar. The joint thus consists of a bolt, a gimbal, and an H coupler. The aforementioned centering fixture is then used to properly attach it to the test device.

The gimbal had to be modified by removing one of its parts. This was made possible because these parts always have, for reasons of design and strength, one of the pins around which the whole gimbal rotates through the center of the connecting block. This made it possible, without damaging other parts, to pull that pin out with a press and use the rest of the gimbal, including that pin, to connect it to the H coupler. The bolt was also pressed into the other part of the gimbal and this created the whole joint which can be seen in Fig. 4.15.

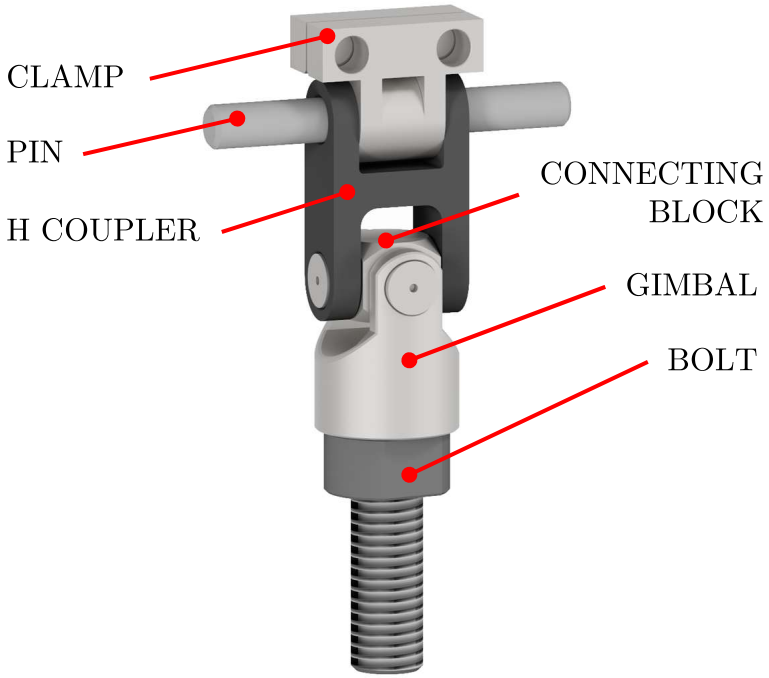

Figure 4.15: Assembled joint

4.4 Fixtures for clamping and other parts

4.4.1 3D printed fixtures

The specimens for mini testing are very small and working with them, especially during clamping before testing, is quite delicate. Moreover, their wrong clamping (for example clamping too far off axis or at an angle) could cause multi-axial loading and the experiment would not be meaningful. Furthermore, clamping could damage the specimen, deforming it and thus invalidating it. That is why special fixtures to help position the specimen correctly during clamping and prevent damage were developed.

The basis of all accessories is a block, which has hexagonal cut-outs in it, into which the nuts of the screws that are used to tighten the clamps fit, and are – as clamps – perfectly located in fixture. This ensures that the clamps are always in equal alignment with the fixture and are centered against each other. In the middle of the fixture, a small cutout of the shape of the specimen is designed in which the specimen fits perfectly. This recess ensures that the specimen is accurately and perpendicularly inserted into the clamp and that the claps can be tightened with a torque wrench. The fixture has holes in the sides that allow it to be screwed to other parts or holders, which makes it easier to tighten the clamp screws and manipulate the specimen. In the center of the hexagonal holes for the nuts, there is a hole which allows the nuts or jaws to be pushed out of the fixture if necessary, or an Allen key can be pushed through this hole, and the head of a bolt is then placed in the hole instead of the nut. The principle of clamping is then the same, it just depends on the user to choose the method. The designed fixtures are on Fig. 4.16.

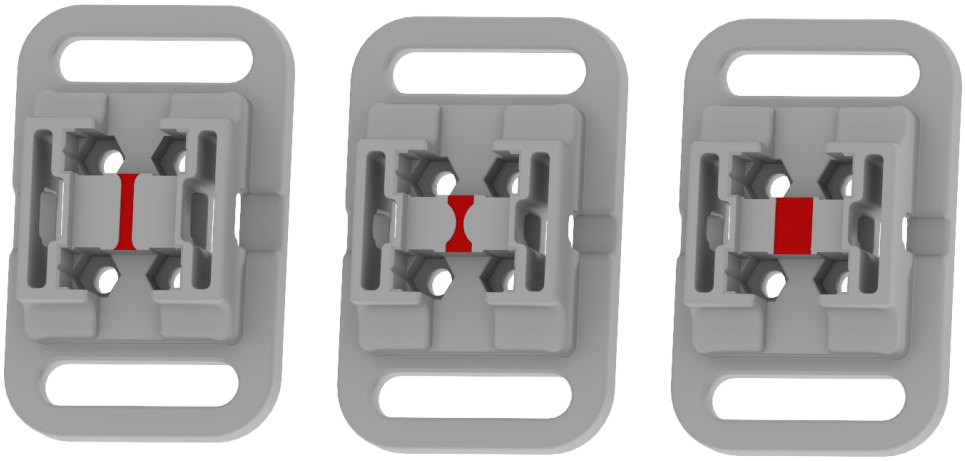

Figure 4.16: Fixtures for clamping

The Stereolithography (SLA) 3D printing method was used for production. The SLA is a 3D printing method in which a laser or ultraviolet light gradually cures a liquid photopolymer resin layer by layer to create detailed and precise objects. This technology is characterized by high precision and smooth surface of the resulting parts. Using SLA, these fixtures could be manufactured with great precision, and even an embedment detail of 0.1 to 0.2 mm would be accurate enough to ensure proper specimen clamping. Specifically, the printer used, branded Elegoo Saturn 3 Ultra with Masked Stereolithography (MSLA) printing technology, is aimed at high-precision printing with detailed smooth surfaces and sharp corners and edges. The display resolution of this printer is 12k, exact specifications can be obtained from the manufacturer's website [71].

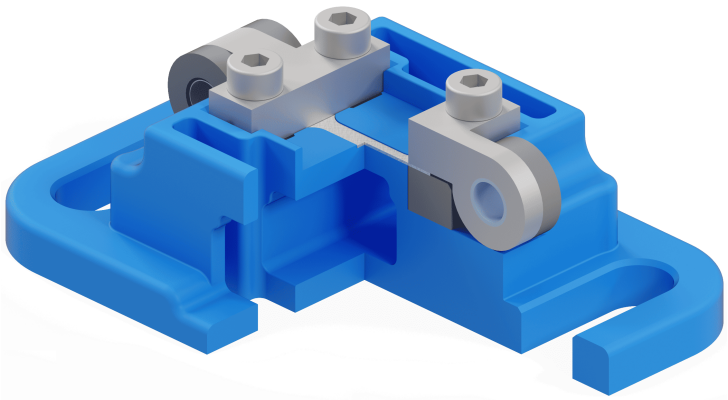

Figure 4.17: Fixtures with claps and specimen in a virtual cut

4.4.2 Clamps housing

Although the new clamping method improves specimen manipulation and significantly increases clamping accuracy, it also poses some problems. The holes in the clamps and in the parts, where the clamps are connected, are facing holes with geometric tolerance H7. Unfortunately, when tightening the clamps in which the specimen is placed, the holes are slightly misaligned and the face pin can no longer be inserted through both holes of the clamps after tightening. In addition, it may occur that after tightening, the jaws remain open, as shown in the middle of the Fig. 4.10. For this reason, a housing has been designed which can be inserted into the clamps when they are in the fixture and

then tightened. This ensures that the clamps grip the specimen perfectly and that the pin can be pushed through the housing very comfortably when the clamps are placed in the instrument. The housing was made from ČSN 19 573 steel as above parts, and its geometry can be seen in Fig. 4.18.

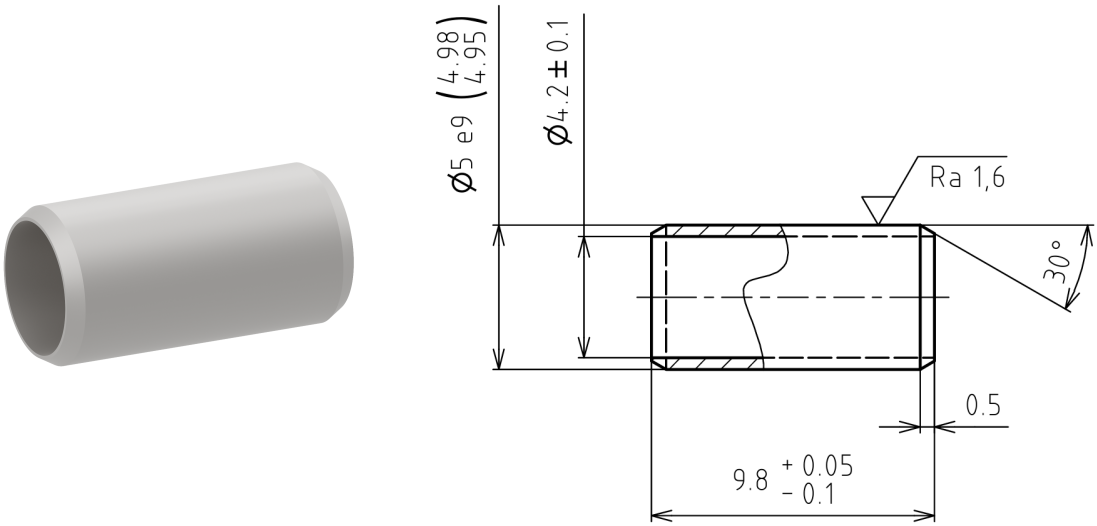

Figure 4.18: Clamps housing (dimensions in mm)

4.4.3 Motor movement screw head

The last modification was the replacement of the motion screw head, which converts the rotational motion of the motor to the translational motion of the upper cross member.

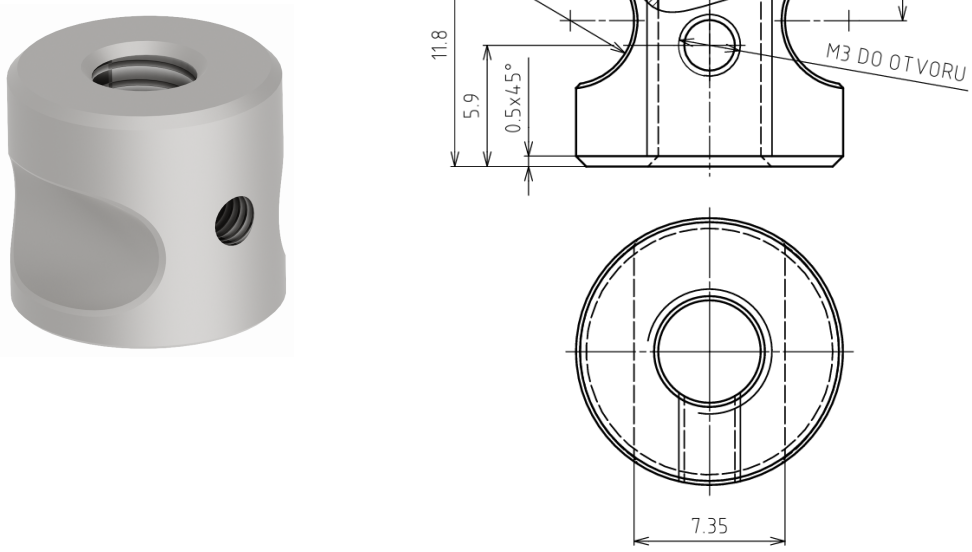

Figure 4.19: Design of a screw head (dimensions in mm)

Due to the fact that the original head was rotationally symmetrical, there was accidental slippage of the head in the cross member, and the screw was drifting with the nut in the motor. To prevent this, a different head was designed and manufactured which prevents the rotation of the screw by means of a form contact, so that the translational movement of the cross member is always present. The proposed shape and its dimensions are shown in Fig. 4.19. The material used for the manufacturing was steel 1.4305 according to DIN EN ISO 4957.

4.5 Final assembly

Thanks to all the above mentioned modifications, which were made based on the gained experience and the one from previous testing, a complete test apparatus was assembled, which is shown in Fig. 4.20.

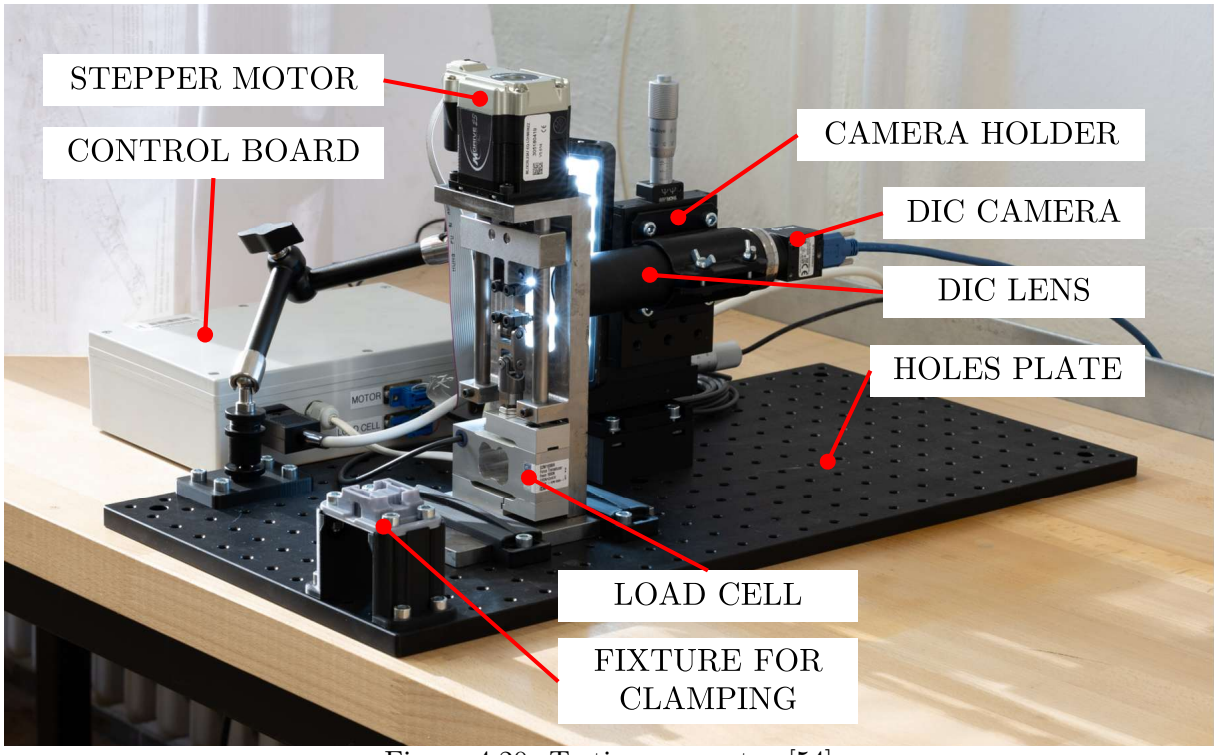

Figure 4.20: Testing apparatus [54]

The new modified assembly consists of a base in the form of a perforated steel plate with threads to which the individual parts of the test apparatus can be firmly attached due to modified parts and manufactured mounts. The main part is a mini-testing device supplemented with all the above described modifications and new components. A new lens holder is placed behind the mini-testing device. As can be seen in Fig. 4.20, it is a different holder than the one designed in this chapter. This is because, after changing the lens of the DIC camera, the designed holder was not rigid enough due to the significant increase in the weight of the lens. Thus, it was possible to use industrially produced travel translation stages. The final holder used is called the XYZ Translation Stage with Standard Micrometers, the specific type that was used is marked as PT3/M and is shown in Fig. 4.21. This XYZ Translation Stage has high accuracy and is orders of magnitude stiffer than the proposed 3D printer design.

Figure 4.21: XYZ Translation Stage PT3/M [72]

Thorlabs PT series translation stages offer a travel range of 1.00” (25.4 mm) and utilize hardened steel linear bearings for precise motion and durability. They are available with various actuators, including adjuster screws, standard manual micrometers, or differential adjusters. The modular design allows for easy configuration into XY or XYZ orientations, with an XY stacked orthogonality of less than 5 mrad and an angular deviation under 250 µrad. Each stage features sixteen 1/4”–20 (M6) tapped mounting holes, facilitating versatile integration into optical setups [72].

Other parts include a Fomei LED MINI RGB 12 light that illuminates the specimen for measurement through the DIC, a control board [63, 64] containing the control electronics wiring to control the motor and read data from the load cell, and a fixture on the board for clamping the specimen so that it is accessible and easy to work with when clamping the specimen.

5 Plan of experiments

As mentioned above, the main and only experimental tool of this thesis is the uniaxial tensile test. This tensile test is the most widely used method of testing material properties and therefore a good choice for determining properties to calibrate material models. The basic tensile test takes several different forms and must be performed under certain conditions to determine the effect of specimen size, strain rate, and temperature.

5.1 Tensile test

In the Czech Republic, the tensile test of metallic materials is currently defined by the standard ČSN EN ISO 6892-1 entitled "Kovové materiály – Zkoušení tahem – Část 1: Zkušební metoda za pokojové teploty" [40]. This standard specifies the procedures for performing tensile tests at room temperature and specifies the mechanical properties that can be determined by this test, such as tensile strength, yield strength, and elongation. It is a part of the international series of ISO 6892 standards, which also covers tensile testing under different temperature conditions, EN ISO 6892-2 [41]. The standard defines several types of test bodies. The most commonly used are the cylindrical or dog-bone specimen, see Fig. 5.1.

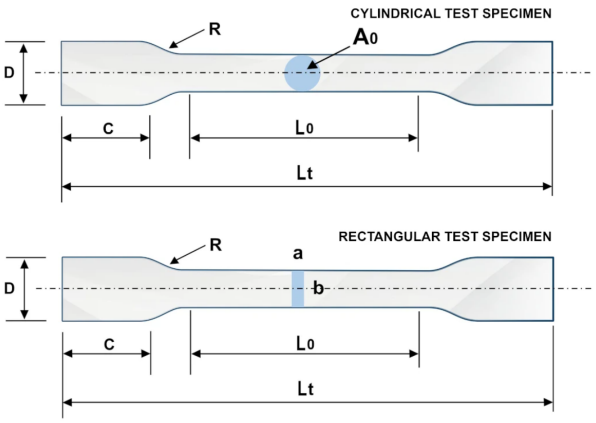

Figure 5.1: Types of used specimens [73]

The norm specifies the dimensions of the test part of the cylindrical specimen. The recommended dimensions are $d_0 = 2.5; 6.25; 12\,[\text{mm}]$ and $L_0 = 10; 25; 50\,[\text{mm}]$. Alternatively, other dimensions can be used, provided that the prescribed standard ratio $d_0/L_0 = 5$, or an alternative ratio used for specific materials or applications, is maintained $d_0/L_0 = 10$ [40].

For the classical tests of all materials tested in this thesis, i.e. AW 2024–T351, additively manufactured Inconel 718 and 316L stainless steel, a cylindrical specimen with base dimensions $d_0 = 6$ mm and $L_0 = 30$ mm was used. The geometry of this specimen is shown in Fig. 5.2. The only exception is the quasi-static test of 316L material, which was performed with a specimen with basic dimensions $d_0 = 8$ mm and $L_0 = 40$ mm whose

geometry can be seen in Fig. 5.3 while other experiments on that steel were performed using specimens in Fig. 5.2.

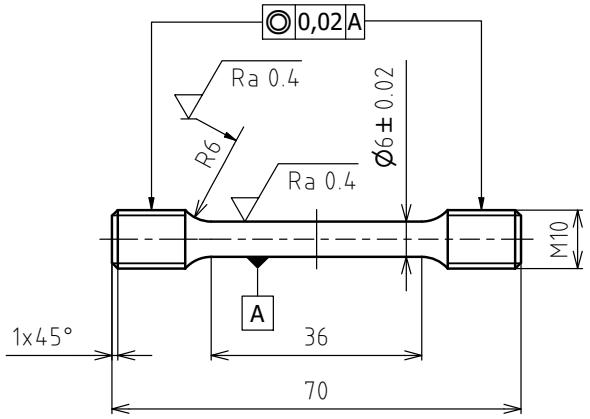

Figure 5.2: Standard specimen with 6 mm diameter

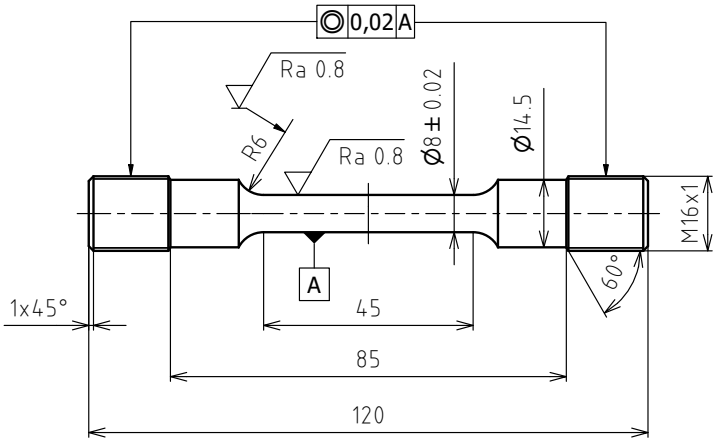

Figure 5.3: Standard specimen with 8 mm diameter

Table 5.1: Parameters for quasi-static, dynamic and high-temperature tensile tests

Tensile test	**Material**	**Temperature** [°C]	**Loading rate** [mm/min]
quasi-static	SS 316L Inconel 718 AW 2024–T351	$T_r = 22$	1
dynamic	SS 316L Inconel 718 AW 2024–T351 AW 2024–T351	$T_r = 22$	100 200
high-temperature	SS 316L AW 2024–T351 AW 2024–T351	+400 +150 +200	1

The classical course of the tensile test does not need further introduction. What is essential is just the setup of the simulations. For the quasi-static, dynamic and thermal tests, this is mainly about the loading rate and the ambient temperature. All tests on classical specimens were performed on the *Zwick/Roell Z250, load cell of: 150 kN, Zwick multiXtens extensometer for static, quasi-static, and dynamic and MAYTEC PMA-12/V7-1 for elevated temperatures with MAYTEC HTO-08/1 furnace.* in the laboratory of the Institute of Materials Science and Engineering. A detailed overview of the set of parameters is listed in the table 5.1.

5.2 Static testing

In tensile tests, the method of temporary stopping of loading (the so-called stress relaxation) was used to obtain static stress–strain curves, based on Huang & Young [74]. In a series of coupon tests on various metallic materials (G450 ductile carbon steel, lean duplex and ferritic stainless steels, aluminum alloy T6), the authors demonstrated that holding the deformation constant for ten to hundreds of seconds results in a stress drop due to relaxation, which leads to the elimination of dynamic effects and allows the determination of more accurate "static" material characteristics [74].

The basic principle of this method is to suspend the load during the tensile test at predetermined points. The authors recommend stopping near the first plastic deformation, i.e, near the yield strength, then at 0.2 % of the strain or at other points where a significant influence of dynamic effects is expected, for example near the ultimate tensile strength. The supply of further deformation should stop at these points. Consequently, the stress (force) is reduced due to the relaxation effect, which reflects the behaviour of the material without the influence of the loading rate. The resulting stress after steady state can thus be considered as static [74].

In the study, the authors found that stress relaxation was more pronounced in areas with higher previous loading rates. The stress drop before the ultimate tensile strength reached values of up to 5–10 % depending on the material and the loading rate. In the experiments in the mentioned study, stopping and stress relaxation were performed for 60, 100 and 300 s to determine the significance of the time at which the specimen can relax. It was found that holding the strain for more than 100 s already results in only minimal additional stress drops (typically < 1 %), making this time the optimal time in terms of test efficiency [74]. For this reason, 100 s was the pause time chosen for the experiments in this thesis.

Advantages of the method are:

- It eliminates the effect of the load speed on the result (the *ASTM*, *BSI* and *AS* standards allow relatively wide speed ranges, but they affect $R_{p0.2}$ and σ_u by up to 10–13 %).
- It provides consistent and comparable results between specimens and materials.
- It allows more accurate calibration of material models for numerical simulations (e.g. Johnson–Cook, Ramberg–Osgood, elasto–plastic models).

Based on the results from the quasi-static and static tests of AW3034 T351, Inconel 718 and 316L stainless steel could be designed, each time at the yield point (first appearance of plastic deformation), then at the 0.2 % strain point and at the expected ultimate tensile strength. The complete inventory according to which the materials were tested is given in the table 5.2. The elongation values in the table are valid for a specimen length equal

to 30 mm.

Table 5.2: Parameters for static tensile tests

Material	**Strain** ε [–]	**Elongation** Δl [mm]	**Loading rate** [mm/min]
SS 316L-L	0–0.006	0–0.18	1
	0.006	0.18	pause 100 s
	0.006–0.2	0.18–6	1
	0.2	6	pause 100 s
	0.2–0.4	6–12	1
	0.4	12	pause 100 s
	0.4–fracture	12–fracture	1
Inconel 718	0–0.006	0–0.18	1
	0.006	0.18	pause 100 s
	0.006–0.2	0.18–6	1
	0.2	6	pause 100 s
	0.2–0.4	6–10.5	1
	0.35	10.5	pause 100 s
	0.35–fracture	10.5–fracture	1
AW2024 T351	0–0.006	0–0.18	1
	0.006	0.18	pause 100 s
	0.006–0.06	0.18–1.8	1
	0.06	1.8	pause 100 s
	0.06–0.12	1.8–3.6	1
	0.12	3.6	pause 100 s
	0.12–fracture	3.6–fracture	1

In order to make it clear at which points during the tensile test the loading should be suspended, x coordinates of the engineering strain values were plotted in the classical quasi-static test. The graphs with the plotted waveforms and values are shown in Fig. 5.4.

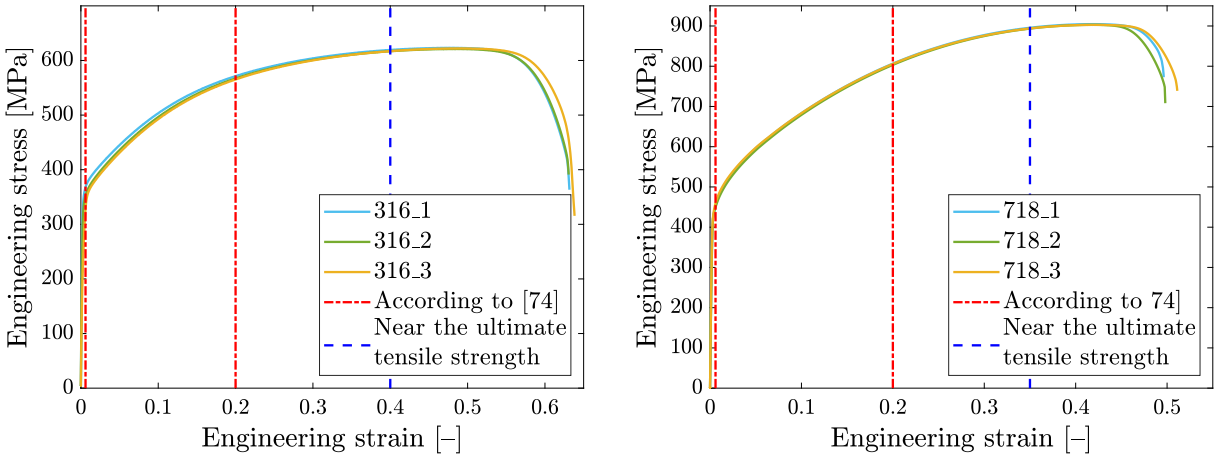

a) Stainless steel 316L *b) Inconel 718*

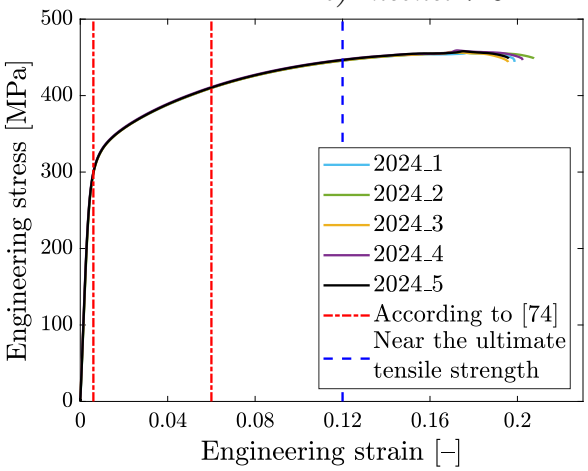

c) AW 2024–T351

Figure 5.4: Representation of load stop

An important part of the subsequent processing of the measured data is the way in which the static curve will be determined. A complete description of how to obtain the static curve and how to represent it is contained in Fig. 4.5 [74].

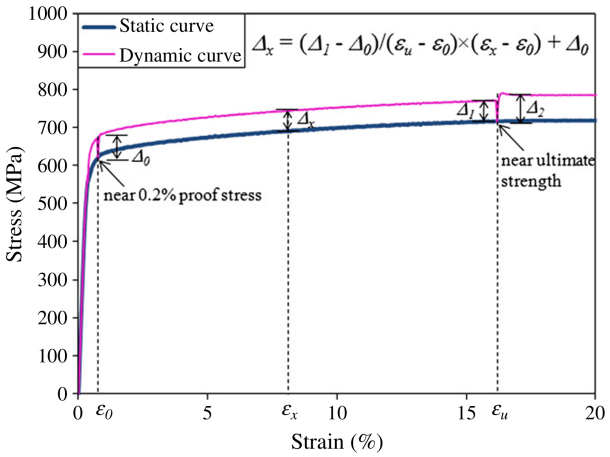

Figure 5.5: Representation of the static curve calculation [74]

In this thesis, in contrast to the previously mentioned article, a total of three stops for 100 s were proposed for each material. However, the method of calculating the static curve remains the same. The strain diagram is divided into four regions. The first region contains the elastic part and the first plastic deformations. The second and third areas contain the progression of plasticity, and the last area is the end of the curve, up to the fracture of the material. To calculate the curve, a linear stress versus strain curve is modelled between two points, using the stress values obtained during static drops (relaxation) at these points. The paper directly presents the formula used to determine the static curve as

$$\Delta_x = \frac{(\Delta_1 - \Delta_0)}{(\varepsilon_u - \varepsilon_0)}(\varepsilon_x - \varepsilon_0) + \Delta_0 \tag{5.1}$$

where Δ_0 is the difference between the value of the curve and the static drop after first relaxation according to the calculated area, Δ_1 is the difference between the value of the curve and the static drop before second relaxation according to the calculated area, ε_0 is the strain value during the first relaxation, ε_u is the strain value during the second relaxation and ε_x is the strain value in which the Δ_x – approximated drop, is calculated.

As can be seen in Fig. 5.5 and from Equation (5.1), it is important to check the magnitude of the static drop before and after the stop, because these values are different and both are important for the calculation of the single-motion areas. The value denoted as $\Delta_0 = 0$ can be used for the first part. The fourth part is calculated by subtracting the constant difference of Δ_2 from the value of the curve. Here, Δ_2 represents the difference between the value of the final static drop and the curve after the final relaxation. This can be seen in Fig. 5.5 [74].

5.3 Miniature testing

When miniaturized specimens are experimentally tested, it is necessary to select the correct loading rate. Thus, a value of 0.05 mm/min is suggested for all tests. This value corresponds to a low strain rate on the order of $10^{-4}\,\mathrm{s}^{-1}$ depending on the length of the measured part of the specimen. The choice of this low rate was guided by the desire to provide quasi-static loading conditions that eliminate the influence of viscoplastic effects. This is particularly important for very small specimens with short measurement lengths (typically $2-6\,\mathrm{mm}$) where higher velocities could lead to inaccuracies in the measurement or deformation that does not match the model assumptions. At the same time, this rate causes the deformation rate in the mini-test to be the same as the deformation rate in the conventional quasi-static test, and therefore the results of these tests can be compared with each other. Moreover, this rate has already been used in previous works [31, 64]. Geometry of all the miniature samples used in this thesis are shown in Fig. 5.6.

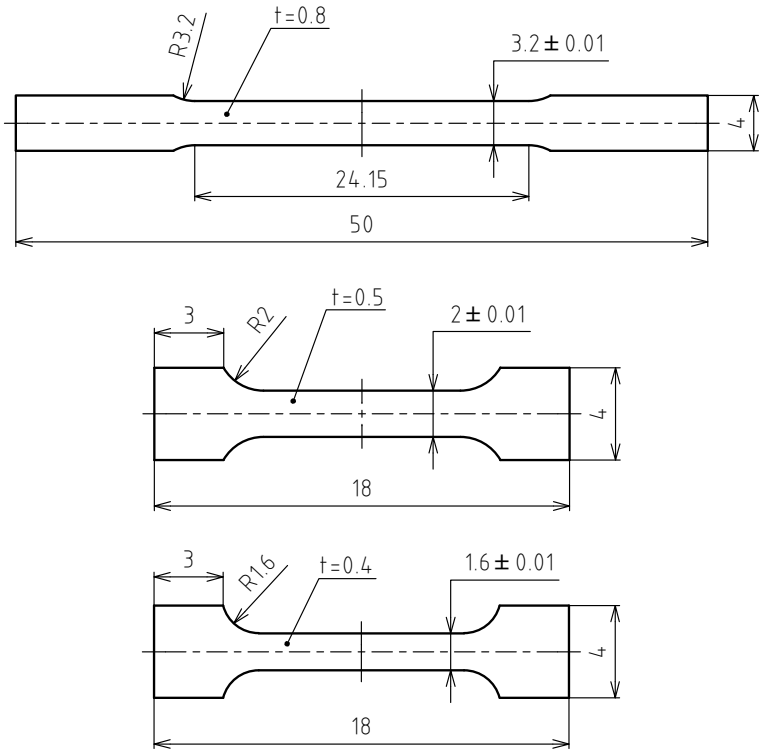

Figure 5.6: Geometry of miniature specimens

6 Experimental procedures

The standard tensile test procedure is generally known, but what is new due to the modifications of the mini-testing equipment is the procedure for testing mini specimens in the laboratory. Thus, for transparency and for further possible work, it is necessary to define the whole procedure of testing mini specimens well to make the test results relevant.

6.1 Miniature testing procedure

The test procedure proposed here is based on experience and is modified according to the new capabilities of the mini-tester. The entire test apparatus shown in Fig. 4.20 must only be assembled by a qualified laboratory technician to avoid damage to the equipment and to ensure the correct position of the individual components in relation to each other. If incorrectly assembled, large deviations in strain measurements by DIC or multi-axial loading of the specimen could occur, and the experimental results would not be valid.

6.1.1 Preparation of mini specimens

The specimens must be properly prepared before the experiment begins. This includes cleaning, measuring, and spraying them with a special pattern for DIC measurements. The exact specimen preparation procedure is listed in the following list:

1. Cleaning the specimens from possible impurities and oils that may have gotten on the specimen due to the production procedure. For degreasing of the metallic specimens prior to testing, technical–grade acetone with a minimum purity of 99 % was used. It is recommended to use cotton sticks or paper towels for cleaning and to take extra care of mechanical damage to the specimen.
2. Marking the specimen with an identification code at the clamping points and entering this code into the system so that it can be correctly identified throughout and after the experiment.
3. Measuring the basic dimensions of the specimen using a calibrated micrometer caliper and entering their values into the system.
4. Preparation of the specimens for pattern spraying for DIC measurements. The specimens are placed in series, usually 10 in a holder, so that their identification code is not covered.
5. The pattern spraying was carried out in several steps. First, a layer of white primer (Primalex Antikorozní základní barva ve spreji, white, 400 ml) was applied. After drying, the surface was optionally smoothed with fine sandpaper depending on its texture, in order to ensure a fully homogeneous white background. Subsequently, a black speckle pattern was created by spraying a matte black paint (Barva ve spreji MASTON Color, black matte, 400 ml), targeting approximately 50 % surface coverage. The spraying process was performed on both sides of the specimen and carried out exclusively by trained personnel to ensure reproducibility and safety.

6. After the pattern has dried, the specimens are removed from the holder. In case the spray layer has settled on the thin sides of the specimen (by thickness), the operator mechanically removes this paint so as not to damage the pattern on the measured surfaces of the specimen. Too much paint on the edges of the specimen could cause the specimen to be inserted into the clamping fixture (Fig. 4.16) incorrectly, causing it to clamp incorrectly and invalidate the experiment.

6.1.2 Experiment preparation and specimen clamping

Before starting the measurements, it is necessary to go through the procedure of preparation and verification of the experimental apparatus. This procedure includes the preparation of the software and the measuring equipment and the check that they are working correctly. At the same time, proper handling and insertion of the specimen clamp into the instrument is also necessary.

1. The first step is to turn on the computer. A drive unit is connected to the computer to control the stepper motor and record the load cell data. Then the DIC camera is connected to the computer. (It is advisable to leave the DIC camera plugged in before testing for a period of 30 to 60 minutes to calibrate it to the correct operating temperature.)
2. The Alpha 2023.1.21 from X-Sight program is run on the computer to control and record data from the DIC camera. If the whole apparatus has been assembled, it is necessary to calibrate and set up the DIC camera correctly at this stage. Then the miniature testing software is started. This is run to control the stepper motor and the load cell. The software must be run in this order to ensure that the control and data flow connections are loaded correctly.

   Steps for setting up the DIC camera and Alpha software during the assembly of the testing apparatus:

   (a) During the assembly of the miniature testing apparatus, the camera must first be aligned with the test region. For this purpose, a calibration slide with a micrometer scale (stage micrometer) is mounted in the specimen clamps. This allows both the mechanical centering of the optical system and the calibration of the pixel-to-distance conversion ratio.

   (b) The pixel-to-distance ratio is essential for converting DIC output from the image domain to real world physical units. Without this calibration, it would not be possible to determine absolute displacements or compute the true strain of the specimen. This value has to be inserted inside the Alpha software during the setup.

   (c) As the measurement system is controlled via a miniature testing software integrated with the Alpha software, the image acquisition in Alpha is automatically triggered upon starting the measurement. To ensure proper temporal synchronization between the experimental data and the image sequence, it is essential to verify and match the frame rate settings in both the miniature testing software and Alpha. Any discrepancy in frame rate may result in incorrect time correlation of the deformation and force data from load cell.

   (d) When defining the probe in the Alpha software – which acts as a virtual extensometer – it is necessary to correctly set the size of the correlation windows

that track the surface pattern. The window size must be an odd number of pixels in order to ensure a well–defined center point. A value of 101 pixels was used most frequently in our testing device, as it provided a good balance between resolution and stability for the given pattern scale.

The probe length, i.e, the distance between the two tracking points used for strain calculation, was usually set to 4 mm or 6 mm, depending on the type of specimen and the expected deformation range. This length defines the physical region over which the strain was computed.

(e) After the probe has been defined, it is also necessary to configure the output values in Alpha. The program allows for up to nine output channels, all of which must be populated to ensure proper export and data structure. Commonly selected outputs include the time axis (based on sampling rate), total elongation, engineering strain, and optionally longitudinal strain, depending on the type of test.

In addition, it is essential to define the target folder for saving image frames captured during the measurement. These frames are used as the basis for deformation analysis. All data, including image sequences and output files, are organized in folder according to the specified specimen ID, which acts as the key reference for file naming, folder structure, and subsequent data processing.

3. Test of basic functions. The operator will test the motor movements, the load cell response and the DIC camera settings to make sure they are working properly and will check for correct data recording as well as DIC camera and load cell in Alpha.
4. In the miniature testing software, it is necessary to set the sampling rate value (same as was defined in Alpha) and zero the force value recorded on the load cell. After that, set a new measurement.
5. Assuming that all tests have gone well and the measurement is set, the operator proceeds to clamp the specimen.

   The specimen fixture was described in chapter 4.4.1 and is firmly attached to the bottom hole plate on two 3D printed legs in the test apparatus. This fixture is also noticeably visible on the Fig. 4.20 in front of the whole setup. The attachment to the plate makes clamping manipulation easier and achieves better results. The space under the fixture is used to insert an Allen (Hex) key when tightening the screws in the fixture. During clamping, it is necessary to follow a predefined procedure and use specialised tools as:

   - Allen key
   - Torque wrench 1–6 Nm – in the laboratory was used EXTOL brand torque wrench with marking *Torque wrench, 1/4" EXTOL PREMIUM 8825304*.

     The wrench has a tightening torque range of 1–6 Nm. The manufacturer supplies a test certificate for this wrench, which guarantees the accuracy of the tightening torque. This particular wrench has been certified with a torque tightening accuracy of ±0.50 %. The manufacturer also guarantees this accuracy for 12 months or 5000 uses.

   Here is the process of specimen clamping described step by step:

   (a) Insert screws or nuts into the holes in the fixture (depending on the clamping style).

(b) Insert half of the clamp into the clamping fixture.

(c) Place the specimen to be clamped in the fixture and align its position with the cutout in the fixture.

(d) Place the other half of the clamp in the fixture to fix the specimen.

(e) Depending on the procedure in (a), secure the clamps with nuts or bolts – do not tighten them.

(f) Insert the clamps housing into the hole in the clamps where the pin goes through to center them.

(g) Tighten the bolts with an Allen and torque wrench using the force 4 Nm.

(h) Remove the specimen clamps from the fixture.

(i) Insert the clamps into the testing device and use the 4 mm diameter pin to fix the clamps in the upper crossbar of the mini tester.

(j) Using another pin, attach the bottom clamp into the joint specifically into H coupler.

(k) Using preload function in miniature testing software to apply preload force of 1–10 N (dependent on the specimen type) to ensure clamps with specimen in testing machine. After preload, set the parameters for testing (loading speed to 0.05 mm/min and force limit).

(l) Check for correct mounting, specimen centering and clamping rigidity.

(m) Turning on the LED lights to illuminate the specimen and focus the DIC camera by moving the camera holder (alternatively adjusting the contrast of the camera).

By following this manual, the specimen and testing apparatus are ready for experiment.

6.1.3 The progress of the experiment

The experiment starts with pushing the corresponding button in miniature testing software. If the software has been synchronized correctly, the measurement will start. The motor will start stretching the specimen with a constant velocity value, the force readings from the load cell will be recorded, and the measurements from the DIC camera will be recorded in the Alpha program window. This measurement can be monitored throughout the experiment. The operator monitors the recorded force and elongation during the experiment to see if there is any error in the measurement. When the specimen breaks, the operator stops the measurement and saves the results in a folder. The file has a name that corresponds to the specimen identification number and a note “succeed”, “warning” or “fail”. The data measured by this procedure are then taken over for subsequent processing.

6.2 Mini testing in COMTES FHT

Since a number of modifications have been made to the mini-testing equipment and a different clamping and specimen work procedure has been designed, it is necessary to independently verify that the modifications have not resulted in errors that would affect the measurements or produce incorrect results. Therefore, some of the miniaturized specimens were tested in a different laboratory – specifically COMTES FHT a.s. A total of

15 tensile specimens were measured there. These were dog bone specimens with the identification tensile_16, tensile_20 and tensile_32. Fig. 5.6 shows the geometry of specimens marked as tensile_16 (width 1.6 mm), tensile_20 (width 2 mm) and tensile_32 (width 3.2 mm). Five specimens of each type were measured. The test boundary conditions were adapted to the proposed parameters in this thesis.

The measurement of specimens in another independent laboratory offers a number of advantages. First, it serves as a form of verification of the results (validation), increasing their reliability and credibility. It also allows the detection of possible systematic errors in methodology, measuring instruments, or procedure. The results validated by an external body are more revealing. They also provide the opportunity for comparison with other laboratories, which can serve as a valuable benchmark to improve the quality of internal processes.

6.3 Summary of measurements made

For clarity, it is useful to list the experimental data obtained and can thus be used for the subsequent calibration of the material model for the materials under investigation. All tests from which data were used are listed in the table 6.1.

Table 6.1: All experiments performed

Tensile test	**Material**	**temp.** [°C]	**strain rate** [s^{-1}]	**specimens**
quasi-static	SS 316L	$T_r = 22$	$\dot{\bar{\varepsilon}}_r = 0,0006$	3
	Inconel 718			3
	AW 2024–T351			5
static	SS 316L	$T_r = 22$	$\dot{\bar{\varepsilon}}_r \to 0$	2
	Inconel 718			2
	AW 2024–T351			2
dynamic	SS 316L	$T_r = 22$	$\dot{\bar{\varepsilon}}_r = 0,0556$	2
	Inconel 718			1
	AW 2024–T351			2
	AW 2024–T351		$\dot{\bar{\varepsilon}}_r = 0,1111$	1
high-temperature	SS 316L	+400	$\dot{\bar{\varepsilon}}_r = 0,0006$	1
	AW 2024–T351	+150		
	AW 2024–T351	+200		
mini tensile_16 **mini tensile_20** **mini tensile_32**	AW 2024–T351	$T_r = 24$	$\dot{\bar{\varepsilon}}_r \approx 0,0002$	5

7 Data processing

Correct processing of the measured data is just as important as measurement. MATLAB R2024b software was used under student license for complete processing. To process the tensile test data, which are all in force–elongation format, it is necessary to provide some basic relations for conversion to engineering stress–strain and then to true stress–strain and further processing.

7.1 Computational relations

The engineering and true tensile diagram are described by a number of equations and quantities that specify the stress history, include a number of different influences, and can describe the behaviour of the material. However, here is a listing of the equations and quantities that are necessary for subsequent processing of the experimental data.

Deformation and stress quantities

The basic deformation quantities include the strain, which indicates the relative deformation of the body. It is determined by calculating from the original length of the body L_0 and its deformed length L, see equation (7.1). This equation describes the engineering strain. The quantity is generally dimensionless, but can also be expressed as a percentage [18, 75].

$$\varepsilon_{eng} = \frac{L - L_0}{L_0} = \frac{\Delta L}{L_0} \quad [–] \tag{7.1}$$

Stress is the force applied per area. Equation (7.2) indicates the engineering stress, which is expressed as a fraction of the applied force F relative to the original area of the specimen S_0 [18].

$$\sigma_{eng} = \frac{F}{S_0} \quad [\text{MPa}] \tag{7.2}$$

True (logarithmic) strain and stress can be defined in a similar way. These stresses are needed to describe the behaviour of ductile materials that undergo significant plastic deformation. The true strain can be defined in terms of the length increase dL integration from the initial state L_0 to the final state L [75]. The resulting relationship after integration is shown in the equation (7.3).

$$\varepsilon = \ln\frac{L}{L_0} \quad [–] \tag{7.3}$$

The true stress is then the ratio of the applied force and the actual (deformed) area,

see Equation (7.4).

$$\sigma = \frac{F}{S} \text{ [MPa]} \tag{7.4}$$

However, for the purposes of this thesis, the conversion relationships between the engineering and the true tension diagrams are more relevant. These relationships are only valid up to the onset of the neck, i.e. ultimate tensile strength, but for the calibration of the material model, this progression is completely sufficient. The conversion relationship between engineering and the true strain is described by Equation (7.5) [75].

$$\varepsilon_{true} = \ln(1 + \varepsilon_{eng}) \text{ [–]} \tag{7.5}$$

For the determination of the parameters of the material model and for the subsequent numerical simulation, it is crucial to remember that beyond the yield strength, the deformation consists of both elastic and plastic components.

$$\varepsilon_{tot} = \varepsilon_{el} + \varepsilon_{pl} \tag{7.6}$$

In the same way that the relationship for the conversion of engineering and true strain to ultimate strength has been given, the relationship for the conversion between true and engineering stress must be given [75]:

$$\sigma_{true} = \sigma_{eng}(1 + \varepsilon_{eng}) \tag{7.7}$$

Other mathematical relations

To process the data, it is also necessary to specify the relationships to calculate the mean, standard deviations, and errors. Most of the tests were performed repeatedly to eliminate measurement errors and increase the reliability of the results.

The average of the measured values can be calculated using Equation (7.8) [76]

$$\bar{x} = \frac{1}{N} \sum_{i=1}^{N} x_i \tag{7.8}$$

where x_i are the individual values of the data file and N is the number of values that are not `NaN`.

The standard deviation (s) is a statistical quantity that measures the dispersion or variability of the values of a data set around their mean ($\bar{x}$). It expresses the average distance of individual values from the mean and is often used to describe how the data are "spread out". The standard deviation is calculated using Equation (7.9) [76]:

$$s = \sqrt{\frac{1}{N-1} \sum_{i=1}^{N} (x_i - \bar{x})^2} \tag{7.9}$$

Standard Error of the Mean (SEM) is a statistical quantity that expresses the precision of the estimate of the arithmetic mean ($\bar{x}$) based on the specimen. The SEM measures how much the mean of the specimen may differ from the mean of the true population. The smaller the SEM value, the more accurately the mean of the specimen represents the mean of the population. The mean error is calculated using Equation (7.10) [76]:

$$\mathrm{SEM} = \frac{s}{\sqrt{N}} \tag{7.10}$$

7.2 Material model

Material behaviour is a combination of a number of effects. In this work, where the main objective is to calibrate the material parameters for three investigated materials, only the elasticity and plasticity are modelled.

7.2.1 Model of elasticity

Elastic deformation zone was modelled by Hooke's law. The material was obtained as isotropic but elastic material properties of materials were not experimentally investigated in this work. The material characteristics were taken from the previous work of the supervisor or other publicly available sources and data sheets. Therefore, unless otherwise specified, the source of the values of the given parameters is from the papers of the supervisor.

7.2.2 Model of plasticity

Based on the research study and the possibilities of modelling the behaviour of the material in the available FEM software, Johnson–Cook was chosen as a suitable material model. This material model accurately simulates the classical quasi-static behavior while introducing the effect of both velocity and temperature which is essential for this work.

The Johnson–Cook model is a frequently used constitutive equation that describes the plastic deformation of metallic materials under various conditions of load, strain rate and temperature. It is defined by the following equation [26]:

$$\bar{\sigma} = \left(A + B\bar{\varepsilon}_p^n\right)\left(1 + C\ln\frac{\dot{\bar{\varepsilon}}_p}{\dot{\bar{\varepsilon}}_r}\right)\left(1 - T_h^m\right), \tag{7.11}$$

where [26]:

- $\bar{\sigma}$: Equivalent stress,
- A: Yield stress at reference strain rate and temperature ($T_h = 0$),
- B: Hardening constant describing the stress increase due to plastic deformation,
- $\bar{\varepsilon}_p$: Equivalent plastic strain,
- n: Strain hardening exponen,
- C: Constant strain rate coefficient,
- $\dot{\bar{\varepsilon}}_p$: Equivalent plastic strain rate,
- $\dot{\bar{\varepsilon}}_r$: Reference plastic strain rate,

- $T_h = \frac{T-T_r}{T_m-T_r}$: Homological temperature, where:
  - T: Actual temperature,
  - T_r: Reference temperature (room temperature),
  - T_m: Melting temperature,
- m: Exponent of the temperature effect.

The equation combines the influence of three main components [26, 77]:

1. **Plastic deformation hardening** – The part $(A + B\bar{\varepsilon}_p^n)$ describes the increase in stress due to plastic deformation. The yield stress A indicates the minimum stress required to initiate plastic deformation, while B and n affect how quickly the stress increases with increasing strain.
2. **Influence of strain rate** – The part $\left(1 + C \ln \frac{\dot{\bar{\varepsilon}}_p}{\dot{\varepsilon}_r}\right)$ models the dependence of stress on the rate of plastic deformation. A higher equivalent plastic strain rate $(\dot{\bar{\varepsilon}}_p)$ causes an increase in flow stress, which is explained by the parameter C.
3. **Temperature effect** – The $(1 - T_h^m)$ part includes the effect of temperature, which decreases the flow stress with increasing value. The normalized temperature T_h is 0 at the reference temperature T_r and 1 at the melting temperature T_m. The exponent m determines the sensitivity of the material to change in temperature.

As already mentioned, this model combines the effects of plastic deformation, strain rate, and temperature to describe material behaviour in a wide range of applications, including impact, ballistics, machining, metal forming, and explosions. Due to its relative simplicity and the ability to include key effects, the model is widely implemented in numerical codes such as the FEM. The main advantage of the Johnson–Cook model is its versatility and simplicity of implementation, which makes it possible to simulate dynamic processes such as high-speed impacts or to predict the behaviour of materials under extreme conditions such as high temperature and strain rate. However, disadvantages of the model include its limited ability to describe anisotropic material behaviour or microstructural changes that may occur during deformation. The Johnson–Cook model still remains one of the most widely used tools in engineering applications due to its balance between simplicity and its ability to describe the behaviour of complex materials [26, 77].

7.3 Preparation of experimental data for curve fitting

7.3.1 Engineering stress–strain diagram

To calibrate the parameters of the Johnson–Cook material model, the true values of stress and plastic strain must be obtained from the measured data. These values can be obtained using the relationships given in chapter 7.1. The first step in the processing is to determine the engineering tensile diagram. To do this, the engineering stress and strain values for all the experiments performed were recalculated from the measured data. For tests in which more than one test was performed, an average (reference) value of engineering stress and strain must be determined, and from that the true stress and true strain will then be calculated to calibrate the material parameters.

Before calculating the average (representative) value of engineering stress and strain, the validity of the measured data was evaluated. As an example of measured data converted to engineering stress and strain values, the tensile curves of the quasi-static test of AW 2024–T351 are plotted in Fig. 7.1.

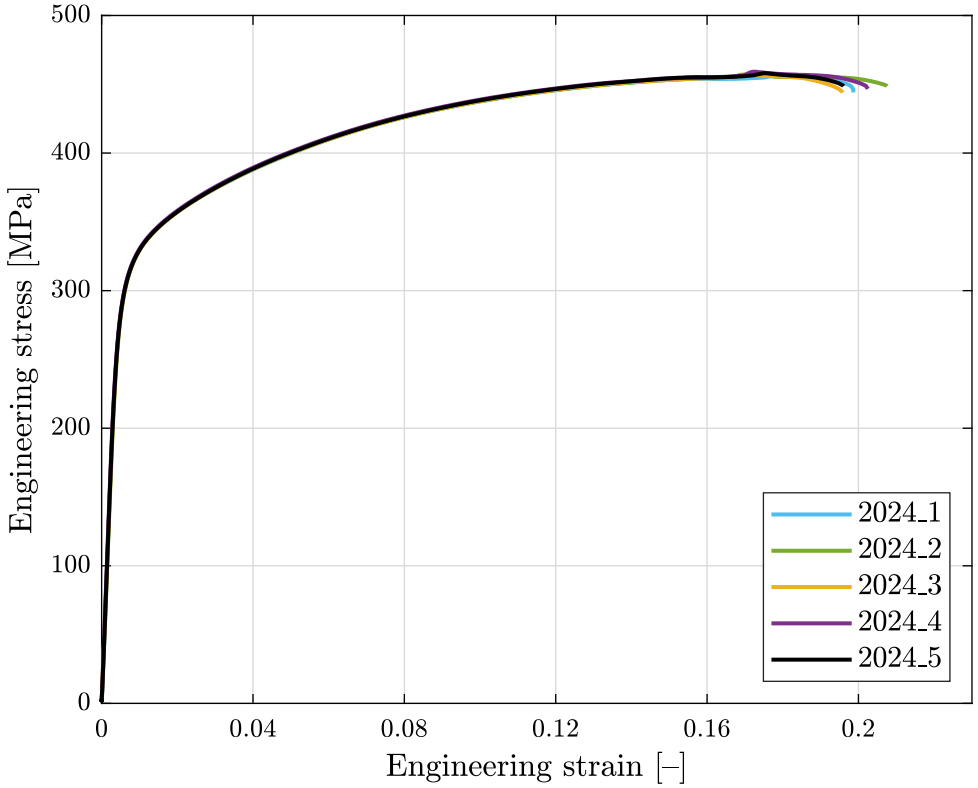

Figure 7.1: Engineering stress strain of quasi-static tests – AW 2024–T351

After obtaining all engineering stress and strain curves, the average value can be calculated. The calculation procedure was described in the chapter 7.1. The average value of the engineering tensile diagram and standard deviation were calculated in the MATLAB software. The resulting tensile diagram consisting of the average value for the experimental data type was plotted, including a representation of the deviation using the error bar function at selected locations on the graph. Since there is a large number of results and graphs and it would not be meaningful to present all results and intermediate calculations in this thesis, the material AW 2024–T351 is chosen here as a representative example, see Fig. 7.2. Most types of test have been performed on this material and so it is appropriate to use that one as a descriptive example. All other charts are inserted as Appendix A Tensile diagrams.

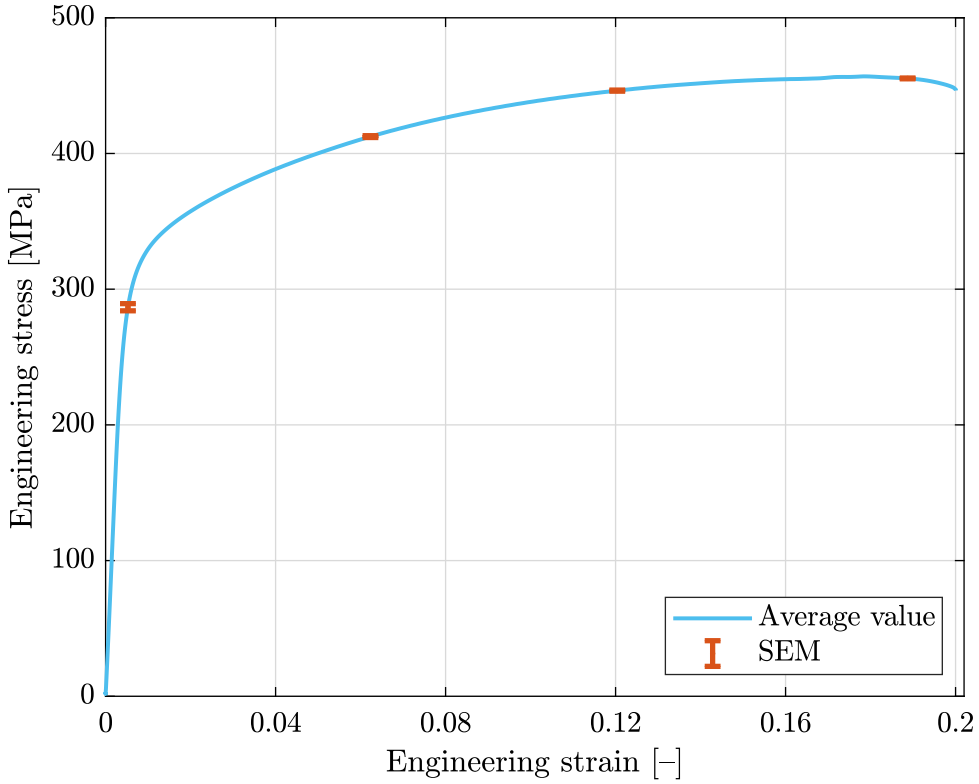

Figure 7.2: Mean value of engineering stress strain diagram – AW 2024–T351

7.3.2 True stress–strain diagram

From the average engineering stress and strain values obtained, it is possible to calculate the true stress and true strain values, but only up to the ultimate tensile strength of the material. Beyond the ultimate tensile strength, where a neck starts to form on the test body, this is no longer uniaxial stress and the conversion relationships do not apply. However, the true stress value up to the ultimate tensile strength is quite sufficient for curve fitting and determining the material parameters. Therefore, the relationships in chapter 7.1 were used to obtain true stress and true strain diagrams for all types of experiments.

In this step, the elastic part of the strain was subtracted from the total value of the strain to obtain the plastic strain that is necessary for curve fitting.

7.3.3 Evaluation of static curve

The procedure for determining the static curve was different from the other tests. The static curve should represent pure material response that is not affected in any way by the loading rate. The strain rate should therefore be limitingly close to zero. However, this cannot be achieved in a conventional test, and so the procedure outlined in [74], which has already been described in more detail in the chapter 5.2, was used. The process of determining a representative tensile curve was a bit longer here.

The static curve for a given experiment was determined directly using equation (5.1). For its use in the MATLAB environment, the sections containing static drop values were first selected. In these intervals, thanks to MATLAB functions `min`, `max` and others, the strain values of the static drops and the stress values before and after these drops were obtained. From these values, the values of "drops", marked as Δ, were calculated.

Subsequently, these drop values were used to obtain the static tensile curve. Only after obtaining the individual static curves were these curves averaged as in the other cases, and this average value was used as a reference for calibrating the material parameters after the modifications described above. A graph showing the engineering stress and strain values determined from the experiment, the calculated engineering stress and strain, and their average for AW 2024–T351 are shown in Fig. 7.3.

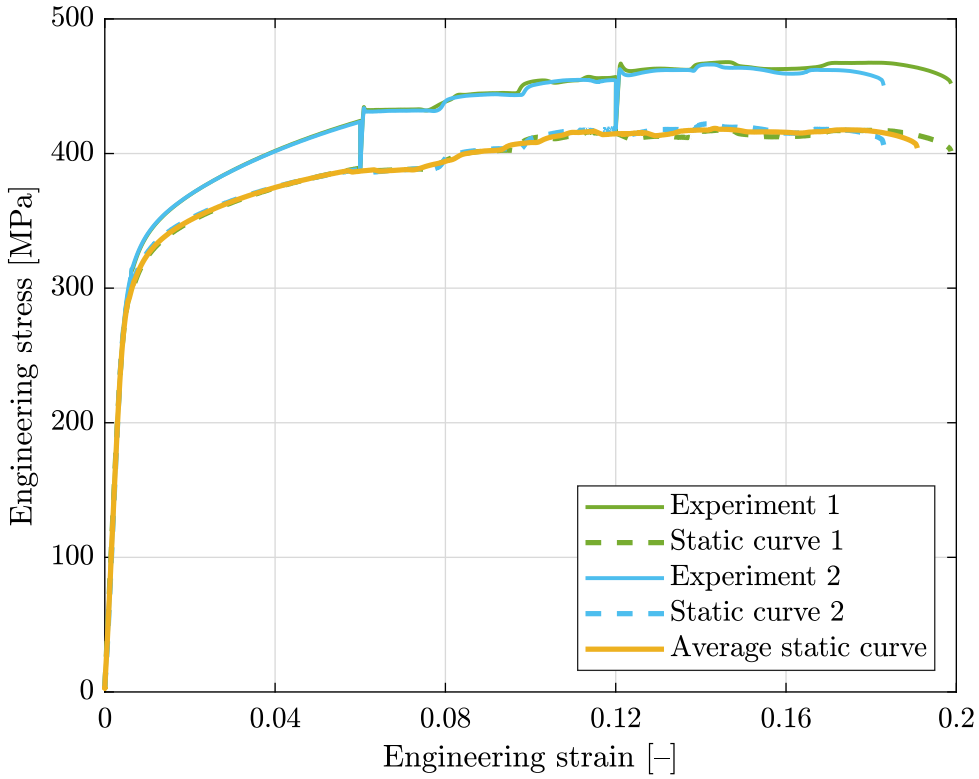

Figure 7.3: Static curve – AW 2024–T351

7.4 Curve fitting in MATLAB

There are numerous iterative approaches in MATLAB for determining material parameters. For example, the least-squares method is available. However, for higher accuracy, it is advantageous to use one of the artificial intelligence algorithms, which is why the PSO algorithm whose principle was described in the section 3.5 of this thesis was used. In MATLAB, the function `params` is used to define the equation (7.11) that describes the Johnson–Cook material model and the parameters we want to determine are defined as unknowns. The function `particleswarm` then determines all unknown constants in an iterative way within predetermined limits so that the curve describing the material model meets the desired precision according to the function setting. The following settings were used to determine the parameters in this thesis:

- (`SwarmSize`) – The number of particles was set to 10 000. Each particle represents a possible solution to the optimization problem.
- (`MaxIterations`) – Optimization is limited to 100 iterations.
- (`Display`) – The optimization progress is displayed iteratively to track its convergence.

- (`FunctionTolerance`) – Optimization ends if the change in the objective function value between iterations falls below 10^{-6}.
- (`MaxStallIterations`) – The algorithm terminates if the value of the objective function does not improve after 3 iterations.

However, in order to determine the material parameters, it is necessary to define a number of input parameters including the reference strain rate, the reference temperature, the melting temperature, the initial guess of the parameters, and the upper and lower limits of the parameters. The reference temperature for all tests was room temperature $T_r = 22$ °C. For computational reasons, it is necessary to calibrate the material parameters to the curve with the lowest strain rate. This is usually a quasi-static test, but in this thesis a static curve was also determined, and thus chosen as the starting point for determining the first part of the material model defining the plastic hardening. Since it is not possible to assume a zero strain rate which should theoretically correspond to the static curve, the loading rate of the static curve was chosen to be $v = 0.01\,\mathrm{mm/min}$ which corresponds to the strain rate $\dot{\varepsilon}_r = 6 \cdot 10^{-6}\,\mathrm{s}^{-1}$. This value is two orders of magnitude lower than the quasi-static test value. Other necessary parameters such as melting temperature depend on the material, and these values will be given in the next section of this work.

The determination of material parameter values is iterative and incremental. The material parameters A, B and n are determined first on the basis of the static curve. The determination is based on the initial input guess parameters, which may be based on knowledge of the material or other calibrations already performed. Since the algorithm tends to zero out some parameters completely, and other parameters grow too high at their expense, it is necessary to constrain the range of the upper and lower bounds on the parameters.

Next, we proceed with the determination of the parameter C that describes the effect of the velocity. To direct it, the experimental data must be used which have a higher strain rate than the reference data, and thus the effect of velocity is present. For all materials in this work, this was the case for the quasi-static and dynamic tests. Each of the tests has a different ideal value of the parameter C, hence the need to choose a compromise between these values so that the resulting parameter value represents all curves as ideal as possible with the least possible deviation. In cases where the velocity parameter varies too much and it is not possible to find an ideal value, it is advisable to adjust the predefined parameters A, B, and n which also affect the subsequent size of the parameter C.

Since the temperature experiments were performed at quasi-static velocities, the effect of velocity is also apparent. This fact should be kept in mind not only in the subsequent numerical calculation, but especially in the determination of the temperature exponent m. When obtaining the temperature parameter, the values A, B, n and C are fixed and the effect of temperature on the material is determined in the same way as for the effect of velocity.

From the needs for numerical simulations, after obtaining the material parameters, the true stress–strain curve is extrapolated (calculated) to a higher strain values (e.g. strain 1 or 2, or any other necessary value) so that the obtained data can be used for numerical simulation. An example of curve fit and extrapolation in a quasi-static test is shown in the graphs in Fig. 7.4.

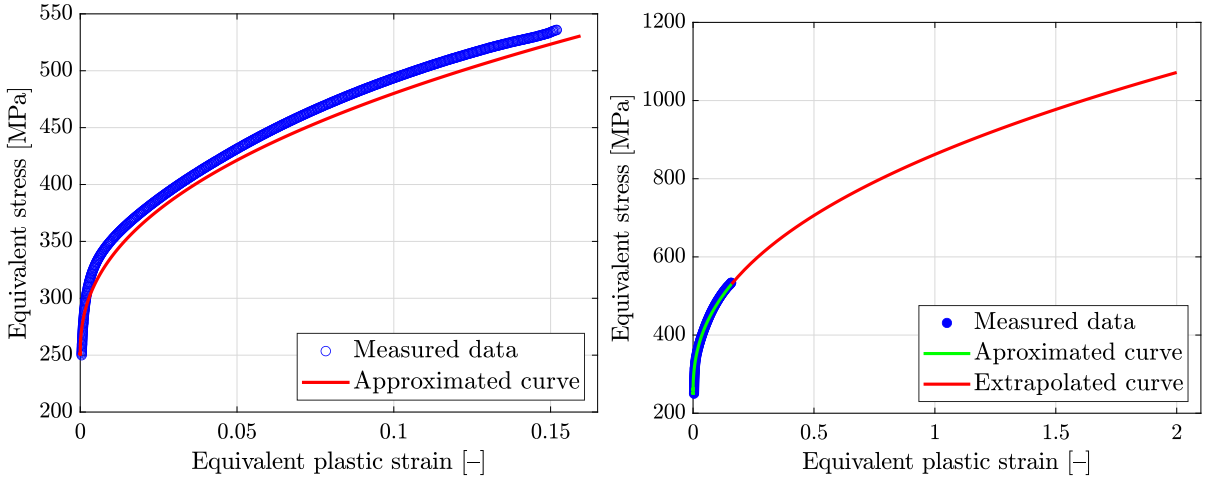

Figure 7.4: Calibration for quasi-static test and extrapolation for numerical simulation

After all the material parameter values have been determined, the next iteration is carried out with an attempt to refine them based on the values obtained from the previous iteration. Afterwards, to obtain satisfactory accuracy, the parameters are validated by FEM calculation and the simulation results are compared with the experimental results.

8 Material model calibration

The entire process of determining the material parameters is used to determine the possibility of using the given material in numerical simulations to calculate the stress and strain values in the structural design of various components made of the given material. Therefore, it is necessary to verify that the material parameters actually represent the material behaviour in numerical simulations using FEM and that is why a tensile test simulation is performed and then the simulation vs. experiment results are compared.

Ansys Workbech 2024 R2 and LS-DYNA R15 (marked on the SVS FEM website as LS-DYNA STUDENT 2024 R1) were used for parameter validation. Ansys Workbench modules were mainly used for parameter validation. Specifically, these were the Static Structure, Transient Structure, and LS-DYNA modules and then the classic LS-DYNA environment i.e. LS-PrePort V4.10.11 and LS-Run 2024 R1 with implicit solver.

Since modules such as Static Structural and others do not directly include the option to set the Johnson–Cook material model, the material was modelled using Isotropic Elasticity and Multilinear Isotropic Hardening. The exptrapolated values obtained in MATLAB as described in the previous chapter were inserted into the plastic section. In the simulations, large deflections and other modules required for proper convergence of the problem were enabled. The Explicit Dynamics module was subsequently used to capture the effect of velocity, but since the classical concept of "dynamic simulation" refers to an event that takes on the order of tenths of seconds, simulating a tensile test that lasts in units of seconds is a very long task that cannot be computed with the available computing power. Therefore, the calculation was performed in the LS-DYNA environment.

Moreover, to be able to state the correctness of the material parameters across all influences, it is suitable to select a module for all simulations that manages to calculate all possible variations of the acting environmental influences. The best choice for this is LS-DYNA, specifically its implicit solver, which makes it possible to compute "static", quasi-static, dynamic (dynamic in the sense of this thesis) and temperature problems.

8.1 Analysis settings

The initial setup of the simulation was performed in Ansys Workbench 2024 R2 in the LS-DYNA module. This is because this environment has a user-friendly graphical interface, allowing for faster and easier setup due to the ability to share geometry or material parameters across simulations.

8.1.1 Geometry and boundary conditions

All experiments used to determine the parameters of the material were performed on specimens with circular cross-sections. Thus, it is convenient to use the axisymmetry and symmetry of the specimen in the simulation. The geometry was modelled in the SpaceClaim modeller included in Ansys Workbench 2024 R2. The specimen is modelled without clamping parts with only half of the measured length, making the geometry a rectangle with basic dimensions taken from the size of the test specimen. For computational rea-

sons, an imperfection was introduced in the geometry to facilitate the formation of the neck. This imperfection took the form of reducing the bottom edge of the rectangle by 0.01 mm, see Fig. 8.1. As a result, the calculation is not too demanding on computational power and time, which is very useful for the procedure when adapting material parameter values. A graphical representation of the geometry used is shown in Fig. 8.1.

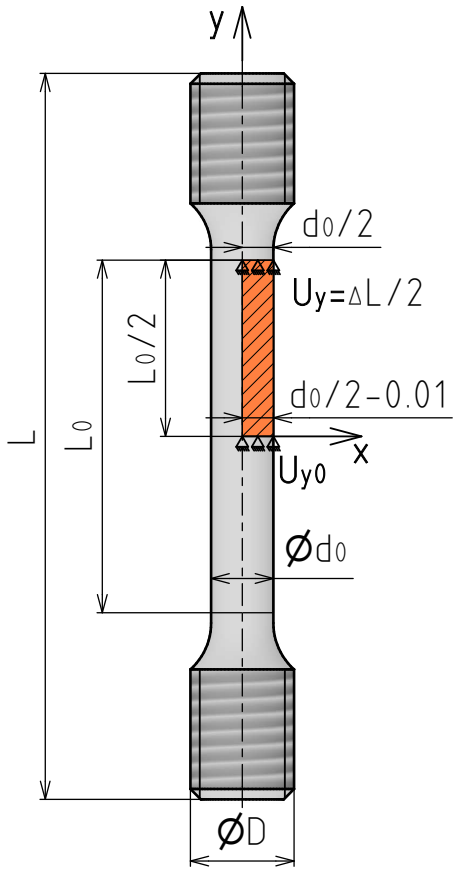

Figure 8.1: specimen geometry and boundary conditions

As can be seen from the drawing on Fig. 8.1, the boundary conditions are set to zero displacement in the y-axis on the specimen symmetry axis. Next is the displacement in the y-axis at the top edge of the specimen. Its value corresponds to half the measured elongation of the specimen in the experiment. Thus, this is a deformation load, which is more advantageous in terms of convergence of the problem. Of course, the problem is set up as axisymmetric along the y-axis which makes it completely determined in space and avoids the formation of singular matrices during the calculation.

The boundary conditions can include the simulation time setting. The time setting is crucial here because it controls the deformation of the specimen during the simulation. The set simulation time corresponds to the time of the test – for dynamic, the times are in units of seconds, for quasi-static, the times are already in the order of minutes. The deformation load is set to increase linearly with the time step and at the end of the time interval in "End Time" corresponds to the measured value in the experiment - it is possible to faithfully simulate the tensile test only in this way.

8.1.2 Finite element mesh

SHELL elements are used as finite elements in the 2D task. The mesh is set as mapped with a global element size of 0.1 mm. Such a fine mesh is chosen because of the critical wave spreading or critical time step size and to obtain correct results. The finite element mesh can be seen in Fig. 8.2.

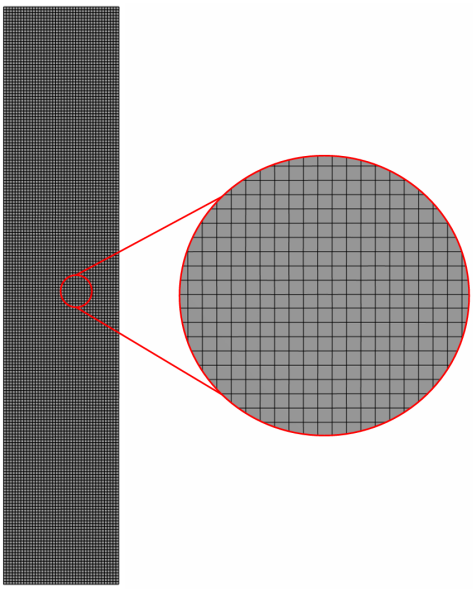

Figure 8.2: Finite element mesh

8.1.3 Material model

The material model was also set up in Ansys Workbench in the Engineering Data environment, however, its subsequent addition and possible modifications were also made in the *.k file in the text editor before running the simulation.

The elastic part of the material behaviour is modelled using Isotropic Elasticity, where material constants for elastic behaviour are given. Specifically, these are Young's modulus E and Poisson's ratio ν. In addition, the material is supplemented with density ρ.

The LS-DYNA implicit solver has only the complete Johnson–Cook material model defined for mathematical reasons. In LS-DYNA, this material model is denoted as *MAT_015 (*MAT_15). In Engineering Data, this model is contained in the LS-DYNA External Model – MAT tab with the designation *MAT_JOHNSON_COOK. In this module, the calculated material parameters A, B, n, C and m are given as well as Melting temperature T_m, Room (reference) temperature T_r, Quasi-static Threshold Strain Rate (epso), which corresponds to the rerefence strain rate $\dot{\varepsilon}_r$ (this parameter is the reason why it is necessary to calibrate the material parameters to the test with the lowest strain rate) and Specific Heat (cp). For computational reasons, the material model *MAT_15 must be supplemented with an Equation of state (EOS) [78]. The Ansys Workbench and LS-DYNA software also have a simplified version of the Johnson–Cook material model. In LS-DYNA is denoted as *MAT_098. This has the advantage of not requiring the EOS and needing fewer parameters than the full Johnson–Cook model. Unfortunately, the simplified Johnson–Cook model is only available for the explicit solver.

In LS-DYNA, it is necessary to add an EOS when using the *MAT_015 material model, because this material model does not calculate the hydrostatic component of

stress (pressure). The EOS is responsible for calculating the pressure based on changes in volume, density, and possibly energy or temperature. In axisymmetric simulations, where significant volume changes and high pressures are involved, an accurate pressure calculation is crucial to the correct modelling of material behavior. Without an EOS definition, the simulation would not be able to correctly capture these volume effects, leading to inaccurate results or calculation failures [78].

For this reason, the material model was supplemented with a simple EOS with a Bulk Module. In the Engineering data, this equation is denoted as *EOS_LINEAR_ POLYNOMIAL and the value of the parameter c1 corresponds to the value of the Bulk modulus [78].

In the case of a temperature–dependent problem, the temperature–dependent material must also be defined for the simulation. The set temperatures in the *MAT_15 model only relate to the constitutive relation where the temperature softening due to material deformation is calculated. For very fast processes, heat is generated due to deformation, which can affect the stress state of the solid and is thus simulated by this approach. However, in cases where we want to simulate the heating of the specimen to the desired temperature and solve for heat conduction through the material, we must supplement *MAT_15 with *MAT_THERMAL under the same material ID and then turn on the temperature effect in the model. The material temperature was set using a text editor directly in the *.k file.

The reason is that the material temperature cannot be set directly in the LS-DYNA module when solving the problem in Ansys Workbench and, more importantly, it is not possible to read the reaction force values from the boundary condition PRESSCRIBED_MOTION_SET that LS-DYNA defines in Ansys Workbench. In addition, if we want to solve the problem using an implicit dynamic solver, it is more convenient to perform the calculation in LS-Run, which stores the progress results of the simulation in text files that can also be monitored in LS-PrePost during the calculation. For these reasons, the simulation was exported from Ansys Workbench at this stage as a *.k file with the settings described above.

8.1.4 Modifying settings

As already mentioned in the previous section, it is necessary to partially modify the set simulation before starting the calculation - the part of the modification was performed in the LS-PrePost environment.

In LS-PrePost, the boundary condition PRESCRIBED_MOTION_SET in the specimen symmetry axis has been changed to SPC_SET to list the reaction force in the bond. Eventually, the reaction force can also be retrieved using NODAL_FORCE_GROUP. In addition, HISTORY_NODE_SET has been defined to allow the possibility of listing the length change as a function of the reaction force. For temperature tasks, TEMPERATURE_SET was also defined with the temperature value depending on the test type.

The other tasks were then performed using a text editor directly in the *.k file. It was necessary to define the parameters of the Implicit Solver using the CONTROL_IMPLICIT_ GENERAL command and its associated commands. To include the dynamic effects and strain rate sensitivity, the dynamic implicit solver defined by CONTROL_IMPLICIT_ DYNAMICS was used and in the case of the temperature problems, it was also necessary to define the time step of the temperature analysis using CONTROL_THERMAL_TIMESTEP. The complete setup of all simulations performed can be

viewed in detail in Appendix B *.k files, which contains the *.k files of all simulations. The simulations prepared in this way could be computed in LS-Run.

8.2 Processing of results and comparison of simulation and experiment

When processing the results of the axisymmetric simulation in LS-DYNA, the force–displacement curve was obtained by combining data from the files `spcforc` and `nodout`. The force was read from the file `spcforc`, which contains the reaction forces acting in the direction of the prescribed motion at the nodes defined in SPC_SET. As this is the axisymmetric problem, the forces given in `spcforc` are related to the unit section in radians and therefore the resulting value had to be multiplied by a factor of 2π to match the actual total force applied across the specimen.

The corresponding displacement was obtained from the file `nodout` as the displacement of one of the nodes in the load direction. Since only half of the specimen was simulated, the displacement value had to be multiplied by two to match the actual displacement of the entire body. From these data, a force–displacement curve was then constructed as an x-y plot, with the recalculated displacement plotted on the x-axis and the recalculated force plotted on the y-axis. This approach allowed for an accurate interpretation of the mechanical response of the model under axisymmetric loading.

By listing and then plotting the values, it is possible to compare the simulation and experimental runs and also show the clear influence of strain rate and temperature on the simulation results. The simulation results obtained and their comparison with the experimental results are shown in Figs. 8.3, 8.4 and 8.5. In the left part, there are always results of the simulations themselves, and in the right part, the comparison with experiments for individual materials is shown.

No size effect is included in the simulations because the chosen Johnson–Cook material model is unable to capture it.

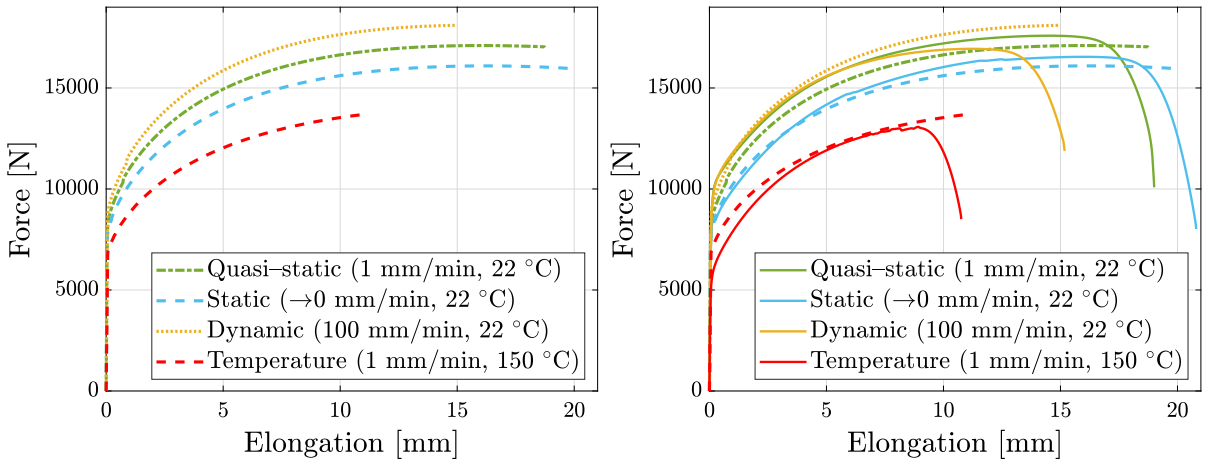

Figure 8.3: Results from simulation and its comparison with experiments – SS 316L

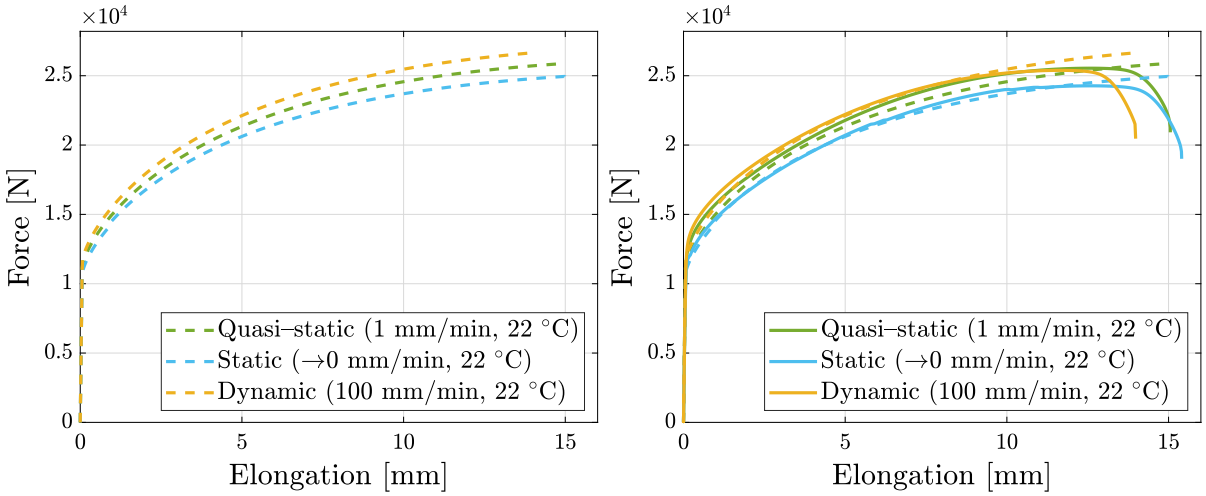

Figure 8.4: Results from simulation and its comparison with experiments – Inconel 718

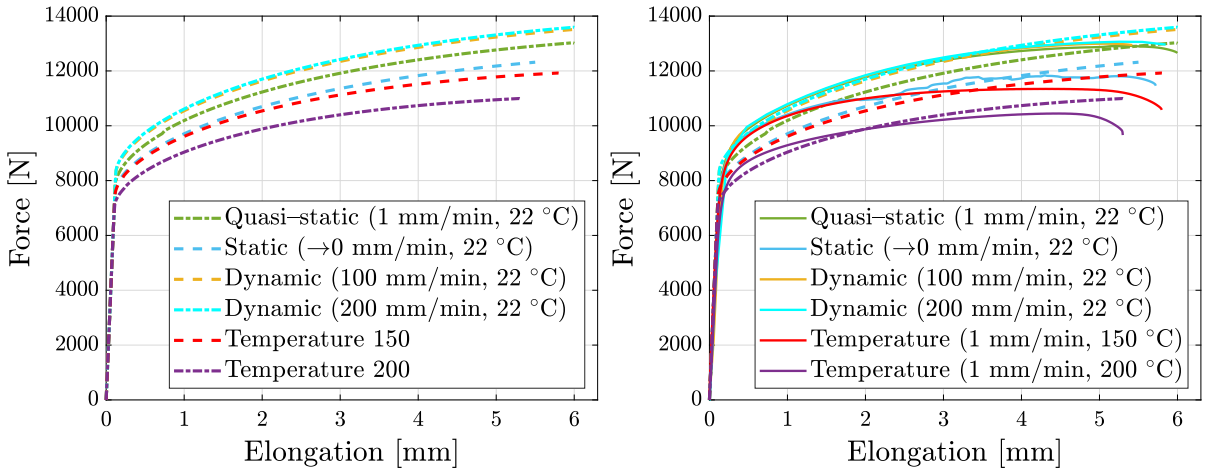

Figure 8.5: Results from simulation and its comparison with experiments – AW 2024–T351

9 Results and discussion

9.1 Results for stainless steel 316L

In the graphs shown in Fig. 9.1, flow curves for 316L stainless steel are presented. The left-hand graph displays the dependence of equivalent stress on equivalent plastic strain for various strain rates. This graph represents a "cross-section" of the response surfaces depicted in Fig. 9.2, evaluated at the reference temperature. The right-hand graph illustrates the influence of temperature on the response of the material at the reference strain rate. The selected values of strain rate and temperature correspond to the specific conditions under which the experiments were conducted.

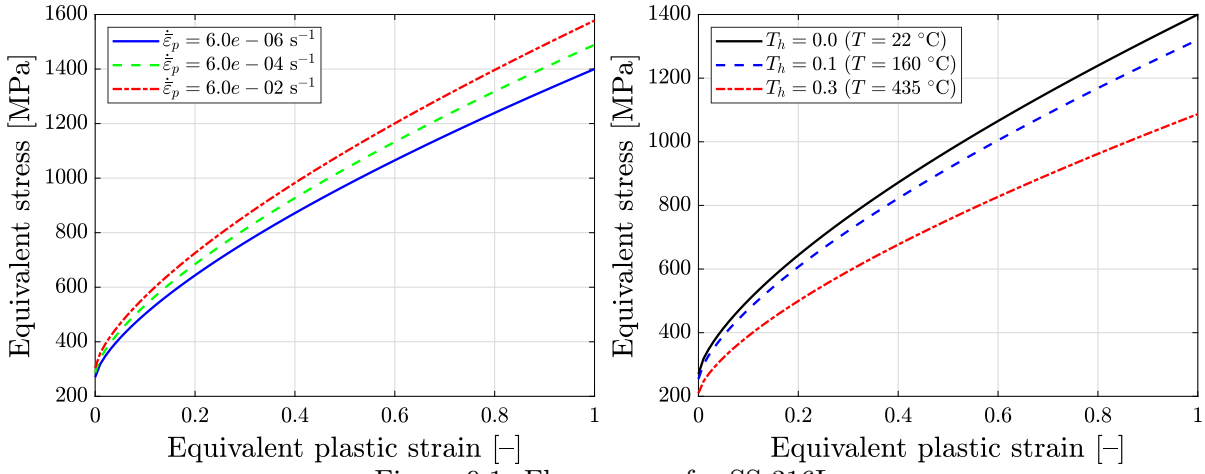

Figure 9.1: Flow curves for SS 316L

Table 9.1: Parameters of Johnson–Cook material model and used properties for SS 316L

E (Youngu's modulus)	193 000	[MPa]	
ν (Poisson's ratio)	0.3	[–]	
ρ (Density)	8 000	[kg m^{-3}]	
K (Bulk modulus)	160 830	[MPa]	
$\boldsymbol{A}$ (Yield strength)	**270**	[MPa]	
$\boldsymbol{B}$ (Hardening constant)	**1130**	[MPa]	
$\boldsymbol{n}$ (Strain hardening exponent)	**0.6877**	[–]	
$\boldsymbol{C}$ (Strain rate coefficient)	**0.0138**	[–]	
$\boldsymbol{m}$ (Temperature exponent)	**1.2441**	[–]	
$\dot{\bar{\varepsilon}}_{\mathbf{r}}$ (Reference strain rate)	$\mathbf{6 \cdot 10^{-6}}$	[s^{-1}]	
T_r (Reference temperature)	22	[°C]	
T_m (Melting temperature)	1400	[°C]	[79]
cp (Specific heat)	500	[J kg^{-1} K^{-1}]	[79]
tc (Thermal conductivity)	15	[W m^{-1} K^{-1}]	[80]

All values of the determined material parameters of Johnson–Cook material model for the 316L material were used to generate reference curves and surfaces for Figs. 9.1 and 9.2 and are listed in the table 9.1 that include all other material parameters necessary for numerical simulations of this material.

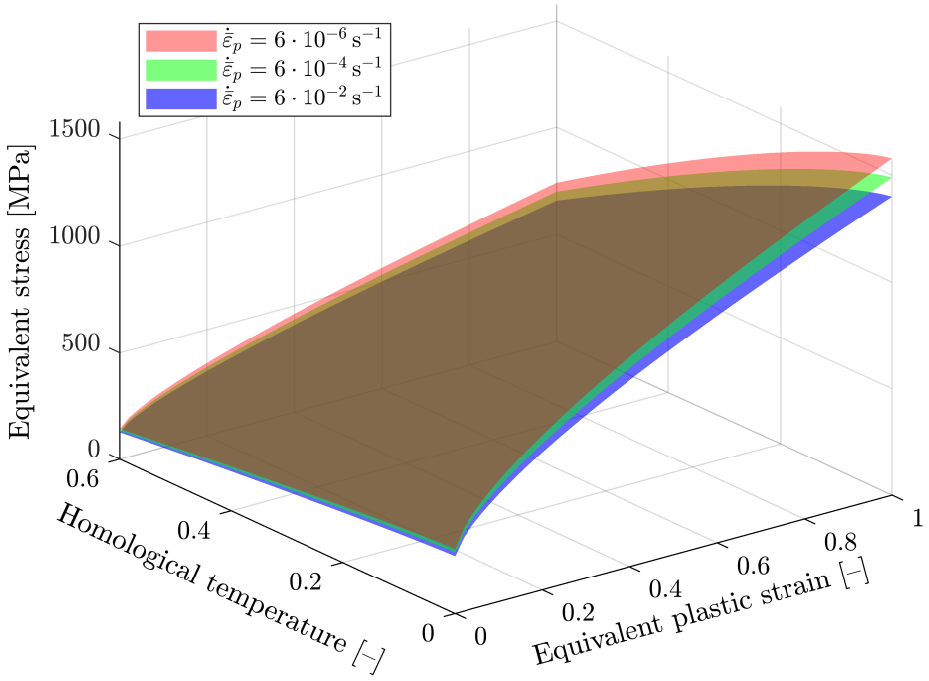

Figure 9.2: Johnson–Cook response surfaces for SS 316L

9.2 Results for Inconel 718

In a similar way as the results for 316L are presented here, the results for Inconel 718 are also shown, with the difference that no temperature tests were performed on Inconel 718 and thus the temperature exponent could not be calibrated. Therefore, table 9.2 does not contain the parameter m nor the thermal conductivity value.

Since the temperature dependence of Inconel 718 cannot be determined, it is also not possible to plot the response surfaces, or even if the response surfaces are plotted. The surfaces will be constant again for homological temperature. Thus, only flow curves were plotted. Therefore, Fig. 9.3 shows the flow curves for different strain rate values based on the material parameters determined for Inconel 718.

According to the parameter of effect of the very low loading rate, it can be concluded that the additively manufactured Inconel 718 is very resistant to the increase in the strain rate in the studied range. Among all the materials studied, it shows the best properties in this respect, proving that its use is suitable for **dynamic applications** in aerospace, aviation and other applications. As has already been mentioned, the temperature influence has not been determined. Therefore, there is an opportunity to extend this work in the future in an attempt to add a temperature-dependent parameter to the already determined parameters to be able to simulate the material in a complex spectra including thermal loading.

Table 9.2: Parameters of Johnson–Cook material model and used properties for Inconel 718

E (Youngu's modulus)	202 000	[MPa]	
ν (Poisson's ratio)	0.34	[–]	
ρ (Density)	8 190	[kg m^{-3}]	
K (Bulk modulus)	210 420	[MPa]	
$\boldsymbol{A}$ (Yield strength)	**380**	[MPa]	
$\boldsymbol{B}$ (Hardening constant)	**1821**	[MPa]	
$\boldsymbol{n}$ (Strain hardening exponent)	**0.718**	[–]	
$\boldsymbol{C}$ (Strain rate coefficient)	**0.0086**	[–]	
$\boldsymbol{m}$ (Temperature exponent)	–	[–]	
$\dot{\bar{\varepsilon}}_{\mathbf{r}}$ (Reference strain rate)	$\mathbf{6 \cdot 10^{-6}}$	[s^{-1}]	
T_r (Reference temperature)	22	[°C]	
T_m (Melting temperature)	1300	[°C]	[81]
cp (Specific heat)	435	[J kg^{-1} K^{-1}]	[81]
tc (Thermal conductivity)	–	[W m^{-1} K^{-1}]	

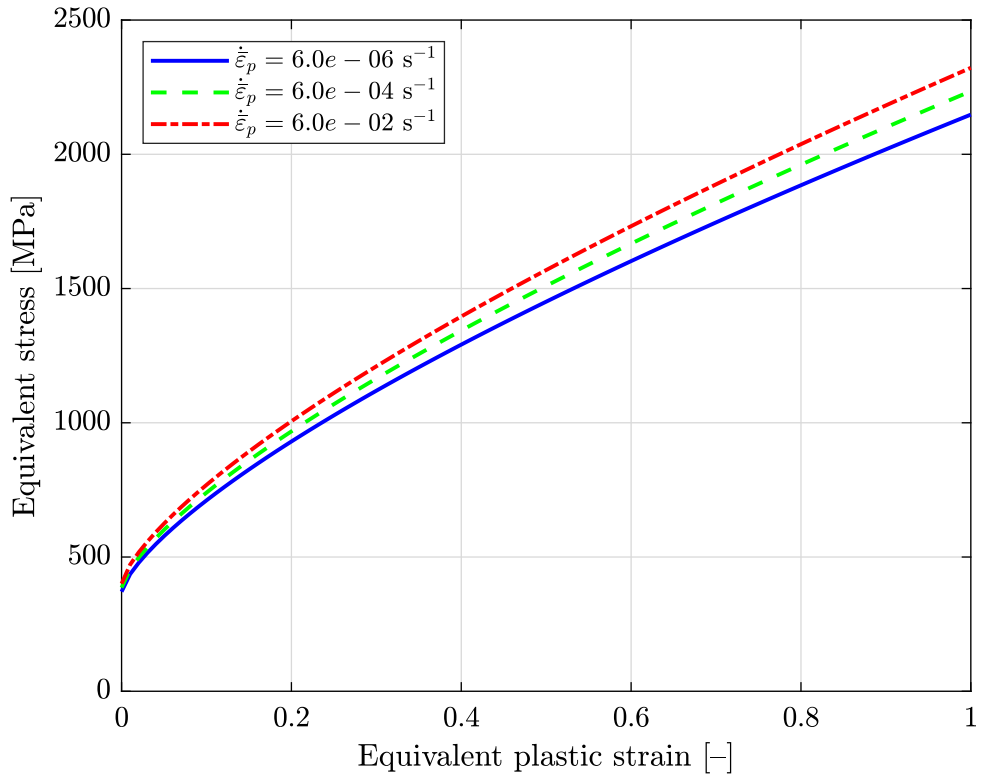

Figure 9.3: Flow curves for Inconel 718

9.3 Results for AW 2024–T351

The last material investigated is an aluminium alloy designated as AW 2024–T351. The same as for other materials, the material parameters of the Johnson–Cook material model were determined for this alloy and are listed in the table 9.3.

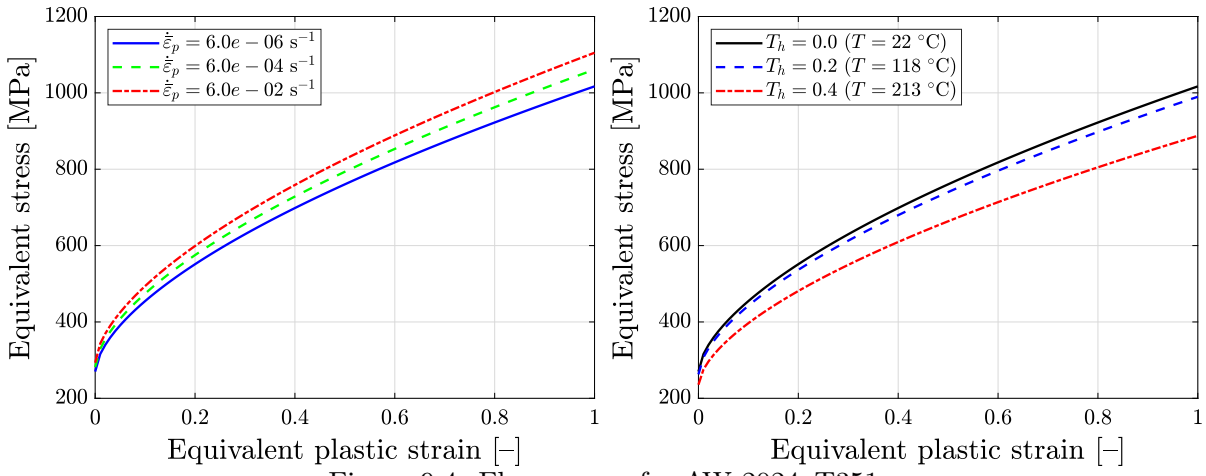

Figure 9.4: Flow curves for AW 2024–T351

Based on the results shown in Figs. 9.4 and 9.5, it can be concluded that the alloy AW 2024–T351 shows **an expressive temperature sensitivity**, which is reflected in a clear decrease in stress with increasing homologous temperature. In contrast, the **sensitivity to the strain rate is very low**, which means that the stress response changes only minimally with increasing strain rate.

For this reason, the alloy is particularly suitable where rapid loading of components occurs (e.g. shock loads, vibration or short-term stress peaks), provided the operating temperature is low to medium. This corresponds, for example, to use in aerospace structures, drone frames, racing cars or portable applications where low weight and strength under dynamic loading is a priority.

Table 9.3: Parameters of Johnson–Cook material model and used properties for AW 2024–T351

E (Youngu's modulus)	72 500	[MPa]	
ν (Poisson's ratio)	0.34	[–]	
ρ (Density)	2 780	[kg m^{-3}]	
K (Bulk modulus)	75 520	[MPa]	
$\boldsymbol{A}$ (Yield strength)	**270**	[MPa]	
$\boldsymbol{B}$ (Hardening constant)	**747**	[MPa]	
$\boldsymbol{n}$ (Strain hardening exponent)	**0.607**	[–]	
$\boldsymbol{C}$ (Strain rate coefficient)	**0.0094**	[–]	
$\boldsymbol{m}$ (Temperature exponent)	**2.25**	[–]	
$\dot{\bar{\varepsilon}}_\mathbf{r}$ (Reference strain rate)	$\mathbf{6 \cdot 10^{-6}}$	[s^{-1}]	
T_r (Reference temperature)	22	[°C]	
T_m (Melting temperature)	500	[°C]	[82]
cp (Specific heat)	875	[J kg^{-1} K^{-1}]	[82]
tc (Thermal conductivity)	121	[W m^{-1} K^{-1}]	[82]

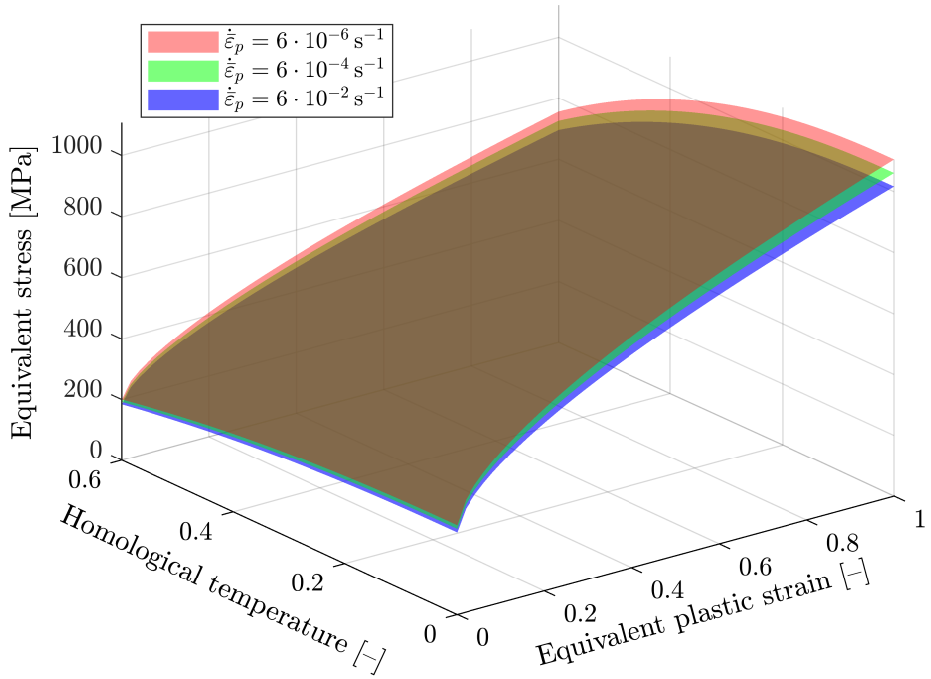

Figure 9.5: Johnson–Cook response surfaces for AW 2024–T351

9.3.1 Size effect for AW 2024–T351

In this work, the alloy AW 2024–T351 was the only material for which mini-test experiments were also performed. This made it possible to show the size effect, i.e. the influence of the specimen size on the resulting engineering stress and strain values.

The size effect is already clearly visible on the individual types of specimen tested. As can be seen in Fig. 9.6, the differences between the specimens are quite large. If we compare the specimen of type tensile_16 with the specimen tensile_32, the difference in the resulting engineering stress is in lower tens of MPa – such difference is due to the size effect. According to the dimensions in Fig. 5.6, the tensile_32 specimen is two times wider and thicker than the tensile_16 specimen and this change in dimensions has a significant effect on the material response.

It should be noted that tests were carried out only in COMTES FHT and not in the laboratory on an improved miniature testing device. This is because the device had problems with the stepper motor that need to be solved and lies outside the scope of this thesis.

The fact that there is a difference between miniature and standard specimens is well illustrated by comparing the mini specimens with the quasi-static test. In the graph in Fig. 9.6, it is clearly visible that all the tensile curves determined from the mini specimens show a lower engineering stress value compared to the conventional quasi-static curve. Parameters such as temperature and strain rate are consistent across the tests. Thus, the only influence on the hardening of the material is the size effect. At the same time, there is not only an influence on the engineering stress value but also a very significant reduction in the achieved strain. The strain is almost half as high in the mini specimens compared to the conventional one. This difference is attributed to the influence of the size effect, where the shorter length of the deformable part limits the development of a uniform plastic flow and promotes earlier localization of deformation, as well as the influence of

the outer grains and its size.

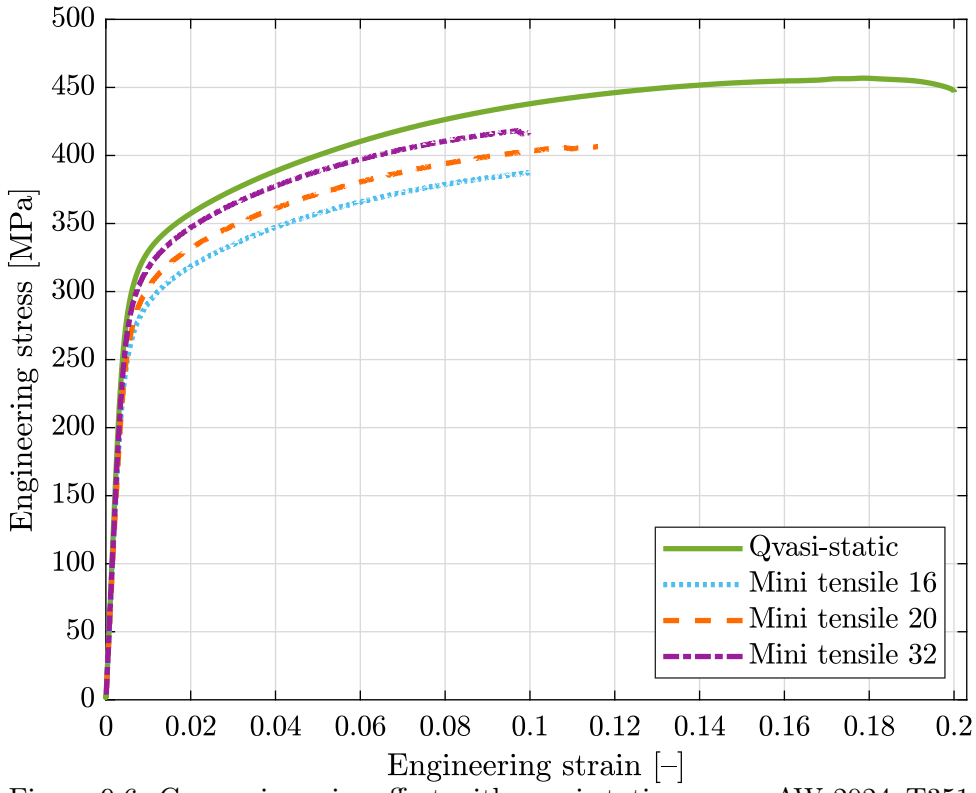

Figure 9.6: Comparison size effect with quasi-static curve – AW 2024–T351

This phenomenon can fundamentally affect the applicability of a given material type in the design of components and also leads to a significant risk during the FEM simulations of components with small parts. If the material model is calibrated without the size effect, it can lead to an unrealistic material response in the case of thin or very small parts of the structure, and thus to an incorrect prediction of deformation or failure.

A comparison of the size effect can be found in the table 9.4. The table lists the cross sections of each specimen. The reduction in cross sections as a percentage provides a good comparison of the size changes. This indicates how the size of the miniature specimen has been reduced relative to the quasi-static specimen. For comparison purposes, the engineering stress corresponding to a value $\varepsilon = 0.8$ [–] is also listed, along with the percentage decrease of this stress relative to the quasi-static value.

Table 9.4: The effect of a change in cross section on the value of engineering strain

Specimen	Section area [mm^2]	Reduction of section area [%]	Engineering stress in $\varepsilon = 0.8$ [MPa]	Reduction of stress [%]
Quasi-static	28.27	–	426	–
Tensile_16	0.64	97.3	379	11
Tensile_20	1	96.5	394	7.5
Tensile_32	2.56	90.9	410	3.8

The Johnson–Cook model, used in this work to describe the material behaviour of the materials under study, does not include the size effect. By this, it is necessary to complement this model with a suitable model which includes the size effect. Examples of the size effect models were presented at the beginning of this work. However, their specific implementation should be thoroughly verified before practical application and alternative solutions should be considered if necessary.

10 Conclusion

The aim of this thesis was to analyze the effects of size, temperature, and strain rate on the hardening behavior of metallic materials and to apply these findings in the calibration of a material model. The study was carried out on three types of materials: stainless steel 316L, Inconel 718, and aluminum alloy AW 2024–T351. An integral part of the work was the development of a miniature testing device, which enables experiments focused on the size effect. In parallel, an experimental procedure for miniature testing was proposed, adapted to the specific modifications of the testing setup.

In the introductory part of this thesis, a literature review was carried out focusing on the mechanisms of strain hardening in metallic materials, with particular attention paid to the individual factors investigated in the experimental part. Material models that account for these effects were identified, which offer potential for use in the calibration of material parameters within FEM simulations. The review also included a study of various miniature testing approaches, their potential for partial or full automation, and their applicability to accelerate the development of new materials, particularly due to the reduced material requirements for specimen production. Based on the findings of these studies, several modifications were made to the existing miniature testing apparatus in the laboratory.

One of the key components of this work was the modification of the miniature testing device. Major improvements included a newly designed holder for the DIC camera, which captures the deformation of the specimen, and redesigned gripping claps that ensure reliable and slip-free clamping of the specimen, thereby preventing experimental errors previously caused by slippage. The lower crosshead was also replaced to ensure accurate force transmission to the load cell and to maintain the uniaxial tensile load of the specimen. In connection with these modifications, a new specimen clamping method was developed. The addition of custom designed fixtures for easier handling and more precise alignment of the specimen effectively eliminated the risk of errors due to improper manipulation or misalignment during clamping.

Before the effects of individual boundary conditions could be determined, it was necessary to select an appropriate testing method and define its parameters according to the applicable standards for the mechanical testing of materials. The most suitable method proved to be uniaxial tensile testing, which was carried out in several variants: classical quasi-static tensile tests, elevated temperature tensile tests, and dynamic tensile tests performed at increased loading rates. To capture a broader range of strain rates, additional tensile tests with intermediate holds – so-called static drops – were performed. These allowed for the calibration of a purely static material curve, free from strain rate effects, thus representing the material's true static response.

All measured data were processed in the MATLAB software after the experiments. The reference curves of a given experiment were successively determined and used for subsequent curve fitting and determination of the material parameters. The Johnson–Cook material model was chosen as the material model that captures the effect of velocity and temperature also because of its implementation in the FEM simulation software. For

curve fitting, the possibility of artificial intelligence–based PSO was used, since the least squares method was not ideal for this task as it is strongly affected by local minima and initial estimation of material constants. Due to the proper implementation of PSO in the MATLAB script, the material model parameters were determined with high accuracy. The Johnson–Cook material model parameters were calibrated with respect to the simulation in the FEM environment by calibrating them to the reference values of the strain rate corresponding to the static curve. Subsequently, they were validated in LS-DYNA software to simulate the tensile tests of each material under the loads of the corresponding experiments. The results of the simulations and experiments were then compared. Ansys Workbech software and its various modules were also used in this activity, which resulted in a series of the Johnson–Cook material model parameters that can be used for subsequent numerical simulations in the FEM codes for the materials investigated in this work.

The simulations did not take into account the effect of size, which is not included in the Johnson–Cook material model. However, the size effect has been clearly described in the example of the tested AW 2024–T351 miniature specimens. This thesis does not include any data measured on the modified minitesting equipment – that is due to the fact that before a satisfactory set of data could be measured, a failure occurred on the stepper motor used to load the specimen. However, the work was not affected in any way by this event and the goals set out in the assignment were fully achieved.

The greatest benefits of this work for prospective future studies are the possibility of using the determined material parameters for numerical simulations and, especially, the extension of the possibilities of a miniature testing device in the laboratory. The modifications and the adapted procedure make the minitesting more accurate and faster. Thus, it is proposed to use this background for the development of future works dealing with minitesting of materials to better understand the effect of size on the hardening of metallic materials and the possibility of implementing the newly acquired knowledge in numerical simulations. In addition, the miniature testing device can be further improved to be ready for in situ measurements using scanning electron microscopes.

List of References

[1] BEERLI, T.; ROTH, Ch. C.; MOHR, D. Semi-automatic miniature specimen testing method to characterize the plasticity and fracture properties of metals. *Acta Materialia*. 2024, vol. 263, p. 119539. Available from DOI: 10.1016/j.actamat.2023.119539.

[2] KAMAYA, M.; KAWAKUBO, A. A procedure for determining the true stress-strain curve over a large range of strains using digital image correlation and finite element analysis. *Mechanics of Materials*. 2011, vol. 43, no. 5, pp. 243–253. Available from DOI: 10.1016/j.mechmat.2011.01.002.

[3] GÜDEN, M.; ENSER, S.; BAYHAN, M.; TAŞDEMIRCI, A.; YAVAŞ, H. The strain rate sensitive flow stresses and constitutive equations of a selective-laser-melt and an annealed-rolled 316L stainless steel: A comparative study. *Materials Science and Engineering: A*. 2022, vol. 838, p. 142743. ISSN 0921-5093. Available from DOI: https://doi.org/10.1016/j.msea.2022.142743.

[4] LI, Z.; VOISIN, T.; MCKEOWN, J. T.; YE, J.; BRAUN, T.; KAMATH, C.; KING, W. E.; WANG, Y. M. Tensile properties, strain rate sensitivity, and activation volume of additively manufactured 316L stainless steels. *International Journal of Plasticity*. 2019, vol. 120, pp. 395–410. ISSN 0749-6419. Available from DOI: https://doi.org/10.1016/j.ijplas.2019.05.009.

[5] KOLOMY, S.; BENC, M.; HARANT, M., et al. Effect of different strain rates on mechanical behavior and structure of Inconel 718 produced by powder bed fusion. *International Journal of Mechanical and Materials Design*. 2025, vol. 21, pp. 1–16. Available from DOI: 10.1007/s10999-024-09724-6.

[6] WOOD, P.; RUSINEK, A.; PLATEK, P.; JANISZEWSKI, J.; SIENKIEWICZ, J.; GUNPUTH, U.F.; RAJKOWSKI, K.; MIGUÉLEZ, M.H. High strain rate effect on tensile ductility and fracture of AM fabricated Inconel 718 with voided microstructures. *Materials and Design*. 2021, vol. 208, p. 109908. ISSN 0264-1275. Available from DOI: https://doi.org/10.1016/j.matdes.2021.109908.

[7] KOURAYTEM, N.; CHANUT, R. A.; WATRING, D. S.; LOVELESS, T.; VARGA, J.; SPEAR, A. D.; KINGSTEDT, O. T. Dynamic-loading behavior and anisotropic deformation of pre- and post-heat-treated IN718 fabricated by laser powder bed fusion. *Additive Manufacturing*. 2020, vol. 33, p. 101083. ISSN 2214-8604. Available from DOI: https://doi.org/10.1016/j.addma.2020.101083.

[8] FORNI, D.; MAZZUCATO, F.; VALENTE, A.; CADONI, E. High strain-rate behaviour of as-cast and as-build Inconel 718 alloys at elevated temperatures. *Mechanics of Materials*.

2021, vol. 159, p. 103859. ISSN 0167-6636. Available from DOI: https://doi.org/10.1016/j.mechmat.2021.103859.

[9] WANG, C.; XU, J.; CHEN, X., et al. A modified Johnson–Cook model for 2A12 aluminum alloys. *Mechanics of Time-Dependent Materials*. 2024, vol. 28, pp. 2085–2104. Available from DOI: 10.1007/s11043-023-09611-1.

[10] HYDE, T. H.; SUN, W.; WILLIAMS, J. A. Requirements for and use of miniature test specimens to provide mechanical and creep properties of materials: a review. *International Materials Reviews*. 2007, vol. 52, no. 4, pp. 213–255. Available from DOI: 10.1179/174328007X160317.

[11] ZHENG, P.; CHEN, R.; LIU, H.; CHEN, J.; ZHANG, Z.; LIU, X.; SHEN, Y. On the standards and practices for miniaturized tensile test – a review. *Fusion Engineering and Design*. 2020, vol. 161, p. 112006. ISSN 0920-3796. Available from DOI: https://doi.org/10.1016/j.fusengdes.2020.112006.

[12] ZHANG, L.; HARRISON, W.; YAR, M. A.; BROWN, S. G. R.; LAVERY, N. P. The development of miniature tensile specimens with non-standard aspect and slimness ratios for rapid alloy prototyping processes. *Journal of Materials Research and Technology*. 2021, vol. 15, pp. 1830–1843. ISSN 2238-7854. Available from DOI: https://doi.org/10.1016/j.jmrt.2021.09.029.

[13] MAKWANA, D. N.; PATEL, A. K.; DAVE, K. G. A review of miniature specimen tensile test method of tungsten at elevated temperature. *International Journal of Engineering Development and Research*. 2016, vol. 4, no. 4, pp. 132–139. ISSN 2321-9939. Available also from: https://rjwave.org/ijedr/viewpaperforall.php?paper=IJEDR1604024.

[14] HECKMAN, N. M.; IVANOFF, T. A.; ROACH, A. M.; JARED, B. H.; TUNG, D. J.; BROWN-SHAKLEE, H. J.; HUBER, T.; SAIZ, D. J.; KOEPKE, J. R.; RODELAS, J. M.; MADISON, J. D.; SALZBRENNER, B. C.; SWILER, L. P.; JONES, R. E.; BOYCE, B. L. Automated high-throughput tensile testing reveals stochastic process parameter sensitivity. *Materials Science and Engineering: A*. 2020, vol. 772, p. 138632. ISSN 0921-5093. Available from DOI: https://doi.org/10.1016/j.msea.2019.138632.

[15] BOYCE, B.; SALZBRENNER, B. *Apparatus for high-throughput sequential tensile testing and methods thereof*. Inventor: B. BOYCE; B. SALZBRENNER. Publ.: 2021-03. Patent issued under number US 11,002,649 B1, United State Patent. Patent US 11,002,649 B1. Available also from: https://patentimages.storage.googleapis.com/86/42/c5/203cb05d4029f8/US11002649.pdf.

[16] RAN, J.Q.; FU, M.W.; CHAN, W.L. The influence of size effect on the ductile fracture in micro-scaled plastic deformation. *International Journal of Plasticity*. 2013, vol. 41, pp. 65–81. ISSN 0749-6419. Available from DOI: https://doi.org/10.1016/j.ijplas.2012.09.002.

[17] ZHANG, L.; HARRISON, W.; YAR, M. A.; MEHRABAN, S.; BROWN, S. G. R.; LAVERY, N. P. Use of miniaturized tensile specimens to evaluate the ductility and formability of dual phased steels for rapid alloy prototyping. *Materials Science & Engineering A*. 2023, vol. 875, p. 145075. Available from DOI: 10.1016/j.msea.2023.145075.

[18] DLOUHÝ, I. *Učební texty předmětu Deformace a porušování materiálů (RDF)*. Available also from: https://umvi.fme.vutbr.cz/students/summer?lang=cs. Accesed: 2025-03-28.

[19] ADÁMKOVÁ, K. *Vliv přípravy svarových ploch a způsobu upnutí na deformace svarů vysokopevných ocelí*. 2020. Available also from: https://dspace.cvut.cz/bitstream/handle/10467/89584/F2-DP-2020-Adamkova-Kristyna-DP_adamkova_3_8_20.pdf?sequence=-1&isAllowed=y. Diplomová práce. České vysoké učení technické v Praze, Fakulta strojní.

[20] HALL, E. O. The deformation and ageing of mild steel: III discussion of results. *Proceedings of the Physical Society. Section B*. 1951, vol. 64, no. 9, pp. 747–753. Available from DOI: 10.1088/0370-1301/64/9/303.

[21] PETCH, N. J. The cleavage strength of polycrystals. *Journal of the Iron and Steel Institute*. 1953, vol. 174, pp. 25–28.

[22] FAN, H.; WANG, Q.; EL-AWADY, J. A.; RAABE, D.; ZAISER, M. Strain rate dependency of dislocation plasticity. *Nature Communications*. 2021, vol. 12, p. 1845. Available from DOI: 10.1038/s41467-021-21939-1.

[23] DOWDING, I.; SCHUH, C. A. Metals strengthen with increasing temperature at extreme strain rates. *Nature*. 2024, vol. 630, pp. 91–95. Available from DOI: 10.1038/s41586-024-07420-1.

[24] COWPER, G. R.; SYMONDS, P. S. *Strain-hardening and strain-rate effects in the impact loading of cantilever beams*. 1957-09. Technical Report, AD0144762. Division of Applied Mathematics, Brown University. Available also from: https://archive.org/details/DTIC_AD0144762.

[25] GYLIENE, V.; OSTASEVICIUS, V. Cowper–Symonds material deformation law application in material cutting process using LS-DYNA FE code: turning and milling. In: *Proceedings of the 8th European LS-DYNA Users' Conference*. Strasbourg, France, 2011.

[26] JOHNSON, G.R.; COOK, W.H. A constitutive model and data for metals subjected to large strains, high strain rates and high temperatures. In: *Proceedings of the 7th International Symposium on Ballistics*. The Hague, The Netherlands, 1983, vol. 21, pp. 541–547.

[27] BAKHSHAN, H.; OÑATE, E.; CARBONELL I. P., Josep M. A review of the constitutive modelling of metals and alloys in machining process. *Archives of Computational Methods*

in Engineering. 2023, vol. 31, pp. 1611–1658. Available from DOI: 10.1007/s11831-023-10026-x.

[28] ARMSTRONG, R. W. *Hall–Petch relationship*. 2016. Available online: https://me.umd.edu/sites/enme.umd.edu/files/documents/Armstrong_EAIA2016.pdf [Accessed 10 May 2025].

[29] MIRZAIE, T.; MIRZADEH, H.; CABRERA, J.-M. A simple Zerilli–Armstrong constitutive equation for modeling and prediction of hot deformation flow stress of steels. *Mechanics of Materials*. 2016, vol. 94, pp. 38–45. ISSN 0167-6636. Available from DOI: https://doi.org/10.1016/j.mechmat.2015.11.013.

[30] SIM, K. H.; RI, Y. C.; JO, C. H.; KIM, O. J.; KIM, R. S.; PAK, H. Modified Zerilli-Armstrong and Khan-Huang-Liang constitutive models to predict hot deformation behavior in a powder metallurgy Ti-22Al-25Nb alloy. *Vacuum*. 2023, vol. 210, p. 111749. ISSN 0042-207X. Available from DOI: https://doi.org/10.1016/j.vacuum.2022.111749.

[31] SALVET, P. *Design of Miniature Specimens for Calibration of Ductile Fracture Criteria*. 2023. Available also from: https://www.vutbr.cz/studenti/zav-prace/detail/146390. Master's thesis. Brno University of Technology, Faculty of Mechanical Engineering, Institute of Solid Mechanics, Mechatronics and Biomechanics. Supervisor: F. ŠEBEK.

[32] WANG, J.L.; FU, M.W.; SHI, S.Q. Influences of size effect and stress condition on ductile fracture behavior in micro-scaled plastic deformation. *Materials & Design*. 2017, vol. 131, pp. 69–80. ISSN 0264-1275. Available from DOI: https://doi.org/10.1016/j.matdes.2017.06.003.

[33] RAULEA, L.V.; GOIJAERTS, A.M.; GOVAERT, L.E.; BAAIJENS, F.P.T. Size effects in the processing of thin metal sheets. *Journal of Materials Processing Technology*. 2001, vol. 115, no. 1, pp. 44–48. ISSN 0924-0136. Available from DOI: https://doi.org/10.1016/S0924-0136(01)00770-1.

[34] LAI, X.; PENG, L.; HU, P.; LAN, S.; NI, J. Material behavior modelling in micro/meso-scale forming process with considering size/scale effects. *Computational Materials Science*. 2008, vol. 43, no. 4, pp. 1003–1009. ISSN 0927-0256. Available from DOI: https://doi.org/10.1016/j.commatsci.2008.02.017.

[35] FU, M.W.; CHAN, W.L. Geometry and grain size effects on the fracture behavior of sheet metal in micro-scale plastic deformation. *Materials & Design*. 2011, vol. 32, no. 10, pp. 4738–4746. ISSN 0261-3069. Available from DOI: https://doi.org/10.1016/j.matdes.2011.06.039.

[36] MARTÍNEZ-PAÑEDA, E.; BETEGÓN, C. Modeling damage and fracture within strain-gradient plasticity. *International Journal of Solids and Structures*. 2015, vol. 59, pp. 208–215. ISSN 0020-7683. Available from DOI: https://doi.org/10.1016/j.ijsolstr.2015.02.010.

[37] LINDBLOM, D.; DAHLBERG, C. F.O. A strain gradient plasticity model to investigate diffusion and dynamic segregation of hydrogen. *European Journal of Mechanics - A/Solids*. 2025, vol. 111, p. 105527. ISSN 0997-7538. Available from DOI: https://doi.org/10.1016/j.euromechsol.2024.105527.

[38] GAO, H.; HUANG, Y.; NIX, W.D.; HUTCHINSON, J.W. Mechanism-based strain gradient plasticity—I. theory. *Journal of the Mechanics and Physics of Solids*. 1999, vol. 47, no. 6, pp. 1239–1263. ISSN 0022-5096. Available from DOI: https://doi.org/10.1016/S0022-5096(98)00103-3.

[39] PTÁČEK, L. *Nauka o materiálu I*. Brno: CERM, 2003. ISBN 80-7204-283-1.

[40] *Kovové materiály – Zkoušení tahem – Část 1: Zkušební metoda za pokojové teploty* [ČSN EN ISO 6892-1]. Praha: Česká agentura pro standardizaci, 2021.

[41] *Kovové materiály – Zkoušení tahem – Část 2: Zkušební metoda za zvýšené teploty* [ČSN EN ISO 6892-2 (420310)]. Praha: Česká agentura pro standardizaci, 2021.

[42] ASTM INTERNATIONAL. *Standard test Methods for Tension Testing of Metallic Materials* [ASTM International, West Conshohocken, PA]. 2024. Available also from: https://store.astm.org/e0008_e0008m-24.html. ASTM E8/E8M-24.

[43] ASTM INTERNATIONAL. *Standard Test Methods of Compression Testing of Metallic Materials at Room Temperature* [ASTM International, West Conshohocken, PA]. 2025. Available also from: https://store.astm.org/e0009-19r25e01.html. ASTM E9-19(2025)e1.

[44] ASTM INTERNATIONAL. *Standard Test Methods for Bend Testing of Material for Ductility* [ASTM International, West Conshohocken, PA]. 2022. Available also from: https://store.astm.org/e0290-22.html. ASTM E290-22.

[45] ASTM INTERNATIONAL. *Standard Test Method for Brinell Hardness of Metallic Materials* [ASTM International, West Conshohocken, PA]. 2023. Available also from: https://store.astm.org/e0010-23.html. ASTM E10-23.

[46] ASTM INTERNATIONAL. *Standard Test Methods for Rockwell Hardness of Metallic Materials* [ASTM International, West Conshohocken, PA]. 2024. Available also from: https://store.astm.org/e0018-24.html. ASTM E18-24.

[47] ASTM INTERNATIONAL. *Standard Test Method for Microindentation Hardness of Materials* [ASTM International, West Conshohocken, PA]. 2022. Available also from: https://store.astm.org/e0384-22.html. ASTM E384-22.

[48] ASTM INTERNATIONAL. *Standard Test Methods for Notched Bar Impact Testing of Metallic Materials* [ASTM International, West Conshohocken, PA]. 2025. Available also from: https://store.astm.org/e0023-25.html. ASTM E23-25.

[49] ASTM INTERNATIONAL. *Standard Practice for Conducting Force Controlled Constant Amplitude Axial Fatigue Tests of Metallic Materials* [ASTM International, West Conshohocken, PA]. 2021. Available also from: https://store.astm.org/e0466-21.html. ASTM E466-21.

[50] ASTM INTERNATIONAL. *Standard Test Methods for Conducting Creep, Creep-Rupture, and Stress-Rupture Tests of Metallic Materials* [ASTM International, West Conshohocken, PA]. 2024. Available also from: https://store.astm.org/e0139-24.html. ASTM E139-24.

[51] MOUSA, M. A.; YUSSOF, M. M.; HUSSEIN, T. S.; ASSI, L. N.; GHAHARI, S. A digital image correlation technique for laboratory structural tests and applications: A systematic literature review. *Sensors*. 2023, vol. 23, no. 23. ISSN 1424-8220. Available from DOI: 10.3390/s23239362.

[52] ZEISS INDUSTRIAL QUALITY SOLUTIONS. *Digital image correlation: Motion and deformation analysis* [https://www.zeiss.com/metrology/en/explore/topics/digital-image-correlation.html]. [N.d.]. Accessed: 2025-04-15.

[53] GÓRSZCZYK, J.; MALICKI, K.; ZYCH, T. Application of digital image correlation (DIC) method for road material testing. *Materials*. 2019, vol. 12, no. 15. ISSN 1996-1944. Available from DOI: 10.3390/ma12152349.

[54] ŠEBEK, F. *Photographs of the test apparatus, miniature specimens, etc.* [Archive of doc. Ing. František Šebek, Ph.D.]. 2025. Photograph.

[55] WANG, D.; TAN, D.; LIU, L. Particle swarm optimization algorithm: an overview. *Soft Computing*. 2018, vol. 22, pp. 387–408. Available from DOI: 10.1007/s00500-016-2474-6.

[56] KENNEDY, J.; EBERHART, R. Particle swarm optimization. In: *Proceedings of ICNN'95 - International conference on neural networks*. 1995, vol. 4, pp. 1942–1948. Available from DOI: 10.1109/ICNN.1995.488968.

[57] ZHANG, Y.; WANG, S.; JI, G. A comprehensive survey on particle swarm optimization algorithm and its applications. *Mathematical Problems in Engineering*. 2015, vol. 2015, pp. 1–38. Available from DOI: 10.1155/2015/931256. Article ID: 931256.

[58] CLERC, M. *SPSO descriptions* [Technical Report, Independent Researcher]. 2018. Available also from: https://hal.science/file/index/docid/764996/filename/SPSO_descriptions.pdf. HAL Id: hal-00764996.

[59] MATHWORKS, INC. *Particle swarm optimization algorithm* [https://www.mathworks.com/help/gads/particle-swarm-optimization-algorithm.html]. [N.d.]. Accessed: 2025-04-25.

[60] MATHWORKS, INC. *particleswarm* [https://www.mathworks.com/help/gads/particleswarm.html]. [N.d.]. Accessed: 2025-04-25.

[61] MATHWORKS, INC. *Particle Swarm Options* [https://www.mathworks.com/help/gads/particle-swarm-options.html]. [N.d.]. Accessed: 2025-04-25.

[62] VEJCHODA, O. *Application of DIC method for measurement of deformations on small specimens* [online]. Brno, 2020 [visited on 2025-05-20]. Available from: https://www.vut.cz/www_base/zav_prace_soubor_verejne.php?file_id=213530. Master's thesis. Brno University of Technology, Faculty of Mechanical Engineering. Supervisor: T. NÁVRAT.

[63] RASOCHA, D. *Control system design for small test machine* [online]. Brno, 2020 [visited on 2025-05-20]. Available from: https://www.vut.cz/www_base/zav_prace_soubor_verejne.php?file_id=211822. Master's thesis. Brno University of Technology, Faculty of Mechanical Engineering. Supervisor: S. VĚCHET.

[64] ŠEBEK, F.; SALVET, P.; BOHÁČ, P.; ADÁMEK, R.; VĚCHET, S.; NÁVRAT, T.; ZAPLETAL, J.; GANJIANI, M. Size effect on the ductile fracture of the aluminium alloy 2024-T351. *Experimental Mechanics*. 2024, vol. 64, no. 9, pp. 1483–1495. ISSN 1741-2765. Available from DOI: 10.1007/s11340-024-01108-3.

[65] AZURE PHOTONICS CO., LTD. *AZURE-6505THM*. 2025. Available also from: https://www.azurephotonics.com/productinfo/249491.html?templateId=1133605. Accessed: March 24, 2025.

[66] OPTO ENGINEERING. *TC3MHR016-C High-Resolution Telecentric Lens for 1.1" Sensors* [https://www.opto-e.com/en/products/tc3mhr-series/TC3MHR016-C]. [N.d.]. Accessed: 2025-03-03.

[67] PRUSA RESEARCH. *Prusa3D – Oficiální web Prusa Research*. 2024. Available also from: https://www.prusa3d.com/cs/. Accessed: 2025-03-03.

[68] GORJI, M. B.; FURMANSKI, J.; MOHR, D. From macro- to micro-experiments: Specimen-size independent identification of plasticity and fracture properties. *International Journal of Mechanical Sciences*. 2021, vol. 199, p. 106389. ISSN 0020-7403. Available from DOI: https://doi.org/10.1016/j.ijmecsci.2021.106389.

[69] KIM, J. S.; HUH, H. Evaluation of the material properties of an OFHC copper film at high strain rates using a micro-testing machine. *Experimental Mechanics*. 2011, vol. 51, no. 7, pp. 845–855. ISSN 0014-4851. Available from DOI: 10.1007/s11340-010-9395-6.

[70] SIT S.P.A. *Universal Joints*. 2025. Available also from: https://sitspa.com/wp-content/uploads/_documents/en/Universal-Joints.pdf. Accessed: 2025-03-03.

[71] ELEGOO. *Elegoo Saturn 3 Ultra Resin 3D Printer 12K*. Available also from: https://us.elegoo.com/products/elegoo-saturn-3-ultra-resin-3d-printer-12k?srsltid=AfmBOoqIpOqE3oj2d_HOTkhVM2LKnRkw2UGgVdnUrOlEMsJOxF1j0O-F. Accessed: 2025-02-25.

[72] THORLABS, INC. *PM100D Handheld Optical Power and Energy Meter Console*. 2025. Available also from: https://www.thorlabs.com/newgrouppage9.cfm?objectgroup_id=706. Accessed: March 24, 2025.

[73] BIOPDI. *Tensile testing – complete guide to testing metals, polymers and composite materials*. 2025. Available also from: https://biopdi.com/tensile-testing/. Accessed: 2025-01-20.

[74] HUANG, Y.; YOUNG, B. The art of coupon tests. *Journal of Constructional Steel Research*. 2014, vol. 96, pp. 159–175. ISSN 0143-974X. Available from DOI: https://doi.org/10.1016/j.jcsr.2014.01.010.

[75] ŠEBEK, F. *Zkouška tahem* [Semestrální práce]. Brno, 2012.

[76] KARPÍŠEK, Z. *Matematika IV. Statistika a pravděpodobnost*. Brno: CERM, 2013. ISBN 978-80-214-4858-2.

[77] EASILY, Statistics. *What is Johnson-Cook Model? Explained in detail*. 2025. Available also from: https://statisticseasily.com/glossario/what-is-johnson-cook-model-explained-in-detail/. Accessed: 2025-01-21.

[78] LIVERMORE SOFTWARE TECHNOLOGY. *LS-DYNA Keyword User's Manual. Volume I*. R13. Livermore, CA: Livermore Software Technology, 2021. Dostupné z: https://www.dynasupport.com/manuals/ls-dyna-manuals/ls-dyna_manual_volume_i_r13.pdf.

[79] MATWEB, LLC. *AISI 316Q Stainless Steel, Solution Annealed*. 2025. Available also from: https://asm.matweb.com/search/SpecificMaterial.asp?bassnum=mq316q. Accessed: 2025-02-02.

[80] MATWEB, LLC. *AISI Type 316 Stainless Steel, annealed, bar* [https://www.matweb.com/search/datasheet_print.aspx?matguid=1336be6d0c594b55afb5ca8bf1f3e042]. 2025. Accessed: 2025-05-04.

[81] MATWEB, LLC. *Special Metals INCONEL® Alloy 718*. 2025. Available also from: https://1url.cz/Z1bVu. Accessed: 2025-02-02.

[82] MATWEB, LLC. *ASM Material Data Sheet: Aluminum 2024-T4*. 2025. Available also from: https://asm.matweb.com/search/specificmaterial.asp?bassnum=ma2024t4. Accessed: 2025-02-02.

List of Figures

2.1 Comparison of quasi-static and dynamic stress–strain responses of Inconel 718 [7] . . . 17
2.2 Micro-flange upsetting [16] . . . 20
2.3 Inner and outer grains [16] . . . 21

3.1 Unique pattern used on miniature specimen compared to the original surface [54] . . . 30
3.2 Graphical representation of PSO algorithm [55] . . . 32

4.1 DIC camera lens TC3MHR016–C [66] . . . 34
4.2 Clamp of the camera lens . . . 35
4.3 Translational mechanism in x and y axes . . . 36
4.4 Translational mechanism in z axis . . . 37
4.5 Model of camera holder . . . 37
4.6 Camera holder and comparison with the old one [54] . . . 38
4.7 New specimens clamps . . . 39
4.8 Drawing of clamp 1 (dimensions in mm) . . . 40
4.9 Drawing of clamp 2 (dimensions in mm) . . . 40
4.10 Clamping representation . . . 41
4.11 Universal joint GU 01 E [70] . . . 42
4.12 Bolt to connect the joint and load cell (dimensions in mm) . . . 42
4.13 H coupler (dimensions in mm) . . . 43
4.14 Centering fixture . . . 44
4.15 Assembled joint . . . 45
4.16 Fixtures for clamping . . . 46
4.17 Fixtures with claps and specimen in a virtual cut . . . 46
4.18 Clamps housing (dimensions in mm) . . . 47
4.19 Design of a screw head (dimensions in mm) . . . 47
4.20 Testing apparatus [54] . . . 48
4.21 XYZ Translation Stage PT3/M [72] . . . 49

5.1 Types of used specimens [73] . . . 50
5.2 Standard specimen with 6 mm diameter . . . 51
5.3 Standard specimen with 8 mm diameter . . . 51
5.4 Representation of load stop . . . 54
5.5 Representation of the static curve calculation [74] . . . 54
5.6 Geometry of miniature specimens . . . 56

7.1 Engineering stress strain of quasi-static tests – AW 2024–T351 . . . 66

7.2 Mean value of engineering stress strain diagram – AW 2024–T351 67
7.3 Static curve – AW 2024–T351 68
7.4 Calibration for quasi-static test and extrapolation for numerical simulation 70

8.1 specimen geometry and boundary conditions 72
8.2 Finite element mesh 73
8.3 Results from simulation and its comparison with experiments – SS 316L . . 75
8.4 Results from simulation and its comparison with experiments – Inconel 718 76
8.5 Results from simulation and its comparison with experiments – AW 2024–T351 76

9.1 Flow curves for SS 316L 77
9.2 Johnson–Cook response surfaces for SS 316L 78
9.3 Flow curves for Inconel 718 79
9.4 Flow curves for AW 2024–T351 80
9.5 Johnson–Cook response surfaces for AW 2024–T351 81
9.6 Comparison size effect with quasi-static curve – AW 2024–T351 82

A1 Quasi-static tensile diagram – SS 316L 97
A2 Static tensile diagram – SS 316L 97
A3 Dynamic tensile diagram – SS 316L 98
A4 High-temperature tensile diagram – SS 316L 98
A5 Quasi-static tensile diagram – Inconel 718 99
A6 Static tensile diagram – Inconel 718 99
A7 Dynamic tensile diagram – Inconel 718 99
A8 Quasi-static tensile diagram – AW 2024–T351 100
A9 Static tensile diagram – AW 2024–T351 100
A10 Dynamic tensile diagram – AW 2024–T351 100
A11 High-temperature tensile diagram – AW 2024–T351 101
A12 Miniature specimen tensile diagram – AW 2024–T351 101

List of Tables

5.1 Parameters for quasi-static, dynamic and high-temperature tensile tests . . 51
5.2 Parameters for static tensile tests 53

6.1 All experiments performed 61

9.1 Parameters of Johnson–Cook material model and used properties for SS 316L 77
9.2 Parameters of Johnson–Cook material model and used properties for Inconel 718 79
9.3 Parameters of Johnson–Cook material model and used properties for AW 2024–T351 80
9.4 The effect of a change in cross section on the value of engineering strain . . 82

A Tensile diagrams

This appendix contains all engineering tensile diagrams obtained from the individual experiments and used to calibrate the Johnson–Cook material model. In cases where multiple tests were measured and an average (representative) curve was calculated, SEM are plotted at selected locations on the graph to show the variance of the measured values.

In the case of static tests, the measured engineering stress and strain curves are plotted from which the individual static curves were obtained. And their subsequent average to the reference value of the static curve.

Stainless steel 316L

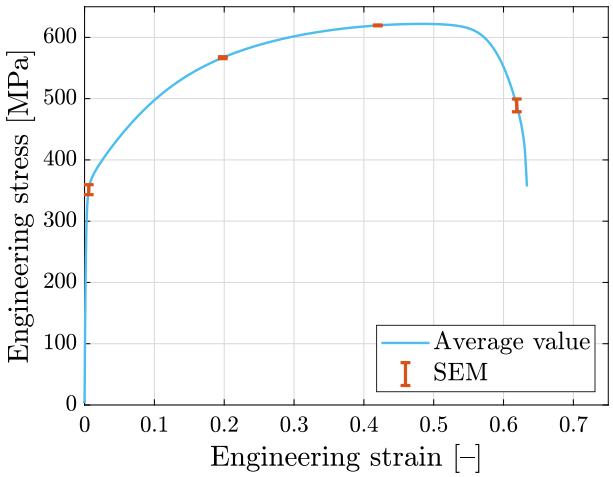

Figure A1: Quasi-static tensile diagram – SS 316L

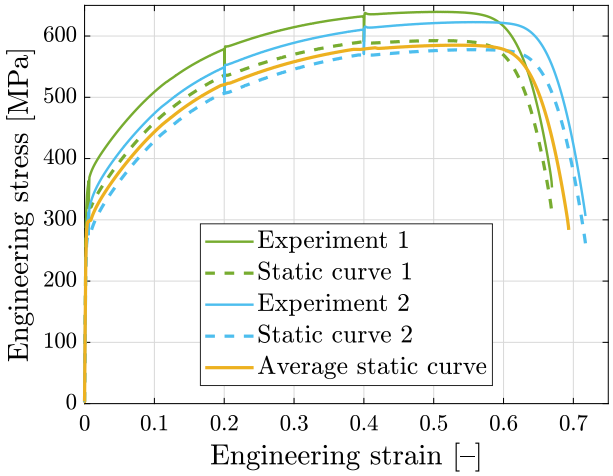

Figure A2: Static tensile diagram – SS 316L

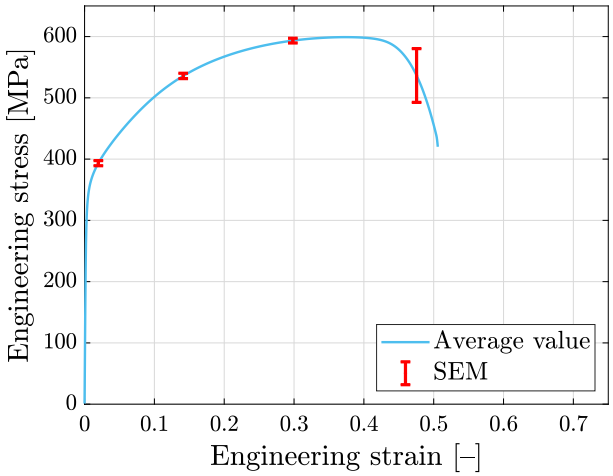

Figure A3: Dynamic tensile diagram – SS 316L

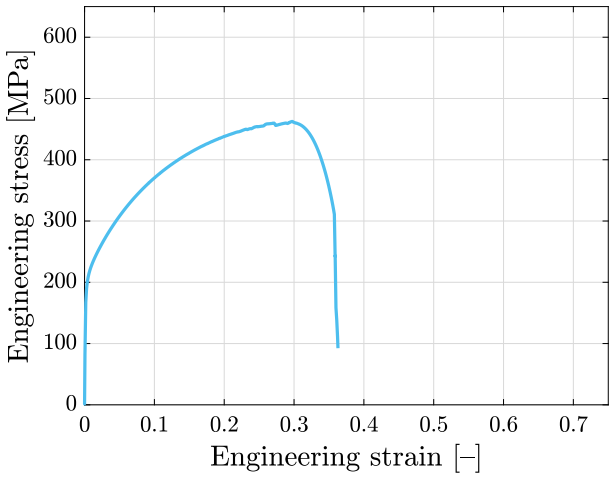

Figure A4: High-temperature tensile diagram – SS 316L

Incolen 718

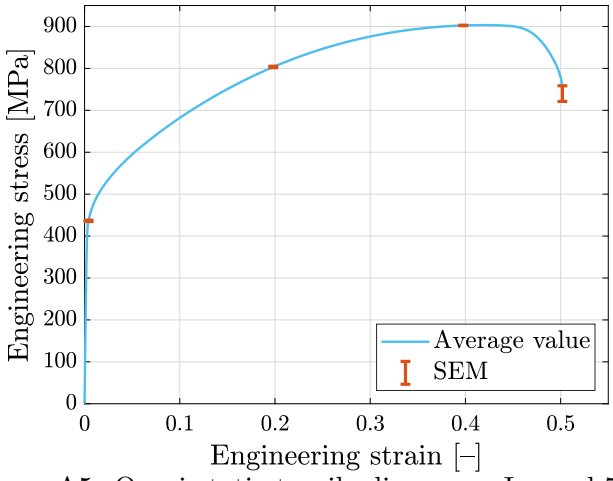

Figure A5: Quasi-static tensile diagram – Inconel 718

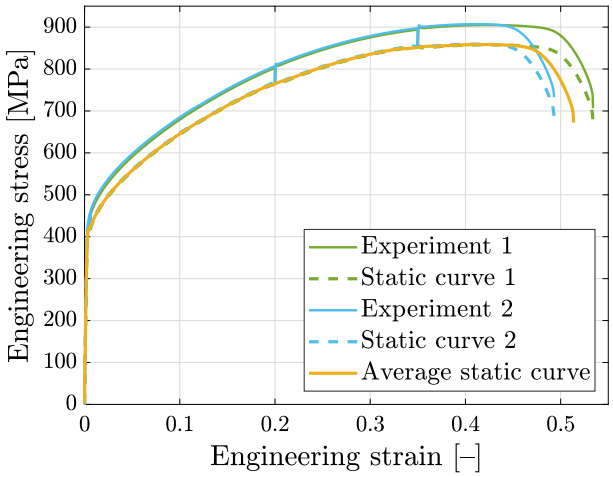

Figure A6: Static tensile diagram – Inconel 718

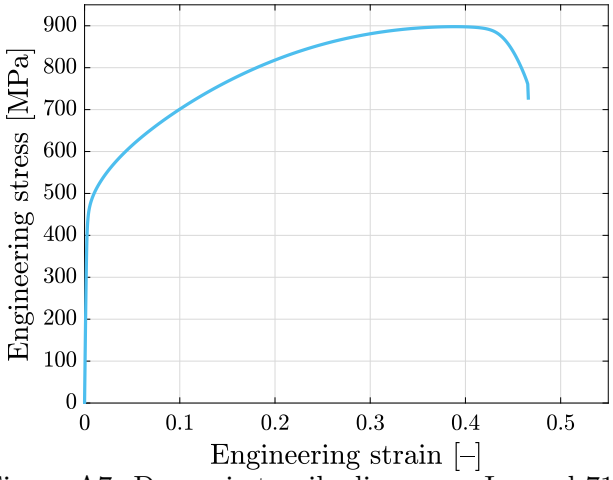

Figure A7: Dynamic tensile diagram – Inconel 718

AW 2024–T351

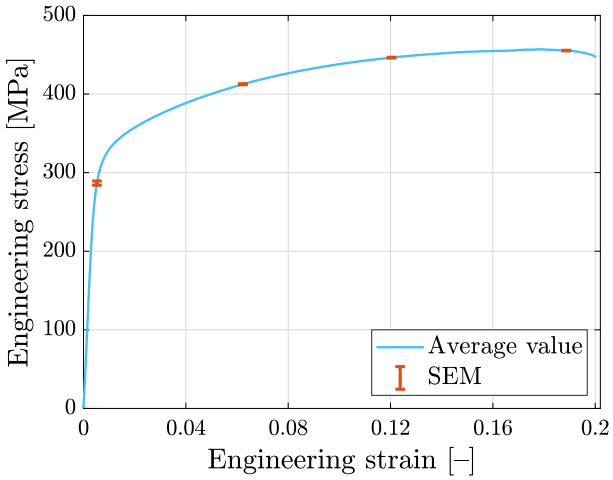

Figure A8: Quasi-static tensile diagram – AW 2024–T351

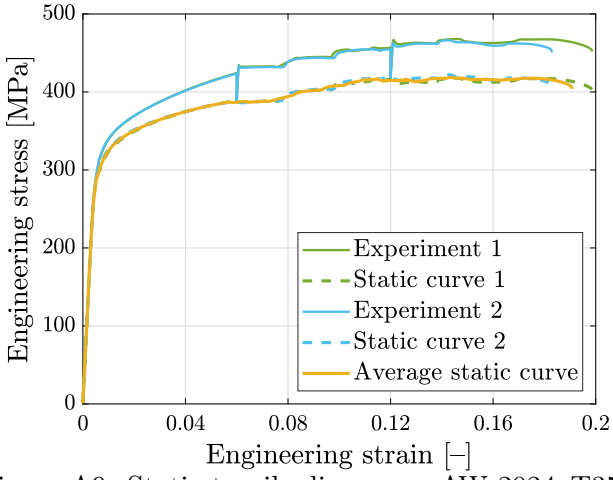

Figure A9: Static tensile diagram – AW 2024–T351

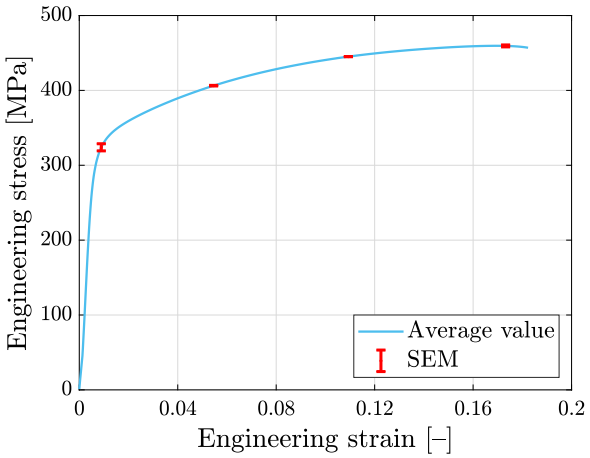

a) Dynamic 100 mm/min

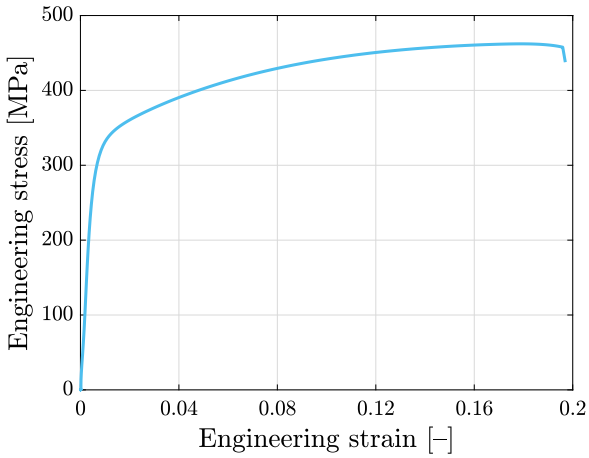

b) Dynamic 200 mm/min

Figure A10: Dynamic tensile diagram – AW 2024–T351

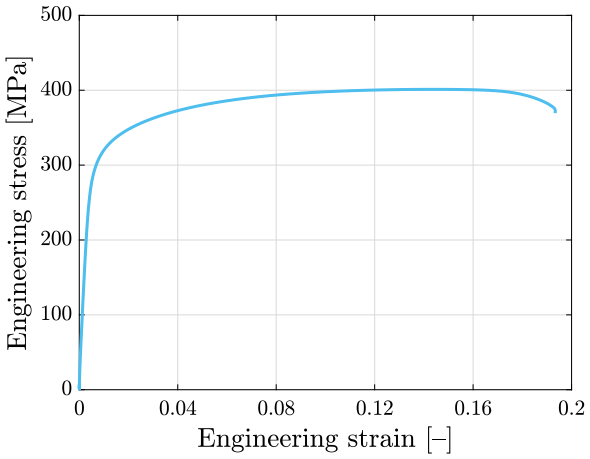

a) High-temperature + 150°C

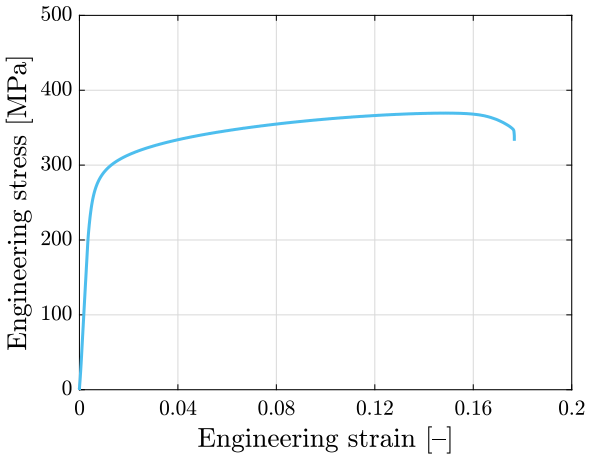

b) High-temperature + 200°C

Figure A11: High-temperature tensile diagram – AW 2024–T351

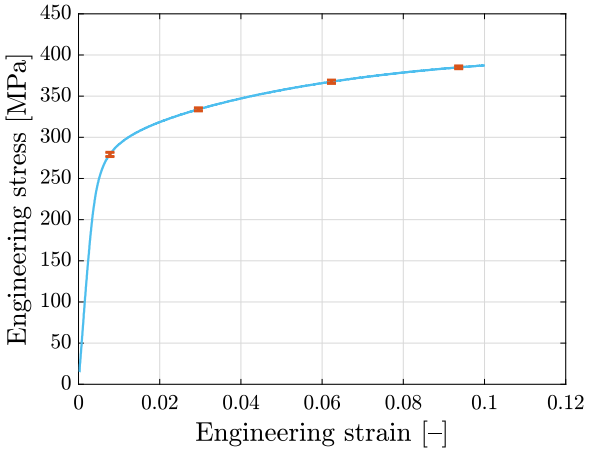

a) Mini tensile_16

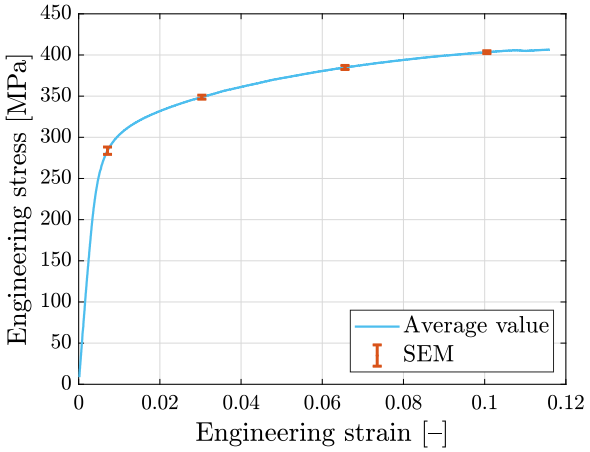

b) Mini tensile_20

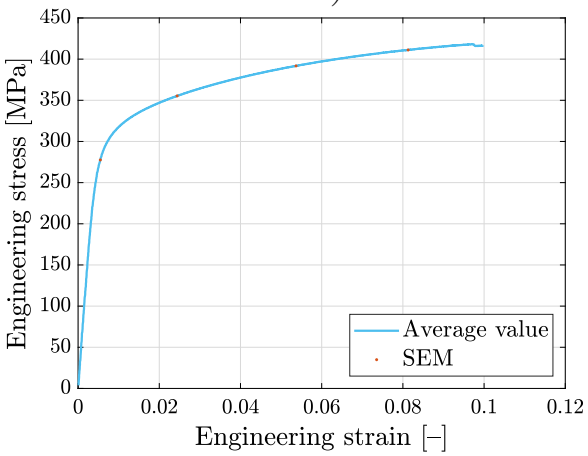

c) Mini tensile_32

Figure A12: Miniature specimen tensile diagram – AW 2024–T351

B *.k files

A folder named `Appendix_B` containing additional subfolders with names corresponding to the individual material containing the folders with the *.k files used for the calculation in LS-DYNA for the given test types.